1-1-1976

Observations of the near-infrared solar corona and a new interferometric telescope test.

Raymond Newton Smartt
University of Massachusetts Amherst

OBSERVATIONS OF THE NEAR-INFRARED SOLAR CORONA

AND

A NEW INTERFEROMETRIC TELESCOPE TEST

A Dissertation Presented

By

RAYMOND NEWTON SMARTT

Submitted to the Graduate School of the
University of Massachusetts in partial fulfillment
of the requirements for the degree of

DOCTOR OF PHILOSOPHY

February 1976

Physics and Astronomy

OBSERVATIONS OF THE NEAR-INFRARED SOLAR CORONA

AND

A NEW INTERFEROMETRIC TELESCOPE TEST

A Dissertation Presented

By

RAYMOND NEWTON SMARTT

Approved as to style and content by:

John D Strong

Dr. John D. Strong, Chairman of Committee

Edward R Harrison

Dr. Edward R. Harrison, Member

G. R. Huguenin

Dr. G. Richard Huguenin, Member

Phillips R Jones

Dr. Phillips R. Jones, Member

F.W. Byron

Dr. F.W. Byron, Jr., Head
Department of Physics and Astronomy

December 1975

ACKNOWLEDGMENTS

This work was carried out under the guidance of Professor John Strong, who initiated the coronal observation experiments here described. His support and encouragement are deeply appreciated.

Experimental programs such as these necessarily involve the direct participation of more than one person, and the assistance of many. In particular, Mr. William Dalton has taken much of the responsibility, both administratively and in the skilled design, construction, and testing of experimental systems. Mr. Ta-Chun Li has displayed meticulous care in the construction and testing of all electronic systems, while Mr. Lawrence Provo has been responsible for much of the machine shop work, as well as assisting in the experimental procedures.

The cooperation of the staff of the National Center for Atmospheric Research Balloon Launch Facility is greatly appreciated, as well as their technical competence. The NCAR field support group provided excellent logistics support for the African eclipse, and we acknowledge the helpful cooperation of government officials of the Republic of Kenya.

Portions of this research were supported by the National Aeronautics and Space Administration, Solar Physics Program, under Grant NGL 22-010-025, and by the National Science Foundation under Grant GP-36857.

ABSTRACT

Observations of the Near-Infrared Solar Corona
And
A New Interferometric Telescope Test

(December 1975)

Raymond N. Smartt, B.Sc., A.S.T.C., University of New South Wales; A.A.I.P., Australian Institute of Physics; M.S., University of Rochester

Directed by: Professor John Strong

Prior observations of the infrared outer solar corona have revealed enhancements, or peaks, in the elongation radiance function. These localized peaks, previously predicted, have been attributed to thermal emission by circumsolar particles undergoing vaporization at critical solar distances.

The first part of this work is concerned with further observations of the near-infrared solar corona. Three experiments have been carried out, two with a balloon-borne infrared scanning coronagraph during balloon flights of October 24, 1971, and October 29, 1973, and the other, ground-based at the June 30, 1973, total solar eclipse. The performance of the 6-detector coronagraph is evaluated, particularly with regard to its novel dual reflective optical systems. Both quantitative and qualitative scatter tests of the primary mirrors confirm that such a system is a viable alternative to a refractor coronagraph, even at visible wavelengths.

The coronagraph balloon flight radiance data, derived from coronal scans spanning elongations of approximately 3-13 $R_{\odot}$, and a wavelength

range of 2-4μ, is presented. The data is found to be uncontaminated by the presence of non-coronal radiation, except over the inner portion of the scan range, where the results are regarded as equivocal. No peaks are evident in the outer portion, as previously observed, indicating a temporal variation of this coronal component.

The eclipse data represents the coronal elongation radiance distribution parallel to the ecliptic, over a range of approximately 2-9 $R_{\odot}$, at a wavelength of 1μ. The distribution differs only slightly from the observed radiance of the white-light corona. The origin of this difference is attributed to the dust-free zone.

The second part of this work is a description of a new two-beam interferometer, and its application to the testing of telescopes. The interferometer is positioned at the image of a point source, and forms a spherical reference wavefront by diffraction of part of the incident light. Field tests using both star and laser sources have proved to be successful.

TABLE OF CONTENTS

Acknowledgments iv

List of Tables viii

List of Figures ix

Chapter I INFRARED CORONA: INTRODUCTION 1

Review 6

Recent Infrared Coronal Observations 11

Chapter II REFLECTOR CORONAGRAPH 14

Introduction 14

Coronagraph Systems 15

Reflector-Coronagraph Optical System 19

Primary-Mirror Tests 25

Chapter III BALLOON-BORNE EXPERIMENTS 36

Introduction 36

Calibrations 40

Results 44

Chapter IV ECLIPSE EXPERIMENT 50

Introduction 50

Instrumentation 50

Experimental Procedure 51

Radiance Calibrations 52

Results 59

Chapter V INTERFEROMETRIC TELESCOPE TEST 65

Introduction 65

Point-Diffraction Interferometer 71

Telescope Testing 77

Tables 83

Figures 92

References 123

LIST OF TABLES

Table 1. Detector Parameters. 83

Table 2. Primary Mirror Scattered Radiance Measurements 84

Table 3. Responsivity and D* Measurements 86

Table 4. Balloon-Flight Parameters. 87

Table 5. Number of Coronal Scans Obtained During Balloon Flights. . . 88

Table 6. Eclipse Data Ratios. 89

Table 7. Comparison of Observed and White-Light Coronal Radiances . . 90

Table 8. Ratios of Observed and White-Light Coronal Radiances 91

LIST OF FIGURES

Figure 1. Coronagraph Optical Configuration. 92

Figure 2. Mirror Scatter Test. 93

Figure 3. Mirror Scatter Test. 94

Figure 4. Scatter Measurements of Three Coronagraph Primary Mirrors. 95

Figure 5. Comparison of Primary Mirror Scatter Measurements Before and After a Balloon-Flight. 96

Figure 6. Dark-Ground Test 97

Figure 7. Dark-Ground Images of a Primary Mirror 98

Figure 8. Phase-Contrast Test. 99

Figure 9. Phase-Contrast Images of Primary Mirrors 100

Figure 10. Scatter Measurements of Mica Coated with Single Evaporated Layers. 101

Figure 11. Scatter Measurements of Mica Coated with Two Evaporated Layers. 102

Figure 12. Spectral Response of Coronagraph Detectors 103

Figure 13. Scatter-Plate Reflectance Measurement. 104

Figure 14. Coronal Radiance Measured During the 1971 Balloon-Flight; Detectors #1, #2, and #3 105

Figure 15. Coronal Radiance Measured During the 1971 Balloon-Flight; Detectors #4 and #6. 106

Figure 16. Coronal Radiance Measured During the 1973 Balloon-Flight; Detector #4. 107

Figure 17. Coronal Radiance Measured During the 1973 Balloon-Flight; Detector #6. 108

Figure 18. Eclipse Telescope Optical System 109

Figure 19. Detector System Spectral Response. 110

Figure 20. Detector System Spectral Response. 111

Figure 21. Telescope Scan Program 112

Figure 22. Relative Orientation of Eclipse Scans. 113

Figure 23. System to Measure Detector Responsivity. 114

Figure 24. Observed Coronal Radiance, $N_{c,e}$. 115

Figure 25. Observed Coronal Radiance, $N_{c,w}$. 116

Figure 26. Ratios of Observed and White-Light Coronal Radiances. 117

Figure 27. Principle of Operation of the Point-Diffraction Interferometer 118

Figure 28. PDI Interferograms of a 152-cm Cassegrain Telescope. . 119

Figure 29. Interferometer/Image-Intensifier System. 120

Figure 30. PDI Interferograms of a 61-cm Cassegrain Telescope . . 121

Figure 31. PDI Interferograms of a Schmidt-Cassegrain Telescope. 122

Figure 32. PDI Interferograms of a Maksutov-Cassegrain Telescope. 122

CHAPTER I

INFRARED CORONA: INTRODUCTION

This portion of the research has been concerned primarily with observations of the outer solar corona at near-infrared wavelengths--observations designed to amplify earlier measurements that revealed anomalous enhancement of the observed corona at several elongations. These localized "peaks" have been attributed to thermal emission by interplanetary particles at heliocentric distances where sublimation becomes significant, a postulate apparently consistent with reasonable theoretical models. The present observations were obtained with the Strong infrared reflecting coronagraph during stratospheric balloon flights on October 24, 1971, and October 29, 1973, and with an infrared telescope at the June 30, 1973, total solar eclipse.

Historical Perspective

Over a period of about 100 years the solar corona has been systematically observed during total solar eclipses by photometric, radiometric, and photographic methods. It is instructive to review briefly some of the early experiments and to trace the evolution of early concepts of the physical processes which give rise to the observed corona; the degree of insight is impressive since accurate experimental data at that time was meager.

In 1860 Lord Kelvin[1] wrote to the Royal Astronomical Society of London suggesting a solar eclipse experiment: the measurement

of thermal radiation of the corona during the period of totality. He stated, "The 'photosphere,' which I suppose is always seen around the Moon's disk during a total eclipse of the Sun, and which must be due to her light reflected from atmosphere or dust around the Sun itself, must radiate heat, and would probably show a sensible effect, as compared with radiation from an equal angular area of the Moon." The suggested method of observation was to use small thermometers, their blackened bulbs located at the coronal/lunar image formed by a reflecting telescope; one bulb within the lunar image and the others in the coronal image would provide a differential measurement. The letter further pointed out that, "a mirror would be better than a lens, because the *hot dust* around the Sun must produce radiant heat; and which, therefore, would be much absorbed by glass."

T. A. Edison[2] invented an instrument, called a "Tasimeter," "for measuring the heat of the stars and the Sun's corona." Designed for use at the focus of a telescope, the tasimeter consisted of a strip of vulcanized rubber, placed between a fixed point and a carbon button. Radiation caused the rubber strip to expand, decreasing the resistance of the carbon button, and destroying the balance of a Wheatstone bridge. The required correction provided a radiance measurement. Observations during the total solar eclipse of 1878 were unsuccessful, "since the galvanometer went off-scale and could not be balanced before the end of totality." Only one other attempt to measure coronal thermal radiation appears to have been made prior to this time: Magrini[3] used a "thermoscope" to measure thermal energy in the image of the corona formed by a reflecting telescope. His system responded during totality but the data is uncalibrated.

At visible wavelengths, most of the pioneering eclipse experiments attempted to measure the spatial extent, brightness and polarization state of the corona. It was customary to compare the brightness of the corona with that of the full Moon, using either a direct visual estimate, or at best a visual photometric method.

At the eclipse of 1860, J. M. Wilson[4] used a wedge of dark glass to estimate the brightness of the corona. He found the extreme inner part of the corona to be brighter than the new Moon. According to the 1878 eclipse measurements of J. W. Langley,[5] the corona at 1 arc min from the Moon's limb was 6x the brightness of the Moon, and at 3 arc min only 0.1x. He used a visual photometer, a large uncertainty arising from the candle reference source. Using these and other eclipse results, including photographic records, W. Harkness[6] deduced that the total light of the corona was about 7×10^{-6} that of the Sun, that the coronal light "varied inversely as the square of the distance from the Sun's limb," and that "the corona of 1870 seems to have been 7x brighter than that of the corona of 1878." For the eclipse of 1886, W. Abney and T. E. Thorpe[7] used a "grease-spot" photometer and a "standard lamp" reference source, while E. C. Pickering[8] made photographic photometric measurements. Such pioneering measurements using new techniques mostly gave inaccurate results; Pickering, for example, found that the coronal brightness varied even less than the low value deduced by Harkness.[6] At the same eclipse, H. H. Turner[9] used different observers to estimate the visible limit of the corona. One observer estimated a streamer out to 15 $R_\odot$, using a mask to obscure the corona out to 3 $R_\odot$, with precautions observed to ensure complete dark adaptation.

In a report of 1871, G. G. Stokes[10] enumerated "the chief points to which observers of polarization [of the solar corona] should direct their attention." In discussing the nature of the "outlying" corona, he suggested that it is due to, "a) circumsolar matter (though at a great distance from the Sun) reflecting light, b) circumsolar matter in the state of a self-luminous gas, c) circumsolar matter diffracting light, and d) lofty atmospheric haze or cloud, of excessive tenuity, diffracting light. The light ought to be, for a) strongly and radially polarized, b) unpolarized, c) and d) insensibly or all but insensibly polarized."

G. K. Winter[11] used a Savart polariscope at the eclipse of December, 1871. The corona close to the Moon's limb was found to be linearly polarized with the magnetic vector along a radial direction, the degree of polarization at 10 arc min being greater than closer to the limb. These results were apparently the first quantitative measurements of the ratio of polarized to unpolarized coronal light. Further polarimetric observations were made by A. W. Wright[12] at the eclipse of 1878. He confirmed the earlier results of Winter[11]--that the polarization is radial--but found a continuous decrease in percentage polarization out from the limb. To account for the decrease in percentage polarization beyond the region where "prominences occur," he suggested the possibility of an increased proportion of matter in solid form. The result would be the same, he postulated, "whether this has its origin in material thrown up by the tremendous eruptive actions in the regions of prominences, to such heights as to permit its condensation into solid particles which fall back to be again vaporized, or whether it consists of innumerable small meteoric bodies which are continually falling upon the Sun. The existence of such bodies is not doubted, and that they are more numerous about the equatorial regions of the Sun may be considered

to be indicated by the greater extension of the corona in this direction, and by the phenomenon of the zodiacal light, which is now generally regarded as depending upon the reflection of the light of the Sun from such small bodies, if indeed it may not be considered as actually in physical continuity with the outer extension of the corona."

A. Schuster[13] (1879) provided an initial theoretical basis for interpretation of polarimetric coronal measurements. He showed that such observations can give information about both the spatial distribution of scattering particles, and the angular dependence of different components in the observed corona.

In a review paper of 1885, W. Huggins[14] elaborated on the then current concepts of the physical origin of the solar corona, substantially supporting the views of Wright.[12] He pointed out that the spectrum of the corona is compound, consisting of: "a) a bright continuous spectrum, which informs us that it comes from incandescent solid or liquid matter; b) a solar spectrum, which shows that the incandescent solid or liquid matter of the corona reflects to us light from the photosphere; c) a spectrum of bright lines which is relatively faint and varies greatly at different eclipses . . . this spectrum tells us of gaseous matter which accompanies the solid or liquid matter." From the spectral information he inferred that "the corona is fed from the Sun itself," since, "the coronal gas is shown to consist of substances which exist also in the photosphere;" he also mentioned that since comet matter "is condensed into discrete particles which form the tail, we should also expect these particles to be again vaporized in their near approach to the Sun." On the question of spatial distribution, he states that "there is a great probability that the corona

has not an outer boundary, but that it is lost in an increasing faintness and diffusion. The absence of a limit is probably true only of the faint outer part of the corona. Within, and especially about the distance from the Sun's limb to which the so-called "inner-corona" usually extends, there is evidence of an apparent arrest of coronal matter, due in part probably to the effects of perspective, and within this distance are seen numerous rays which turn around and descend towards the Sun." The dominant contribution of the electron-scattered component to the observed inner continuum corona was not recognized until much later; but diffraction, reflection and thermal emission by interplanetary particles, and the link between the outer corona and the zodiacal light had all been at least suggested last century. Sixty years later, diffraction by interplanetary particles was proposed as the dominant mechanism responsible for the visible F-corona.

Review

The visible solar corona is thought to be composed principally of two scattered-light components,[15] denoted by K and F.* The K-component arises from Thompson scattering by an atmosphere of free electrons around the Sun. It is characterized by the absence of Fraunhofer lines, and a rapid decrease in brightness with distance from the limb (although coronal "streamers" have been observed to extend beyond 20 $R_{\odot}$); it is polarized and varies with solar activity. The F-component is attributed to

---

*This "classical" concept has recently been questioned.[16,17]

scattering by dust particles in interplanetary space,[18,19] such particles being identified with those responsible for the zodiacal light. This component shows Fraunhofer lines, and decreases more slowly with increasing elongation than the K-component, becoming dominant in the outer corona. As with the zodiacal light, it is asymmetric with a concentration in the vicinity of the ecliptic.[20]

The brightness, structure, and extent of the K-corona are broadly correlated with the phase of the solar cycle. Near solar maximum, the isophotes are almost circular; at solar minimum, equatorial streamers predominate, and polar features are greatly reduced. At this time the total coronal brightness is less than half that during solar maximum. Apart from such secular changes, coronameter patrol observations reveal day-to-day variations which occur in response to localized solar activity. Recent satellite data has shown that observable changes in coronal distribution can occur within a period of less than one hour.[21] Some apparent variations of the F-corona on a time scale of a few days, or longer, have been described,[22] but it is generally believed to remain substantially constant with time.

Emission lines observed in the inner solar corona can be considered as a third, or E-, component, and thermal emission by near-circumsolar interplanetary particles as a fourth, or T-, component. It has been suggested that such particles should make a significant contribution to radiation from the outer corona at near-infrared wavelengths.[23] As pointed out above, this idea is not new; towards the end of last century, attempts were made to explain the continuum spectrum of the corona in terms of high-temperature meteoric dust,[14] and infrared eclipse observations

were carried out to this end.[24,25] It is only in recent years, however, that infrared techniques have developed sufficiently to provide the requisite sensitivity necessary to give useful measurements.

The above ideas encompass the recognized mechanisms responsible for the optically-observed "quiescent" coronal radiation;* the presence of large-scale magnetic fields and high energy electrons (associated with flare events) allows the possibility that synchrotron radiation, detected at radio frequencies, can occur also at visible frequencies;[17] this, and the possible influence of the solar wind on the observed corona, together suggest that the above ideas are somewhat simplistic. Certainly, the K-corona has extremely complex dynamics, as revealed by recent satellite observations in the visible and ultraviolet. Massive eruptions in the outer corona have been observed, apparently resulting from the disintegration of extensive coronal streamers, each event associated with large coronal "clouds" moving out from the Sun at high velocity. Observations at radio frequencies have detected sources moving rapidly away from the Sun following flare events.[26] Parallel observations in the visible indicate that concurrent temporary depletion of part of the corona can occur, as evidenced by reduced radiance, with recovery within a period of several hours.[21]

The isolation of the K- and F-components has been a major concern in the analysis of coronal radiance measurements. In the infrared, the observed non-K-component (excluding the emission spectrum) is, itself, possibly a composite of three significant components: diffraction,

---

*The term "solar corona" is used simultaneously in the literature with, strictly, two different meanings; as well as that of the physical region itself, external to the chromosphere, it is also used in the sense of "observed radiance distribution."

reflection, and thermal emission by interplanetary particles.

It has been shown that small dust particles approaching the Sun will, within a finite radial distance, vaporize due to the intense insolation.[27] A particle in orbit about the Sun is under the influence of several significant forces; apart from gravity, radiation pressure, and the Poynting-Robertson drag, the solar wind and the interplanetary magnetic field give rise to a gas-kinetic drag and electromagnetic force drags.[28] The particle, therefore, spirals in towards the Sun, with a temperature increase and an abrupt mass loss due to vaporization at some critical distance. Studies of the dynamics of such particles indicate that the orbits tend to become increasingly eccentric as mass loss near perehelion occurs, and particles initially in the range of 1 μ to 10 μ eventually leave the system on hyperbolic orbits. Particles larger than 10 μ would totally evaporate. The physical characteristics of such particles determine the radius at which vaporization occurs, and within which such particles cannot exist. A circumsolar dust-free zone bounded by a narrow vaporization zone has therefore been postulated.[29]

This vaporization zone was recognized in early treatments of the F-corona. Van de Hulst[19] assumed, for purposes of discussion, a radius of 0.1 A.U. (21.4 $R_\odot$), while Allen[18] assumed an arbitrary value of 4 $R_\odot$. Coincidentally, Over[30] found that sublimation of SiO_2, using an idealized absorption curve, would occur at 4 $R_\odot$ at a transition temperature of 870 K; but this value critically depends on the properties of the dust particles. If they were black bodies, the equivalent distance would be 21 $R_\odot$.

A model for thermal emission by interplanetary dust has been derived by Peterson.[23] It predicts the radiance distribution at different i.r. wavelengths, for zones at 3.5 $R_\odot$, 6 $R_\odot$, 12 $R_\odot$, and 18 $R_\odot$. In a later analysis, Kaiser[31] constructed a model that employs optical cross-sections for emission and absorption; these depend on both wavelength and particle radius, resulting in a particle temperature dependence on radius. The heliocentric distance at which sublimation occurs is then particle-radius dependent.

Lamy[32] has also investigated the dynamical characteristics of the dust, following an approach similar to that of Kaiser, but using Mie-scattering theory: the essential results are, however, similar. The dynamics are found to depend crucially and sensitively on the optical characteristics of the dust. It was found that particles of 1 μ radius, after spiraling in towards the Sun, can remain in a well-defined "equilibrium zone," rather than escaping on a hyperbolic orbit. Sputtering by solar wind ions was found to be less destructive than sublimation. The derived thermal emission spectra of two natural silicates, obsidian and andesite, reveal the pronounced features of the reststrahlen band structure and emphasize the possibility of allowing unambiguous identification of the circumsolar dust particles from simultaneous multiwavelength observations.

Infrared coronal observations should thus lead to a further understanding of the physical processes associated with the observed corona, and, on the basis of the above models, provide further information about the physical nature, temperature, and distribution of interplanetary particles. In general such observations have given conflicting results.

Recent Infrared Coronal Observations

Low-temperature photoconductive detectors have been used in an attempt to detect thermal emission of circumsolar dust under non-eclipse conditions.[33] Scans of the i.r. aureole in the bands 1.8-3.0 μ and 3.5-5.2 μ revealed a higher radiance in the plane of the ecliptic than perpendicular to it, the difference attributed to a circumsolar component. This result was later challenged[34] when similar, but more sensitive observations at 2.2 μ failed to reveal such a difference. The conclusion was that sky radiance precludes such a measurement and that, instead, eclipse and balloon observations should be attempted. However, later coronal observations,[35] under non-eclipse but exceptionally clear conditions, showed a small peak at 4 $R_{\odot}$, attributed to thermal emission in the vicinity of the vaporization zone.

During the 1966 total solar eclipse, separate observers recorded features in the scanned outer corona. In one set of observations at 2.2 μ,[36] scanning approximately along the ecliptic, a prominent peak in the elongation distribution was found at 3.9 $R_{\odot}$, and a smaller peak at 3.3 $R_{\odot}$, both east and west of the Sun. Similar peaks were also observed immediately after totality, at a wavelength of 3.5 μ. With such scant spectral information, estimates of the dust vaporization temperature were found to vary from 870 K to 2000 K, depending on the model used. The 2.2-μ coronal radiance, compared with the visible, indicated a large infrared excess with a maximum reddening coefficient[37] (after allowance for reddening attributed to thermal emission) of 1.8 at 3 $R_{\odot}$. This value is consistent with some other measurements of the outer corona that have indicated an excess of radiation at red wavelengths, and a large excess

in the infrared.[37] However, for the observations at 2.2 μ,[36] diffraction reddening, according to existing models, was found inadequate to account entirely for the large reddening coefficient obtained.

A second eclipse observation,[38] also at 2.2 μ with scans parallel to the ecliptic, recorded similar peaks at 3.4 $R_\odot$ and 3.9 $R_\odot$, but the agreement in radiance is poor; the derived absolute radiance of the 3.9 $R_\odot$ peak differs between the two observations by a factor of two, and the radiance of the "continuum" corona by a factor of almost ten.

Further observational results were obtained from a stratospheric balloon-flight of an infrared coronagraph operating at 2.2 μ.[38] The data revealed a pronounced peak at 4.1 $R_\odot$, and evidence of peaks at 8.7 $R_\odot$ and 9.2 $R_\odot$. The minimum elongation recorded was equivalent to 3.6 $R_\odot$. Kaiser[31] provided an interpretation of the eclipse and balloon observations which together indicated peaks at approximately 3.4, 4.0, 8.7, and 9.2 $R_\odot$. He showed that a "stony" dust material could produce two emission peaks, one due to small, and the other to large particles (intermediate particles provide a background between the two peaks). Using synthetic optical constants, he attributed the peaks at 3.4 and 8.7 $R_\odot$ to one type of silicate-like material, and the other pair to a similar material of different mean opacity.

At the total solar eclipse of 1970, the i.r. outer solar corona was again observed, this time over a more extensive wavelength range. Simultaneous observations at 0.84 μ, 1.57 μ, and 2.23 μ revealed enhanced radiance, as before, near 4 $R_\odot$.[39] On the basis that such peaks represent the detection of thermal emission by dust particles, the equivalent particle equilibrium temperature was determined to be 2160 $\pm$ 200 K, a value

considerably higher than expected. It was therefore postulated that the particles were composed of graphite or some other highly refractory material. Another observation[40] at 10 μ failed to reveal any peaks. However, the scans were found to agree closely with the continuum radiance distribution predicted by Kaiser's[31] model.

The interpretation of the observed peaks as being due to thermal emission has been questioned;[41] it is claimed that the magnitude of the F-component of the corona is much smaller than previously thought, and that the minimum approach of particles to the Sun is probably about 10 $R_{\odot}$. But this work has in turn been criticized, and the earlier "classical" model of the F-corona defended.[20]

The above summary indicates the need for precise observations of the infrared corona, to try to resolve apparently conflicting evidence represented in both experimental and theoretical studies in this field. For this, we seek not only additional data concerning the previously observed peaks, but accurate knowledge of the elongation spectral-radiance function of the continuum corona at infrared wavelengths. Such results can lead to further information about the physical and chemical properties of the interplanetary dust and its density distribution, as well as general characteristics of both the F- and K- coronas. The infrared coronal observations reported here have produced a large quantity of relatively low-noise spectral-radiance data derived from radial scans of the outer corona. These results are analyzed in Chapters III and IV.

CHAPTER II

REFLECTOR-CORONAGRAPH

Introduction

During the 1880's, considerable interest developed in the possibility of observing the solar corona "outside of eclipse." G. E. Hale[42] used a spectroheliograph set on the K absorption line in an attempt to photograph the corona from a high-altitude site. The unsuccessful result led him to advocate a "differential bolometric technique."[43] He showed that meteoric particles near the Sun, treated as black or gray bodies, would reach temperatures considerably above that required for incandescence, and concluded that coronal "heat radiation" should therefore be easily measurable; but all attempts to detect the corona "in full sunlight" by Hale's method were unsuccessful. This led to further eclipse infrared measurements; the results were uncertain, limited by the relatively insensitive detection devices then available. H. Deslandres[44] recorded observations over the spectral region around 1.3 μ, and determined that the "heat" of the corona was about half that observed from the circumsolar sky without an eclipse, under exceptionally clear conditions; however, such a relationship could apply, at best, only within a few arc minutes of the solar limb. Subsequently, Deslandres claimed to have detected the corona under non-eclipse conditions.

Coronagraph Systems

Ground observation of the visible solar corona outside of eclipse is an exceedingly difficult task. Scattering, absorption and degraded seeing imposed by the atmosphere, as well as instrumental scattering, mean that only at high-altitude sites, under exceptionally clear conditions and using specially-designed telescopes, can the corona be detected. The radiance of the outer corona is far too small to allow any hope of its discrimination against the overwhelming sky background except by using sophisticated techniques. While the radiance of the inner corona is much greater, telluric-scattered radiation is also greater; and since this region is within a few arc minutes of the solar disk where the photospheric radiance exceeds the coronal radiance by a factor of $\sim 10^6$, instrumentally-scattered radiation can form a major component of the total extraneous radiation, unless special precautions are taken. B. Lyot[45-47] proposed the first successful coronagraph system, which substantially eliminated the primary causes of instrumental scattering. He used a singlet objective lens constructed from highest-purity optical glass, the surfaces polished to be as free from micro-ripples as possible, and scrupulously cleaned. The primary solar image was blocked by an occulting disk. Beyond, a field lens formed an image of the objective on a diaphragm which eliminated most of the diffracted light arising from the objective aperture. A small stop was also used to block axial light, attributed to multiple reflections, from reaching the camera lens and final image plane. While the coronal irradiance at this image plane is typically only a small fraction of that due to the sky and residual scattering, it can be discriminated polarimetrically since it is strongly polarized

with the magnetic vector radial to the solar disk. A major problem with the use of such an instrument--a K-coronameter--is the need to differentiate between the polarized component of the corona and that of the sky, which varies with zenith angle and dust content. Ground-based scanning K-coronagraphs, employing advanced electronic techniques, can record the K-corona out to about 2.0 $R_\odot$ from the limb.[48] Detection of the E-component is possible using birefringent or thin-film narrow-band filters tuned to one of the coronal emission lines; this permits efficient rejection of light from all sources at other wavelengths. More commonly, spectrographic isolation of emission lines is used. The radiance of the K-corona is proportional to the electron density, N_e, while the E-component is proportional to N_e^2. The E-component then has the larger gradient, and is not normally observed much beyond 0.3 $R_\odot$ from the limb.[49]

At visible wavelengths, the lower limit of the extraneous radiance of the Lyot coronagraph has been determined to be approximately 10^{-6} $N_\odot$, where $N_\odot$ is the mean solar radiance in the visible.[50] This value is almost entirely due to scattering within the objective lens. For the best observational sites, on the best days, telluric-scattered radiance is approximately 10^{-5} $N_\odot$ in the visible. This falls to approximately 10^{-8} $N_\odot$ at an altitude of 25 km,[51,52] roughly proportional to the exponential decrease in pressure. Therefore, in order for balloon-borne,[52,53] rocket-borne,[54] or satellite-mounted coronagraphs[21] to be able to take full advantage of the low background, the instrumental radiance should be reduced by a factor of at least 10^3 over that possible with the Lyot coronagraph. This can be achieved using external occultation. J. W. Evans[55] suggested using an occulting disk to prevent direct solar radiation from

reaching the objective. An improvement results from apodization. For example, if the disk boundary is serrated, the diffracted light within the geometrical shadow is diminished.[56] Alternatively, multiple disks can be used in series; for three disks, the spacing is such that the diffracted radiation directed toward the axis from the foremost disk is prevented from entering the objective aperture by the following disk; radiation diffracted by this disk is similarly blocked by a third disk. The geometry is also such that the second disk is shadowed by the first, and the third disk by the second. Therefore, if the angular diameter of the third disk, as seen from the objective, is greater than the angular diameters of the other two disks, the only direct photospheric radiation that can ultimately reach the objective, apart from scattering, is that which is triply diffracted. Note that the diffraction field from the anterior, or first disk, is a broadened function, due to a disk source, of that from following disks which have line sources. The efficiency of an occulting system depends on the geometry of the disk assembly and the optical system parameters. A satellite-borne, externally-occulted white-light coronagraph[21] that recorded to a minimum elongation of 1.5 $R_\odot$, was estimated to have an instrumental stray radiance of ~ 10^{-10} $N_\odot$. An additional advantage of external occultation is its vignetting characteristic; the dynamic range of the total coronal field sampled can be reduced if the design is such that the effective entrance aperture, over at least part of the field, decreases with decreasing elongation. A disadvantage is that the effective angular resolution simultaneously decreases, and the minimum elongation attainable in most instruments is much greater than with a pure Lyot system. Where only a

radial strip of the corona is viewed, a series of knife-edges in tandem (first suggested by J. Strong) can be used instead of disks. For three knife-edges, this can result in a reduction of diffracted radiation at the objective of the order of 10^{-2} that of the equivalent disk configuration.[53] Knife-edges were also used in the Strong infrared reflector coronagraph, the instrument used for the research here described.

In an n-stage occulting system, only radiation which has been successively diffracted n-times can reach the objective aperture. But the gain in efficiency as n increases is at the expense of a reduced tolerance in the edge settings--for knife-edges this includes parallelism as well as distance from the axis; if a knife-edge, or disk, is set too far from the axis, it can annul the shielding effect of edges both anterior and posterior to it; if too close its own effect is annulled. MacQueen[53] used three equally-spaced knife-edges set in arithmetic progression. Such a specification assumes precise settings. The effectiveness of the center knife-edge rapidly approaches zero for a small displacement towards the axis; for the 30-cm knife-edge separation used by MacQueen, this corresponds to an error of 0.3 mm, while the optimum condition is halved for an error of approximately 0.1 mm. If the second knife-edge is set further from the axis than the mean position, it intercepts more radiation from the first knife-edge and hence constitutes a higher radiance source. This increase is partly offset by the circumstance that the third knife-edge is then deeper within the shadow of the second knife-edge. For such a three knife-edge system it is therefore prudent to "overset" the second knife-edge so that it lies just outside the limit of possible measurement error. From diffraction theory, the second knife-edge

reduces the irradiance at the third knife-edge by a factor of approximately 4, compared with the case where the second knife-edge is inoperative. In practice, the reduction is likely to be less due to dust particles on the knife-edges and imperfect knife-edge alignment.

Reflector-Coronagraph Optical System

In 1963, Newkirk and Bohlin[50] pointed out that a coronagraph which employed a primary mirror objective would avoid the chromatic aberration of the singlet Lyot objective lens,* and the problem of scattering would then be one of surface scattering only. Laboratory tests indicated the feasibility of a reflection system.[58,59] A u.v. rocket-borne coronagraph has been reported which employs an aluminized objective mirror.[60] The performance of the Strong reflector-coronagraph confirms the practicality of such a system at near-infrared wavelengths. The optical system, represented in Fig. 1, is now described.

The coronagraph has twin optical systems which view the corona on opposite sides of the solar disk. In each system, a primary-mirror objective, operating off-axis, reflects the coronal field through the aperture stop to the enclosed detection system--a mirror train, chopper, lens and a set of three filtered detectors, six in all. All mirrors are coated with gold, which has a reflectance of ~ 0.98 over the operating spectral range of 2 μ to 4 μ. Dimensions of the entire system are set out in Fig. 1.

---

*An alternative approach is to use a Mangin mirror within the optical system to achromatize both the objective and the relay lens.[57]

The primary focal-plane field stop limits the angular field to 0.8 $R_\odot$ horizontally and 1.0 $R_\odot$ vertically. Beyond the primary image plane, two off-axis ellipsoidal mirrors in turn fold the axis and direct the beam to a cluster of small plane mirrors. A 400-Hz Bulova chopper operates at the focus formed by the first of the two ellipsoids. The plane mirrors are close to the relayed field-stop image and function as a three-part field divider. The rays that comprise the central third of the image patch pass between two of the mirrors (mutually inclined at ~ 90°), and are focused by an aspheric, anti-reflection coated, silicon lens to the central detector. The outer thirds are further reflected to give laterally-displaced images that are focused by the lens at the two adjacent detectors. The instantaneous fields of view of the three detectors therefore have slight relative angular displacements. A plane-parallel LiF window between the lens and detectors isolates the vacuum environment of the liquid-nitrogen-cooled detectors, each covered by a different band-pass filter. The original design of the coronagraph used six PbS detectors; these have a sensitive area of 0.1 mm horizontally and 1.0 mm vertically. Detector #2 failed prior to the flight of October 24, 1971, and was replaced by an InAs detector, 1 mm diameter.

The coronagraph has an auxiliary entrance aperture and optical system--a plane mirror and an MgO lens--by which radiation from a small region of the stratospheric sky, centered at the co-altitude of the Sun, is admitted to the internal optical train independent of the primary mirrors. The rear surfaces of the chopper vanes are gold-coated; when closed the vanes function as a reflector for the imaged sky radiation. The chopper is inclined so that the reflected beam follows the same path to the detectors as the coronal beam when the vanes are open. By this

method a component of the sky radiance included in the coronal detection can be removed.

The primary mirrors are mounted symmetrically on a metal plate that is pivoted about a central axis normal to the plane of the optical system. In operation, the plate oscillates linearly, via a cam-driven arm, with an 8-minute period. When the coronagraph mechanical axis is sun-centered, the two independent systems have coronal views on opposite sides of the solar disk. The corona is scanned in a direction normal to a vertical circle, at a rate of 0.04 $R_\odot$/s, and the detectors sample radial coronal strips covering a range of approximately 3 $R_\odot$ to 13 $R_\odot$. Since the rotation axis is remote from the primary mirrors, each primary focal plane has an oscillatory shift; but this amounts to only about 0.2% of the 63.5-cm focal length, and its effect is not significant. The detector spectral and scan ranges are set out in Table 1.

The external occulting assembly consists of two square baffles mounted in tandem, 46 cm apart, at the end of a conical boom. Knife-edges in the form of ground-steel strip, 0.013 cm thick and 1.3 cm wide, are attached to the vertical edges of the baffles. The anterior pair of knife-edges are each 24.88 cm from the center-line axis; the posterior pair are 24.31 cm from the axis, and 5.41 m from the plane of the primary mirrors. This geometry results in a convenient vignetting of the incident coronal radiation over the inner part of the scan.

For the initial balloon flight of the coronagraph, three occulting baffles were used, their knife-edges set sufficiently close to the axis such that no vignetting occurred over the scan range. The efficiency of this original geometry was more sensitive to static and dynamic tracking

errors than that of the wider baffles employed in the subsequent two flights. From the point of view of the tracking precision (~ ± 6 arc sec) achieved[61] in these two flights, the modified geometry was unnecessary--it allowed a tracking offset of 27 arc min before the posterior knife-edge would be exposed to direct sunlight. However, the associated properties of vignetting and reduced diffracted radiation at the primary mirrors were recognized as significant advantages, despite the concomitant imprecision in the reconstructed data, inherent in the vignetting-function correction. A further modification was the use of only two baffles. This allowed a reduction in the system moment of inertia by reducing the mass at the end of the 4-m boom. Further, the required alignment precision of the knife-edges could be relaxed. The overall efficiency of the occulting system was still superior to the original three-baffle system in which the knife-edges were set much closer to the axis.

An internal knife-edge baffle, or stop, indicated in Fig. 1, is located in the plane of the image of the external posterior baffle. For the October, 1971, balloon flight, this internal baffle was fixed. Under this circumstance, as the coronal field is scanned, the image of the external baffle is simultaneously scanned and enters the field of view of the detectors at elongations less than approximately 5.4 $R_{\odot}$. Thus the coronal field is gradually replaced by the posterior-baffle field, so that the external baffle becomes a potential source of extraneous radiation--emission and scattering--allowing the possibility of simultaneous detection with the vignetted coronal field. This can lead to ambiguities in the recorded signal. The advantage of a reduced signal dynamic range is

therefore offset by uncertainties in the data at small elongations. This problem was avoided in the October, 1973, flight. The pair of internal baffles were synchronously scanned with the image such that the internal knife-edges slightly preceded the image of the external knife-edge baffle. Direct radiation from the external posterior baffle was thus occulted and residual radiation from the internal baffle substituted. Only by indirect paths, scattering or diffraction, could radiation from the external baffles then reach the detectors. To minimize the effect of this possibility, the black-painted external posterior baffles were changed to gold-coated plexiglas reflectors; these were inclined to the boom axis so that only far-field sky radiation would be reflected to the primary mirrors.

A major problem in the design of a reflection coronagraph is to protect the primary mirrors from locally-scattered radiation without introducing secondary sources close to the direction of the field of view. This is important since, as indicated below, the scattering properties of the primary mirrors are strongly biased towards the specular direction. The wide external baffles used in the last two balloon flights of the coronagraph allowed more extensive shielding of the primary mirrors than was possible using narrow baffles. Interior surfaces of this shielding were covered with blackened aluminum-honeycomb panels. Reflection at a high angle of incidence, in the direction of the primary mirrors, could then occur only at the fine edges of the honeycomb sheet. Also, the boom surface, the optical-assembly outer cover, and other structural surfaces, all lying close to the direction of observation, were more extensively shielded from direct sunlight than was the case previously. The horizontal surface of the electronic housing, below the

optical system, is in direct sunlight under flight conditions, and constitutes a potentially harmful source of emitted and reflected radiation. For the 1973 flight, this surface was covered by a series of aluminized plexiglas vanes, each attached at such an inclination as to direct the reflected radiation away from the instrument.

A measurable cross-coupling between the two sets of detector outputs, on opposite sides, appeared in the results of the October, 1971, flight. Subsequent tests revealed the cross-coupling to be at least partly optical in origin. Additional internal baffling was incorporated to improve this system characteristic. For the 1973 flight, however, the maximum detector outputs were approximately two orders of magnitude less than those obtained in the October, 1971, flight, and any residual cross-coupling was negligible.

The assembled coronagraph was tested for its susceptibility to off-axis, external sources of radiation with a "sun-gun" probe. This confirmed the effectiveness of the optical-system shielding--the source could be brought to within 5° of the system field of view before the detector outputs increased. A further test was carried out with the coronagraph tracking the Sun, using a black-cavity target. The cavity consisted of two black-glass plates mutually inclined at an included angle of 10° to form a hollow vee, mounted in an open-ended wooden box. The glass surfaces had a high-quality polish and were maintained free from dust, so that incident radiation was strongly absorbed. The emergent radiation was then mainly thermal, appropriate to the temperature of the glass. The box was attached to the side of the coronagraph boom so that during the inner part of the primary mirror scan, the field of view of the corresponding detectors fell entirely within its aperture. The six detector outputs

were measured under these conditions. The worst case, detector #1, yielded an output of 2.5 μV. The corresponding output with the entrance aperture blocked was -1.5 μV. This performance was considered satisfactory, particularly since these results were not obtained with the best coronagraph primary mirrors, which were reserved for use on the flight, and since the ambient light was much greater than that in flight. A flight output of 2.5 μV for detector #1 corresponds to its response near maximum elongation.

Primary-Mirror Tests

The primary coronagraph mirrors, constructed from optical glass, have dimensions of 12.7 cm x 6.4 cm, and a radius of curvature of 127 cm. The effective aperture is 58 cm^2. Six mirror substrates were prepared by the manufacturer to have a "high quality" polish, and two others with a normal polish. After some preliminary tests, a single evaporated layer of gold was chosen for the reflecting film. The substrates were prepared by the usual cleaning procedures; ultrasonic cleaning methods were not available. The gold was evaporated in a few seconds, after discharge cleaning of the substrate, at a pressure of less than 10^{-5} torr. The film thickness was not instrumentally monitored; it was maintained approximately constant from run to run by the criterion that the evaporation filament could barely be seen in transmission just prior to terminating evaporation. Advantages of gold are its high reflectance in the near infrared, chemical inertness and ease of evaporation. Also, a gold film should remain substantially unchanged in its properties with time if protected from prolonged exposure to air-borne contaminants. Dust can

be removed by gently blowing with an air jet; (for the coronagraph flight, the mirrors were sealed by dust covers which opened only at float altitude). But a single gold film is relatively delicate. Film substrate adhesion can be improved by an intermediate layer of aluminum or chromium deposited beneath the gold film. However, for this type of application, the *softness* of the evaporated film is not a significant disadvantage, since there is normally no need to touch the surface directly, once prepared, and for *any* film such a procedure is likely to result in an impaired performance. Moreover, for recoating, a single gold film can usually be removed using adhesive tape, thus avoiding the microscopic damage to the polished glass substrate that can occur when the usual techniques for chemically removing films are used; as demonstrated below, it is crucially important to avoid such damage. Further, it has been found that scattering is greater for compound films.

Each of the primary mirrors was coated at least once prior to each of the coronagraph balloon flights of February and October, 1971, and October, 1973. The angular scattering properties of the mirrors were measured after each coating. A variety of qualitative tests were also applied and the investigation extended to other metallic-coated reflectors. A description of this work follows.

Scattering measurements. The angular dependence of scattered radiance, N, of the coronagraph mirrors was measured by the method indicated in Fig. 2. Apertures 1 and 2 limit the region of illumination at the mirror surface to a central patch approximately 3 cm diameter. Aperture 3 subtends a solid angle of 1.8×10^{-5} sr at the primary mirror surface. For convenience, the source was an unfiltered tungsten-filament

lamp. Since for this scattering regime the wavelength dependence of diffusely scattered radiation is approximately proportional to λ^{-2}, measurements in the visible region provide a safe margin when applied to the infrared. The photomultiplier output was detected by the usual synchronization-rectification technique. For each test, the mirror was initially adjusted so that specularly-reflected light was directed to the photomultiplier; for this measurement, linearity was maintained by inserting a calibrated neutral density filter to reduce the signal level to the same order as that of the low-angle scattered light, without a filter. The mirror was then rotated about a vertical axis to determine the variation of scattered light as a function of the angle of scatter. An alternative method, indicated in Fig. 3, was also tried. It allows a more accurate determination of the integrated radiation within a solid angle centered on the axis. An opaque plane reflector diverts the direct light away from the axis, while scattered light is focused by the field lens to the photomultiplier. However, in practice this type of test proved to be less convenient than that of Fig. 3, the method finally used for all measurements described in this section.

Figure 4 shows the measured dependence of the normalized scattered radiance, N/N_o, on the angle of scatter, θ_s, for primary mirror #3, the best, and #5, the worst, of the six coronagraph-quality mirrors tested before the balloon flight of February, 1971. Also shown is the corresponding curve for mirror #1, which was finished with only a normal-quality polish. Mirrors #6 and #7 were used for this balloon flight. On landing, the surfaces were splashed with mud. Mirror #7 was carefully cleaned using first a detergent solution and then by rinsing with distilled water. It

is revealing that its remeasured value, 7b of Fig. 5, showed only a relatively small increase in scattered radiance from the pre-flight measurement, 7a, compared with the characteristic curve of mirror #1.

Consecutive scatter tests of each of the coronagraph mirrors has provided a valuable history of mirror performance. Further measurements are presented in Table 2a-e. It can be seen that the original hierarchical order persisted. The results prompt a tentative conclusion: the substrate microstructure is the dominant parameter characterizing the mirror scattering function.

The implied relevance of these results to the coronagraph optical performance follows from the applicability of the scattering reciprocity theorem:[62] loosely formulated, it states that the reflected field at a point A due to a source at B equals the field at B when the same source is at A. The test itself also relies on this assumption since to sample the scattered field, the mirror is rotated while the detector remains fixed. Some independent, corroborative tests are now described.

It is useful to categorize the typical sources of scattered radiation of an evaporated metallic film as follows:

1. Superficial contaminants such as dust and organic films.
2. Discrete points in the film surface, such as particles remaining on the substrate after cleaning that are coated by the film, macroscopic particles that lodge on the surface during evaporation, and pinholes.
3. Irregularities in the film surface conforming to those of the substrate.
4. Microstructure in the film.

5. Intrinsic properties of the film material.[63]

Some simple tests are now described that have been used to differentiate, at least partially, between these different scattering sources.

Dark-ground test. If light from an intense source such as the Sun, an arc lamp, a laser, or a compact-filament lamp such as a "sun-gun" is focused at the reflecting surface, with the surface positioned such that the specularly reflected light just fails to enter the eye, both discrete scattering points (categories 1 and 2 above) as well as any general background-scattering are clearly visible, particularly if the surface is viewed in a darkened room. An improvement on this direct test is to use the optical system of Fig. 6, which produces dark-ground illumination. The direct beam is blocked by an opaque stop, a black spot supported by the mica sheet, while the adjacent lens forms an image of the test surface in the photographic plane. The coronagraph mirrors were examined by this method and photographic records of the field distribution obtained. Typically, both a field of *star-like* points distributed uniformly across the surface, and a lower-radiance uniform background, were evident. Increasing the angle of incidence at the mirror revealed that whereas the background uniformly diminished, some bright points only then became evident. This behavior was attributed to specular reflection occurring at crystalline-like facets, in contrast to other points where the reflected radiation has diffuse properties. Figure 7a-d consists of photographic records that illustrate the central dark-ground field for scattering angles, θ_s, of approximately 0°, 1°, 2°, and 4°, respectively, using the optical system of Fig. 6. The cause(s) of the observed points was not identified; categories 1 and 2

in the above list suggest several possibilities, all of which can be avoided using modern equipment and clean-room facilities. In any case, evidence cited below indicates that the integrated uniform background constitutes the major source of scattering.

Phase-contrast test. The coronagraph mirrors were further tested by phase-contrast; this reveals micro-structure of the polished surfaces (category 3 above). For this, the optical system of Fig. 8 was used.

Phase-contrast, as described by F. Zernike[64] for use in microscopy, linearly converts a spatial phase modulation to a spatial intensity modulation, apart from an additive constant. A wavefront reflected from a mirror has local phase variations impressed on it, corresponding to localized regions of path-difference, and the test is applicable here also.

If phase shifts due to a phase object are very small, a wavefront so modulated is, to a first order, equivalent to a direct (unmodulated) and a diffracted component in phase-quadrature. According to the theory of Zernike's test,[65,66] phase objects are rendered visible by adding a phase increment (via a "phase-plate") of $\pi/2$, or $3\pi/2$, to the direct light; the sensitivity increases if, as well, the phase plate attenuates. It is now shown that an attenuating disk that produces a phase change of π, or zero, also produces an intensity modulation.

Consider a pure phase object such as a reflecting surface having local departures, $s(u,v)$, from a mean surface, where (u,v) are coordinates in the object plane. The amplitude reflectance has the form, $r(u,v) = e^{i\phi(u,v)}$, where $\phi(u,v) = \frac{4\pi}{\lambda}s(u,v)$. A reflected wave therefore has impressed on it phase irregularities of the form $f(u,v) = e^{i\phi(u,v)}$.

For $\phi(u,v) < 1$, we have

$$f(u,v) \approx 1 + i\phi(u,v) - \frac{\phi^2}{2}(u,v), \tag{1}$$

the first term representing a direct component, and higher terms diffracted components.

Assuming unit magnification, and neglecting the finite extent of the pupils of the system, we have, in the transform plane (conjugate plane to the source),

$$F(\xi,\eta) = \delta(0) + iT\{\phi(u,v)\} - T\{\frac{\phi^2}{2}(u,v)\}, \tag{2}$$

where $T\{\ \}$ represents the Fourier transform operator.

A filter with an amplitude transmittance function

$$T(\xi,\eta) = \begin{cases} te^{i\alpha}, & \text{over the region } \delta(0) \\ 1, & \text{otherwise} \end{cases},$$

where $\alpha = 0,\pi$, is inserted in this plane. The emergent field is

$$F'(\xi,\eta) = t\delta(0) + iT\{\phi(u,v)\} - T\{\frac{\phi^2}{2}(u,v)\}. \tag{3}$$

In the image plane of the object, the final transform is,

$$f'(u',v') = t + i\phi(u',v') - \frac{\phi^2}{2}(u',v'). \tag{4}$$

The intensity,

$$I(u',v') = |f'(u',v')|^2$$
$$\approx t^2 + (1 - t)\phi^2(u',v'). \tag{5}$$

The intensity is thus proportional to the square of the phase, apart from the additive constant, while the contrast, γ, in the image is, for $t > \phi, \gamma = \phi^2(1 - t)/t^2 \approx \phi^2/t^2$, with $t << 1$.

For a Zernike $\pi/2$-phase-disk, the intensity is[65]

$$I(u',v') = t^2 \pm 2\phi t,$$

and

$$\gamma = 2\phi/t.$$

For $\phi > t$, the image contrast in the case of a π-, or 0-phase-disk equals

that for a $\pi/2$-phase-disk when $\phi = 2t$. If $t = 0.03$, a realistic value, this corresponds to a surface irregularity of depth $s = 3.0$ nm ($\lambda = 632.8$ nm). From equation (4) above, the direct and diffracted components are balanced when

$$|t| = \left|i\phi(u',v') - \frac{\phi^2}{2}(u',v')\right|,$$

or $t \approx \phi$, the condition for unit contrast. Then for $t = 0.03$, $s = 1.5$ nm. Irregularities having smaller values of s would be visible, but with reduced contrast. Evidently, if linearity is not demanded, a $\pi/2$- (or $3\pi/2$-)phase-changing disk is not essential to observe phase-structure. We conclude that, contrary to what is sometimes implied, phase objects are observable with any coherently illuminated imaging system in which the direct and the diffracted light follow separate paths--an interferometer--providing only that the components have approximately equal amplitudes. In the system indicated in Fig. 8, we then expect phase variations due to the mirror surface to be visible simply by inserting an appropriately absorbing disk. Such a test would be adequate to rank the mirrors on the basis of the quality of the smoothness of the polish.

The phase-shift requirement was investigated, since, without a thin-film thickness-monitor, it was not possible to manufacture phase-disks from evaporated films of dielectric/metal stacks, as described in the literature.[67] Therefore, absorbing disks, 0.3 nm diameter, were prepared by evaporating gold onto a mica substrate, covered by a metal mask; these disks were found to give excellent results for $t \approx 0.03$. Subsequently, the phase shift, α, due to such disks, was measured, where for a film of thickness d, and a phase change, δ, through the film, $\alpha = 2\pi d/\lambda + \delta$; for $d \gtrsim 60$ nm, $\delta \approx \psi_1 + \psi_2 - 2\pi nd/\lambda$, where ψ_1, ψ_2 are the phase changes at

the film surfaces, and n is the real component of the complex index.

The method of measuring α was that described by R. Fleischmann and H. Schopper,[68] in which a set of three slits is coherently illuminated, and interference in the far-field diffraction pattern observed with an eyepiece. The thin-film sample is then positioned to cover the central slit (the substrate covers all slits), and a polarization technique used to equalize the amplitudes transmitted through the central slit, and the outer two slits combined. An identical pattern is again observed, but displaced along the axis. The displacement is a measure of the phase shift. By this means, the phase-shift was found to be $\alpha = 0.85\ \pi$ radians ($t \approx 0.03$), a value considerably different from that for a linear transformation.

Referring to Fig. 8, the mirror surface is illuminated by a low-power laser; a phase-disk is located at the source image. The adjacent lens focuses the diffracted light to the photographic surface. Figure 9a-e consists of phase-contrast images of the coated primary mirrors. These patterns reveal imperfections in the substrate surfaces--cleaning and recoating left the patterns unchanged. Mirror #1, finished with a normal- (or low-) quality polish, evidently has polishing grooves across its surface, following two preferred directions. Coronagraph mirror #3 obviously has the smoothest surface; mirrors #4 and #8 are difficult to differentiate by this test; mirror #5 has the greatest roughness. This is the same ranking obtained from the scattered-light measurements. The previous tentative conclusion--that, at least for gold films in the visible, the substrate roughness substantially determines the magnitude of the scattered flux--is therefore supported. This conclusion may not be valid

at smaller wavelengths, however. Stanford *et al.*[69] have studied the u.v. properties of silver films on supersmooth substrates. They found evidence from plasmon excitation that indicated that film roughness is associated with the films themselves, and not with the substrate.

Mica-substrate tests. Imperfections in the substrate, whether intrinsic or due to contamination, make the inherent contribution to scattering of the evaporated film itself (categories 4 and 5 above) difficult to separate out. Ideally, a *perfect* substrate--free from microstructure and contaminants, is required. High-quality, free-splitting mica can be cleaved such that there is no contact with the surface by any material (other than air), thus providing a surface that closely approaches the required ideal. (Attempts to cleave mica under vacuum and coat the surface before exposure to air, were unsuccessful; it was found that mica will not cleave in a low-pressure environment.) Measurements have been made of the angular dependence of scattering from mica surfaces coated with the three obvious candidates for the coronagraph mirrors--gold, silver, and aluminum. The results are indicated in Fig. 10. These measurements were near the limit of the detection system, in which the diffraction field of the test system and air-borne dust probably made a significant contribution. The broken line represents the corresponding curve for coronagraph mirror #3 (Fig. 4). The direct focus test revealed little or no scattering whatsoever.

It was found that an aluminum film, examined by the focus test, had a substantial amount of scatter at large angles of incidence of evaporation. This appears to provide a direct measure of inherent scattering of the film. Where compound films were prepared such as gold/

aluminum, with gold as the top layer, increased scattering, indicated in Fig. 11, was evident. On the same figure, the two gold/lead curves correspond to measurements made on two different parts of the same substrate; the difference apparently due to variations in the granularity of the thin lead layer with thickness, or with angle of incidence of the evaporant. It is recognized that a crystalline substrate may result in a film structure, even without epitaxy, that is different from that possible with a glass substrate. Nevertheless, the results obtained with a mica substrate are indicative of the limitation on scattering imposed by the properties of the thin film itself. Mica has a further advantage: it can be cleaved after evaporation to gain an accurate measurement of scattering at the film/mica interface.

In summary, it is possible to produce coated mirrors suitable for use as near-infrared coronagraph objectives. All tests described above support the hypothesis that the smoothness of a mirror substrate is the dominant parameter determining its scatter function. Since the phase-contrast tests reveal residual substrate imperfections, and since the mirror coatings were prepared without clean-room facilities and without modern evaporation equipment, it is concluded that it should be possible to prepare coronagraph mirrors with significantly superior properties to those achieved here.

CHAPTER III

BALLOON-BORNE EXPERIMENTS

Introduction

Stratospheric observation of the solar corona avoids almost all atmospheric absorption, emission, and scattering, and the degraded seeing that limit the quality of ground-based instruments. However, even at stratospheric altitudes, detection of the outer corona is feasible only where instrumental extraneous radiation is exceedingly small. The crucial function of the coronagraph occulting system has been discussed in Chapter II. But even with an externally-occulted system, the problem is severe since unlike eclipse conditions, surfaces of the balloon-package exposed to direct sunlight constitute local sources of large radiance that can give rise to significant levels of stray radiation close to the system field of view. Effective shielding is therefore essential, a more stringent requirement for a mirror system than for a conventional lens-type coronagraph. In this respect alone, observation of the outer corona from a balloon platform constitutes an extremely difficult experiment.[70] Moreover, balloon-borne instruments are subject to design and operational constraints that do not apply to ground-based instruments; all on-board systems, mechanical and electronic, are required to function normally in a low temperature and pressure environment. Remote operation demands a substantially inflexible experimental program, except where exceedingly

complex logic is employed. Therefore, apart from significant hazards associated with a balloon-launch itself, and the flight, and package recovery, success in the form of useful data is not easily achieved.

The 1971 and 1973 balloon flights of the infrared reflector coronagraph sought to obtain data on the spectral radiance of the outer corona in the wavelength range of 2-4μ--in particular, to gain additional spectral and spatial information about the previously observed "peaks," of equivocal origin, and precise knowledge of the "background" elongation function. The coronagraph was designed to achieve a higher spatial resolution and cover a larger spectral range than previously obtained, with provision for simultaneous observations of the corona on opposite sides of the solar disk.

Balloon package. The stabilized balloon-platform for the coronagraph was that developed for a series of earlier balloon-borne experiments.[71] It has been described in detail elsewhere,[71-74] and will be discussed here only briefly. The basic components are a horizontal mounting plate, and beneath, a reaction wheel, both free to rotate on separate coaxial tubes about a central shaft that supports the complete system. The plate and reaction wheel are coupled through a d.c. torque motor, allowing azimuthal orientation of the suspended system by rotation of the reaction wheel. Electrical power supply in flight is from silver-zinc batteries, conveniently mounted around the circumference of the reaction wheel, substantially adding to its moment of inertia, since it is of lightweight construction. For the coronagraph flights, the mounting plate carried control and data instrumentation, protected by an insulated cover, and above, the

coronagraph multiple-axis mount.

The coronagraph optical system has been described in Chapter II. This system, and the associated external baffle assembly, mounted at the end of a conical boom, together comprise a single assembled unit approximately 6 m in length. For coronal observations, it is required that the axis of this unit is centered on the solar disk, preferably with high precision and stability, to optimize the accuracy of data reduction. Both these conditions were achieved on the two coronagraph flights discussed here.[61] Previous experience with balloon-borne instruments[71,72] revealed that a simple two-axis mount for the observing instrument is inadequate for accurate tracking, since continuous and comparatively rapid changes in the orientation of the balloon-package coordinate axes can occur, due to relative motion imparted to the package through package-balloon interaction. Both simple and torsional pendular oscillations have been identified, as well as transients and standing waves in the balloon train.[71,72] Methods have been devised to decouple, at least in part, the effect of such oscillations of the package from the target alignment of the observing instrument, by incorporating auxiliary axes.[71,72] The three-axis mounting system used for the reflector coronagraph is a modification of an alt-azimuth mounting, such that, over an azimuthal range of $\sim 5^{\circ}$, the coronagraph is free to rotate about an axis orthogonal to both its own longitudinal axis and the elevation axis. By this means, "cross-axis coupling" is reduced.[75] It is noted that a simple pendulum motion, in a plane perpendicular to the plane of the vertical circle containing the Sun, results in rotation of the

coronal fields of view along arcs concentric with the solar disk. For tracking, the platform is initially orientated so that the correct side faces the Sun; this is achieved by seeking a net null signal from sensors located at the corners of the mounting plate.[74] When this condition is achieved, a preprogramed timer activates similar sensors mounted on the end of the coronagraph boom for low precision acquisition of the Sun, and then, in turn, the control is switched to another set of sensors for high precision tracking.[61]

Recording systems. The amplified detector outputs were recorded as analog traces on three on-board photographic strip-chart recorders. These mirror-galvanometer systems are capable of simultaneously recording up to twelve channels. Each detector output was divided into four channels, covering a sensitivity range of approximately 45:1. A "marker" trace was also recorded. This trace provides an elongation scale for the detector fields-of-view. It is derived from the angular position of the cam that generates the primary mirror scan, as discussed below. Other channels were used to monitor the three tracking error-signals. Ten telemetry channels registered the same information on two strip-chart recorders and on magnetic tape (detectors #4, #5, and #6 only). Such records provide a convenient presentation of the general characteristics of the data. The on-board recorders have the advantage of proven reliability. The data is cumbersome to reduce however, particularly so, as the chart speed is non-linear. Provision was made to reduce the gain of any of the individual data amplifiers during flight, in the event that the coronal radiance proved to be unexpectedly high. On both flights,

however, the telecommand system failed to operate. The data amplifiers have a non-linear characteristic such that the amplified detector signal is proportional to the detector output (taken to be linear with incident radiant power over the operating range) only at small values. This circumstance applies to all flight data except for the small elongation part of the scans recorded in the October, 1971, balloon flight.

Calibrations

Spectral. The coronagraph design provides for triple spectral-band observations of the infrared corona on opposite sides of the solar disk. The filter/detector spectral responses (see Table 1) are shown in Fig. 12. The 2.2μ filters of detectors #1 and #4 are identical, as also the 2.5μ filters of detectors #3 and #6. The overlapping of these spectral bands is not ideal--filters that would have given completely isolated bands were not available however.

Spatial. The lateral separation of the three detectors in each optical system results in corresponding small relative angular displacements of the three fields-of-view. These displacements are therefore established by the geometry of the optical system, but can vary slightly with adjustments of the internal mirrors. Calibration was obtained by laboratory primary-mirror scans of a collimated slit or point source; such scans also provided a measure of the effective angular resolution, ~ 0.1 $R_\odot$ (except for detector #2, where the resolution is ~ 0.25 $R_\odot$). This value is approximately 40% greater than the angular dimension of the PbS detectors in the scan plane.

Since the image conjugate to the detectors was observed to be extremely astigmatic, it is concluded that alignment optimization, as gauged by optimum signal, resulted in the tangential image being focused approximately at the detector surfaces. Under this circumstance, the aberration causes an energy loss, but there is apparently little change in resolution. The magnitude of the angular scan range for all detectors corresponds to 9.56 $R_{\odot}$, fixed by the primary-mirror cam drive. The scan limits vary with the primary-mirror mechanical setting, adjustable via three micrometer support screws. These were set, for each system, such that at the primary mirror mid-scan position, the center detector response was maximum for a collimated incident beam inclined to the coronagraph axis at an angle equivalent to 8 $R_{\odot}$. Scan ranges are given in Table 1. An independent signal derived from the primary mirror cam was used to identify points in the recorded scans corresponding to maximum and minimum scan angles, as well as equally-spaced intermediate points. The registration of the angular field-of-view scale for the flight scans is uncertain within the range of static or dynamic tracking errors. It is noted that symmetry results in any such errors having equal and opposite values for the two optical systems. The vignetting characteristic of the external baffles, discussed in Chapter II, was measured for each detector by scanning the primary mirrors with an extended diffuse source located beyond the external baffles. For indoor tests, the source was a uniformly illuminated white surface. Sky scans were also obtained. These have the potential advantage that flight conditions can then more nearly be simulated. The data were mostly

inferior, however; it was found that the infrared sky radiance, even under cloudless conditions, is rarely constant in time. The laboratory vignetting ranges, for the balloon flight of 1973, are given in Table 1. It can be seen that vignetting does not commence at the same elongation angle for all detectors, apparently a result of aberrations and imperfect alignment. Since the image of the external posterior knife-edge has a width of approximately 3 mm in the detector plane, it is spatially unresolved.

Radiance. For a linear detector system and a source of radiance N, the detector output, $V_d \propto N$, where the proportionality constant is given by the system parameters and the detector power responsivity, R. Strictly the spectral power responsivity, R_λ, should be used. However, to a close approximation, R is constant over the effective spectral band of the coronagraph detectors. To determine R, a commercial black-body source of radiance $N_{bb}(\lambda,T)$ was used to irradiate a diffusely reflecting surface--a gold-coated coarse-ground glass plate of diffuse reflectance r. The plate was positioned, in turn, a few centimeters from the entrance aperture of each of the coronagraph optical systems, such that it overfilled the combined detector fields of view. The rms radiant power incident on each detector is then given by, $P_d = A_d' t_s \sum_\lambda H'(\lambda) t_f(\lambda) \delta\lambda$, where the irradiance at the primary field stop is, $H'(\lambda) = \pi r N_{bb}(\lambda,T) \sin^2\theta \sin^2\phi$. A_d' is the area of the detector image in the plane of the field stop, t_s is the system transmittance (up to the detector filter), $t_f(\lambda)$ is the filter transmittance, θ is the semi-angle subtended by the black-body aperture at an axial point on the plate, and ϕ is the semi-angle subtended by the

primary mirrors (for an equivalent circular aperture) at the field stop. Measurements of the corresponding detector outputs give R values. These are given in Table 3, together with corresponding D* measurements. The effective reflectance, r, of the scatter-plate was determined as indicated in Fig. 13. A diffuse source S (a tungsten-filament lamp positioned indirectly in a diffusely reflecting enclosure) of aperture A_1 and radiance N was placed at a distance d_1 from the scatter-plate along the normal direction ab (Fig. 12). The aperture A_2 defined an appropriate solid angle A_2/d_2^2 subtended at the aperture A_3. Radiation passing through A_3 was measured by a photomultiplier mounted in a MgO-coated integration sphere of aperture A_4. The radiant power at A_4 is $P_1 = eNA_1A_2A_3/\pi d_1^2 d_2^2$, where e is the efficiency with which the plate directs radiation towards A_2 compared with that of a Lambert surface. A second measurement was then made with the scatter-plate replaced by the source. For this case, the power at A_4 is $P_2 = NA_2A_3/d_2^2$, and the ratio of the measurements, $m = P_1/P_2$, gives $e = m\pi d_1^2/A_1$; from measurements, e = 0.62. Then $r = er_{ir}/r_v$, where r_v and r_{ir} are the reflectances of an evaporated gold film at visible and the relevant infrared wavelengths, respectively. Since $e \sim r_v$, the diffuse reflectance, r, is approximately equal to the specular reflectance, $r_{ir} \approx 0.98$.

A particular feature of the reflector coronagraph is the provision of an auxiliary entrance aperture and associated optical system, as described in Chapter II. By this means, during each chopper cycle, the detectors have alternate views of the coronal field, and the stratospheric sky, remote from the Sun. This allows at least partial

correction of the observations for the contribution due to sky radiance. The correction is probably incomplete since measurements in the visible at an altitude of 25 km indicate a residual enhancement of sky radiance in the solar direction;[50] but this enhancement decreases with increasing wavelength, and inferred values in the infrared indicate complete absence of an aureole, at 3.5μ.[50] Subsequent infrared sky radiance measurements, N_s, were obtained at an altitude of 28 km, within 3° of the solar disk.[38] The results, corrected to zenith, gave $N_s(2.2\mu) \sim 2 \times 10^{-10} N_\odot(2.2\mu)$, where $N_\odot$ is the mean solar radiance. In view of these results, any instrumentally uncorrected sky-radiance component of the observations reported here is assumed negligible, particularly since both balloon flights were at altitudes in excess of 28 km. Further evidence to support this conclusion is presented below.

Results

The two coronagraph balloon-flights have provided a large quantity of infrared data. In addition, the similarity of the two experiments in terms of instrumentation and flight conditions has provided a valuable opportunity for data comparison. Table 4 presents parameters of these two balloon-flights. The coronal radiation detected over the outer portions of the scans (approximately 6 to 13 $R_\odot$) is believed to be substantially uncontaminated by non-coronal radiation. The inner portions of the scans require a vignetting function correction. Ambiguities over this scan range have resulted from calibration uncertainties associated with this correction, coupled with the possibility of extraneous radiation.

The number of useful scans recorded is set out in Table 5. In many cases, however, these are only partial scans. For the 1971 flight, the signal from detector #5 was positive only over the extreme inner part of each scan; the outer portion of the scan was unrecorded. A negative signal occurs when the reference radiant flux, derived from the auxiliary optical system which views the stratospheric sky (as described above), exceeds the coronal radiant flux. A possible explanation is that thermal emission of the chopper blades, uncooled by convection, resulted in a net reference radiance greater than that of the corona--the spectral range of detector #5 (3-4 μ) makes it more sensitive to thermal emission from instrumental surfaces than the other detectors. The outer portions of the scans of detector #4 have measurable values only over the last ten scans.

The two scan intervals are characterized by a marked difference in signal level. The outer portion represents detector outputs of only a few microvolts, but even at the scan limit, this is substantially greater than the rms noise in most cases. An abrupt increase in signal level distinguishes the inner portion, where the detector amplifiers were operating in the extreme non-linear region of their gain curve. At least part of this high signal is attributed to extraneous radiation. Reduction of this portion of the data has proved to be extremely difficult.[75]

The 1971 balloon-flight had an exceptionally low ascent rate, attributed to water vapor accretion on the balloon surfaces during launch. The tracking and data recording, preprogramed for float conditions, commenced during ascent at an altitude of approximately 27 km. Float altitude was reached at a time corresponding to scan #22. All six data channels display marked noise-like features, positive and negative, at random

intervals up to scan #22; none occur in later scans. In most cases, they appear simultaneously in time for all detectors and with constant relative amplitudes between the three detectors of each set. A possible explanation therefore is that near-field reflecting particles were recorded as they passed through the fields of view of both the primary and reference optical systems, during ascent. This noise has rendered the outer portions of the first fifteen scans unsuitable for reduction. It is noted that particle tracks have been recorded in photographs obtained with a white-light balloon coronagraph.[48] The tracks were attributed to particles freed from the balloon and gondola surfaces.

A further characteristic of this data is that the inner scan interval increases continuously to a maximum value at approximately scan #36. The increase represents a change of approximately 20%; following scans show less change, varying from detector to detector. The signal levels near the maximum scan range do not display the same characteristic, although a small increase occurs over the first 30 scans for detectors #1, #3, and #6. There are several obvious possibilities for the origin of such variations. Maximum solar elevation corresponded in time to scan #36, while the projected radial direction of the coronal region scanned was parallel to the ecliptic at approximately scan #42. The possible influence of backscatter from a cloud deck was also considered. From ATS satellite cloud-cover photographs, densitometry traces were obtained corresponding in time and position to the balloon-flight path, for equivalent base diameters of 35 km and 100 km. These show a prominent peak, equivalent to almost total cloud cover, which, at its maximum value, corresponds in time to scan #34. The integrated cloud cover during the first few scans was,

however, greater. The complexity of the instrumentation does not allow a definite conclusion with regard to the cause of the observed changes in the scans during the flight. Nevertheless, it is considered that the close temporal correlation of maximum solar elevation and/or cloud cover with maximum observed spread of the inner portion of the scans is not coincidental, and that extraneous radiation contributed at least, in part, to the high signal level recorded over the inner range. This reasoning would be suspect if the atmospheric extinction, t_{ex}, was significant; but for a zenith optical depth, $\tau_t(\lambda=2.2\mu) = 0.05$,[38] the change in t_{ex} during the period of observation would be ~ 1% only. The increase in signal level of the outer scan portion, as noted above, occurred also in the balloon flight of 1973. An instrumental origin cannot be excluded, such as drifts in the amplification system. The sensitivity of the PbS detectors increases above the temperature of liquid nitrogen, before decreasing at higher temperatures. However, on the initial balloon-flight of this coronagraph, under similar conditions, the detector temperature was monitored and found to remain constant.

The photographic strip chart scans were digitized at intervals of 0.04 $R_\odot$. The outer scan portions were divided into approximately two equal groups, and each averaged. The results, calibrated in units of solar radiance, $N_\odot$, are plotted in Figs. 14 and 15. Peaks in the coronal radiance at 8.7 $R_\odot$ and 9.2 $R_\odot$, as observed by MacQueen,[38] were not recorded. Since these outer portions of the scans are believed free from extraneous radiation, and the signal level is typically much greater than the noise, and since there is evidence from the scans that angular resolution remained unchanged from the pre-flight calibration, it is

concluded that the previously observed peaks display a temporal variation. Several possible correlations of *apparent* brightness variations of the zodiacal light have been suggested, including comet activity and the 11-year solar cycle activity, but observations have not reliably confirmed such relationships.[37] If, however, they do exist, by extension the F- and T-coronas could be expected to demonstrate variations also. It is noted that the observations reported here were carried out near sunspot minimum, while the first observations of the peaks[35,38] were at a time close to sunspot maximum. However, a subsequent observation at the total eclipse of 1970 also revealed an enhancement at 4 $R_{\odot}$, at three near-infrared wavelengths.[39]

As discussed in Chapter II, the optical system for the 1973 flight was modified to incorporate scanning internal knife-edged baffles. By this means, the image of the external baffles was occulted. Useful data was obtained only from detectors #4 and #6, and, due to a shift in the zero level, most scans do not extend to the full scan range. The general characteristic of the scans are similar to those obtained in the previous flight, with the exception that the signal level decreases over the inner portion of the scans, due to the vignetting effect of the internal baffles. The data was reduced by the same procedure as that used previously. It is apparent from the results that the vignetting function which applied during the observations is different from that obtained just prior to the flight. This has resulted in some uncertainty in the exact form of the appropriate correction. Hence the reconstructed data was not obtained with high precision over the inner part of the scan, the possible error greatest at the smallest elongation. The averaged results, for both

detectors, are shown in Figs. 16 and 17. As before, no peaks were observed at 8.7 $R_\odot$ and 9.2 $R_\odot$. Variations from a smooth elongation function near minimum scan are possibly real, but could be artifacts of the curve reconstruction which is extremely sensitive to the form of the vignetting correction function in this region. It is noted that there is a close similarity in the form of the radiance distribution obtained in the two flights, for corresponding detectors. At a wavelength of 2.2 μ, the radiance of the continuum corona, as determined by Peterson at the total solar eclipse of 1966, was 3.0×10^{-9} $N_\odot$ at an elongation of 5 $R_\odot$. For the same eclipse, MacQueen derived a value of 4.4×10^{-10} $N_\odot$, for scans parallel to the ecliptic, while the present observations give a corresponding value of 7.2×10^{-10} $N_\odot$.

CHAPTER IV

ECLIPSE EXPERIMENT

Introduction

During the total solar eclipse of June 30, 1973, a ground-based telescope was used to observe the corona at a wavelength of 1 μ. The telescope was provided with twin detection systems which allowed simultaneous scans of the corona on opposite sides of the solar disk.

The observation site was Loiyengalani, Kenya, on the southeastern shore of Lake Rudolf, with coordinates, latitude 2° 44.7' N, and longitude 36° 42.4' E, approximately 18 km north of the eclipse center line, or ~ 0.15 of the eclipse-path half-width; elevation 455 m above msl. Second contact occurred at 12 h 57 m 25 s U.T., with a totality duration of 294 s. The mean solar elevation during totality was 37°; azimuth 297°. Sky conditions in the solar direction were clear; the closest visible clouds were small remnants of evaporating cumuli beyond 20° from the Sun.[76]

Instrumentation

The telescope was a 40-cm aperture, $f/4.5$ reflector, equatorially mounted. The optical system is indicated in Fig. 18. Twin plane secondary mirrors each direct off-axis incident beams to independent, nominally identical detection systems. The centers of the corresponding two fields of view are displaced in right ascension, approximately

symmetrically about the principal axis and mutually inclined at an angle equivalent to 5.6 $R_{\odot}$. In each detection arm a rectangular field stop is located a few millimeters from a 400-Hz Bulova chopper set in the primary image plane. These two components together determine the angular field of view--2.4 arc min parallel to the scan, and 4.8 arc min normal to this direction. A fused-silica lens, operating at a conjugate ratio of 3:2, relays the primary image through a filter to the photocathode of a dry-ice-cooled photomultiplier. The photocathode has a sensitive area of approximately 5 mm^2. The output is synchronously rectified and displayed on a chart recorder.

The photomultiplier detection system which views eastward of the Sun (with the primary axis centered) is designated D_e, and that which views westward, D_w. Both photomultipliers have an S-1 spectral response. They were individually selected for their exceptionally high long-wavelength sensitivity. The overall spectral response is the product of filter transmittance and the response curve of the photomultipliers. As shown in Figs. 19 and 20, the effective spectral bandpass half-width for D_e is 0.14 μ, and for D_w, 0.17 μ, both centered at 1.03 μ.

Experimental Procedure

The corona was scanned in right ascension at a constant rate of 10 arc min per second. The scan was controlled visually by monitoring the inner corona with an attached sighting telescope fitted with a graticule graduated in solar radii. At intervals of image movement corresponding to one solar radius, a foot-operated switch was pressed to produce a pulse on the strip chart. A sequence of such pulses formed

a scale in units of solar radii, giving the orientation of the telescope relative to the solar disk, and hence, the corresponding angular view of each detection system.

Figure 21 indicates the scanning program followed during the period of totality. The telescope was first directed west of the obscured Sun to a maximum elongation of 6 $R_\odot$; at this instant D_e was viewing an elongation of 3.9 $R_\odot$ west, and D_w an elongation of 9.5 $R_\odot$ west. The scan was then reversed until an opposite maximum elongation of 6 $R_\odot$ was achieved. At this instant, D_e was viewing an elongation of 8.2 $R_\odot$ east, and D_w, 2.6 $R_\odot$ east. The scan was again reversed, and so on. Each detector therefore scanned partly into the opposite coronal region, as indicated in Fig. 21; this provided a direct measure of the radiance difference between the two regions. Twelve complete scans were recorded on the east side, spanning the range 1.7 $R_\odot$ to 8 $R_\odot$, and fourteen on the west side, from 2.9 $R_\odot$ to 9 $R_\odot$. The minimum useful elongation was determined by amplifier saturation, and therefore by the amplifier gain; this was changed several times during the period of observation. The relative orientation of the diametral scans across the solar disk with respect to the ecliptic is indicated in Fig. 22. Geocentric coordinates are identified in the figure.

Radiance Calibrations

The responsivity of the overall system was determined using a commercial blackbody as a calibrated source. The optical configuration is shown in Fig. 23. The blackbody aperture is located at the principal focus of a collimator mirror. This system, collimator and blackbody, is

rotated such that the radiation transmitted through the aperture stop, of area A_a, is aligned with one of the detection systems. The stop A_a serves to attenuate the incident radiation to a level within the normal operating range of the detectors. The image of the blackbody aperture overfills the telescope field stop, A_{fs}. The power responsivity, R, is derived from the calculated spectral radiance, $N_{bb}(\lambda,T)$, of the blackbody source at a known temperature, and the detector output, V_{bb}. For a telescope focal length, f_e, a system transmittance, t_s, and a filter transmittance, $t_f(\lambda)$, the responsivity is

$$R = \frac{C\ V_{bb}}{\sum_{\lambda} N_{bb}(\lambda,T)\ t_f(\lambda)\ \delta\lambda}, \text{ where } C = f_e^{\,2}/A_a A_{fs} t_s = 3.81 \times 10^6.$$

The derived values were, $R_e = 2.46 \times 10^8$ VW^{-1} for D_e, and $R_w = 8.36 \times 10^8$ VW^{-1} for D_w. The detector output recorded at eclipse can be converted by R to a corresponding coronal radiance, corrections being applied for atmospheric extinction and radiance.

An independent calibration in terms of direct solar radiance was carried out in the field. On several days preceding the eclipse, and on eclipse day prior to first contact and following fourth contact, measurements of detector output, $V_\odot$, were obtained when each detector viewed the solar disk. For this, a cover containing three symmetrically located holes was placed over the entrance aperture of the telescope. Each hole, of 1.18 mm diameter, was covered by two neutral-density gelatin filters. The total attenuation, k, of the cover, relative to an open telescope, was 3.87×10^{-8}. Thus, for coronal measurements, the detector output, V_c, is transformed to a corresponding fractional solar radiance by $kV_c/V_\odot$,

corrections again applied for atmospheric extinction and radiance. Alternatively, for a known source radiance, the corresponding detector output can be calculated. At a wavelength of 1 μ, Allen[77] gives a mean solar spectral radiance of $N_{\odot}(\lambda) = 1.08 \times 10^{3}$ W cm^{-1} sr^{-1} μ^{-1}. The calculated output, $V_{c,\odot}$, when a detector views the solar disk with the 3-aperture cover in place, is then given by:

$$V_{c,\odot} \approx Rk\frac{A_e}{A_a C}\, t_{ex}(\lambda,z)\, N_{\odot}(\lambda)\Delta\lambda,$$

where A_e is the effective aperture of the open telescope, $t_{ex}(\lambda,z)$ is the atmospheric extinction, and $\Delta\lambda$ is the effective spectral bandpass. The computed value $V_{c,\odot}$ can then be compared with the measured value, $V_{\odot}$, as a check on the entire calibration procedure.

To a close approximation, the atmospheric extinction, $t_{ex}(\lambda,z)$, is given by,[78]

$$t_{ex}(\lambda,z) = \frac{I(\lambda,z)}{I_{\odot}(\lambda)} = \exp\{-\tau_t(\lambda)\ \sec z\} + I_d(\lambda,z),$$

where $I(\lambda,z)$ is the observed solar intensity at zenith distance z, $I_{\odot}(\lambda)$ is the zero-airmass solar intensity, $I_d(\lambda,z)$ is the diffuse intensity detected, and $\tau_t(\lambda)$ is the total zenith optical depth. Neglecting $I_d(\lambda,z)$, $I_{\odot}(\lambda)$ can be derived by linear extrapolation of ln $I(\lambda,z)$ vs sec z, to sec z = 0, while the slope is $-\tau_t$. Since $I(\lambda,z) \propto V(\lambda,z)$, the above $V_{\odot}$ measurements can be used directly to evaluate $t_{ex}(\lambda,z)$. Accordingly, for the period of totality, $\tau_t(\lambda=1\mu) = 0.21 \pm 0.04$, and $t_{ex}(\lambda=1\mu, z=53^{\circ}) = 0.71 \pm 0.05$. The error estimates follow from significant variations in repeated measurements. The origin of these variations was not identified, but could have been due in part to short term variations in τ_t itself. For the same eclipse site, Shaw[76] found

$\tau_t(\lambda=0.5\mu) = 0.32$. The total optical depth is

$$\tau_t(\lambda) = \tau_r(\lambda)P/P_o + \tau_p(\lambda) + \tau_a(\lambda),$$

where τ_r ($\propto \lambda^{-4}$), is the Rayleigh-scattering optical depth, P is the atmospheric pressure at the point of observation, P_o is the atmospheric pressure at sea level (standard atmosphere), $\tau_p(\lambda)$ is the optical depth due to scattering and absorption by airborne particulate matter and water droplets, and $\tau_a(\lambda)$ is the optical depth due to selective absorption by polyatomic gaseous constituents of the atmosphere and continuum absorption by the integrated effect of the wings of the absorption lines distributed throughout the spectrum. Direct sampling of aerosols and extinction measurements at other sites[78] have shown that $\tau_p(\lambda)$ sometimes has a power-law wavelength dependence; then $\tau_p(\lambda) \propto \lambda^{-\varepsilon+2}$, $2 \leq \varepsilon \leq 4$, with a mode $\varepsilon \sim 3$. If such a relationship was applicable for the eclipse site conditions, the ratio $\tau_t(\lambda=1\mu)/\tau_t(\lambda=0.5\mu) = 0.66$ then indicates that $\tau_a(\lambda=1\mu)$ was not negligible. Independent field observations[79-81] tend to support this possibility. Tabulated values of water-vapor absorption coefficients, $c_i(\lambda)$, derived from solar observations,[82,83] indicate that overlapping at 1 μ of the 0.94-μ and the 1.13-μ water-vapor vibration-rotation bands could account for a measurable attenuation over realistic values of absorber path. For example, for an amount of precipitable water, w = 6 mm, $\tau_a(\lambda=1\mu) \sim c_i w \approx 0.10$. The 0.94-μ water-vapor band overlaps the spectral bandpass (Fig. 19, 20) of the eclipse telescope detection systems; hence the overall sensitivity of the eclipse observations to water-vapor absorption was much greater than that which applied at 1.0 μ. Detailed meteorological data was not available for the vicinity of the lake-shore eclipse site; due to a local circulation pattern associated with solar heating,

moist air ascends the slopes of the surrounding mountains resulting in convective cloud formation over the peaks, while air descending over the lake is relatively moisture-free.[84] It is concluded that the observation path across the lake contained relatively higher amounts of water vapor than is typical for such savannah-desert regions, and a relatively high value of τ_a for the total atmospheric path is therefore plausible.

For observations, $V_\odot$, made just prior to first contact, $\tau_t \approx 0.75$, and $V_\odot/V_{c,\odot} \approx 0.85$, for both detectors. The discrepancy is not considered surprising. Apart from a possible error in t_{ex}, the most likely source of error is thought to be in the attenuation constant, k, since its evaluation relied on the assumption of linearity in the transmittance measurement; moreover, the transmittance of gelatin filters can vary with time and temperature. It is noted that MacQueen[38] derived an experimental mean radiance, $N_\odot(\lambda=2.2\mu)$, 14% less than that quoted by Allen.[77]

During totality, both detection systems recorded several diametral scans of the lunar disk. These provided a measure of the combined contributions from earthshine, sky radiance and scattered radiation in the telescope system. A mean value of the visible earthshine at totality is, $N_{es} = 1.1 \times 10^{-10} N_\odot$.[77] Information on the wavelength dependence of the Earth's bond albedo, $A_\oplus$ is sparse.[85-88] The spectral variation of $A_\oplus$ between the visible and near-infrared is determined mainly by the atmospheric albedo. A coarse approximation is $A_\oplus(1\mu)/A_\oplus(\text{vis}) \sim 0.8$. The Moon's geometric albedo, p, increases approximately linearly with wavelength,[83] and $p(1\mu)/p(0.55\mu) = 1.7$. Adopting these values, and taking into account the difference in extinction between the two wavelengths, $N_{es}(1\mu)/N_\odot(1\mu) \sim 1.6 \times 10^{-10}$.

The sky spectral radiance during a total solar eclipse is a function of parameters such as those of the eclipse geometry, the altitude and direction of observation, the ground albedo, the atmospheric optical depth, and the upper atmosphere constituents including aerosols, which determine the scattering characteristics.[90-94] Cumulative observations indicate that the sky radiance increases with solar elevation in accordance with the sine-curve form of normal day-sky radiance variation; but prevailing atmospheric conditions can result in marked departures from this relationship.[91] The sky radiance typically changes asymmetrically during the period of totality with a minimum near mid-totality.[91] A comparison of ordinates, Y_ℓ, of the recorded lunar scans shows this characteristic, for both detectors; a minimum occurs at scan #4, with a monotonic increase to the last scan recorded before third contact. For D_w, $Y_\ell(\#4)$ corresponds to a radiance $N_\ell(\#4) = 1.54 \times 10^{-9}\ N_\odot$, and $Y_\ell(\#12)$ to $N_\ell(\#12) = 2.29 \times 10^{-9}\ N_\odot$; for D_e, $Y_\ell(\#4)$ corresponds to $N_\ell(\#4) = 1.51 \times 10^{-9}\ N_\odot$, and $Y_\ell(\#12)$ to $N_\ell(\#12) = 2.33 \times 10^{-9}\ N_\odot$. Subtracting the component, N_{es}, due to earthshine, gives the ratios: $(D_w)\ N_s(\#12)/N_s(\#4) = 1.54$; $(D_e)\ N_s(\#12)/N_s(\#4) = 1.61$, a mean of 1.58. Sky radiance measurements obtained by Shaw[76] at the eclipse site also reveal the same characteristics. These measurements were in the form of scans in the solar vertical plane, at wavelengths of 0.4 μ and 0.6 μ; within 2° west of the solar disk (corresponding approximately in time with scan #4 and #12 of the eclipse data), the ratio of maximum to minimum sky radiance during totality is $\gamma \sim 1.57$, for both wavelengths. Since γ cannot be determined with high precision from the published graphs,[76] its concordance with the mean of the ratios derived from the lunar scans, given above,

is in part coincidental. Nevertheless, it indicates that scattered radiation within the eclipse telescope, as detected, was at most small and probably negligible. Since N_ℓ is approximately twice the radiance recorded at 8 $R_\odot$, it follows that the sky radiance varied in elongation. While measurements of the stratospheric aureole display a zero gradient within approximately 6 $R_\odot$ of the solar disk,[50] ground observations can show a pronounced gradient due to large aerosols.[95] The eclipse sky, measured 14 minutes prior to totality, revealed an enhancement of diffuse radiation near the Sun;[76] a measurable forward scattering of coronal energy by large aerosols ($r > 1\mu$) is therefore not precluded. The above lunar-scan results,however, force the conclusion that the component of sky radiance originating in such a process displayed the same temporal changes as the general sky background. This conclusion is supported by the results of O. Koutchmy and S. Koutchmy.[96] They show that under non-ideal sky conditions the coronal aureole radiance can be comparable with that of the F-corona itself. The same conclusion follows from an analysis of the coronal scans themselves. Comparison of corresponding ordinates, Y_i, of the coronal scans shows a minimum at scan #6, with a continuous increase to the final partial scan at the termination of totality. The D_w ratios, $Y_i(\#14)/Y_i(\#4)$, given in Table 6, are approximately constant for elongations smaller than 6.5 $R_\odot$; hence the temporally increasing component, S_i, of the signal is, over this angular range, approximately proportional to the total signal, Y_i. Adopting the relationship, $S_i(\#12)/S_i(\#4) = 1.57$, where S_i is taken to be the sky-radiance signal, the angular function of sky radiance over the scanned region can be extracted and the recorded coronal data corrected for this spurious component.

Hence, for a coronal signal, C_i, $S_i = Y_i - C_i$, and $C_i = \gamma\{Y_i(\#4) - Y_i(\#12)\}/(1-\gamma)$, where $\gamma = 1.57$. This formula is applicable to the data only beyond ~ 3.5 $R_\odot$, the inner limit of scan #4 for both detectors. Interpolation of data from other scans has been used to obtain values at smaller elongations. Values of C_i so derived have been converted to equivalent fractional solar radiances.

The mid-totality sky radiance values given by Shaw,[76] at an elongation ~ 9 $R_\odot$, are $N_s/N_\odot(\lambda=0.4\mu) = 7.9 \times 10^{-10}$, and $N_s/N_\odot(\lambda=0.6\mu) = 3.0 \times 10^{-10}$, a wavelength dependence of $\lambda^{-2.36}$. A corresponding dependence, $\lambda^{-2.5}$, was found in previous stratospheric sky measurements.[50,51] This close agreement gives confidence that the exponent of -2.5, derived from the latter measurements for the spectral interval, 0.6 μ to 1.0 μ, was also appropriate for the eclipse sky; it predicts a radiance $N_s/N_\odot(\lambda=1.0\mu) \sim 0.8 \times 10^{-10}$. Application of the above formula for C_i leads to a value of $N_s/N_\odot(\lambda=1\mu) = 4.0 \times 10^{-10}$ at 9 $R_\odot$. The discrepancy is of concern. It is noted, however, that the sky radiance values given in ref. 76 are unusually small for low-altitude observations,[90,92] particularly for a sky recognized visually as inferior to that at some other eclipses.[76]

Results

The observed coronal radiances, $N_{c,e}$, measured east of the solar disk, and $N_{c,w}$, measured west, corrected for atmospheric extinction and sky radiance, are plotted in Figs. 24 and 25. A gradient discontinuity occurs at 1.95 $R_\odot$ (Fig. 24), evidently a direct observation of the elongation at which the K- and F-coronas interchange dominance, in

approximate agreement with white-light coronal models. From 1.8 $R_\odot$ to 1.9 $R_\odot$, the derived gradient is -6.8, and from 1.95 $R_\odot$ to 2.7 $R_\odot$, -4.8. The mean gradients between 5.5 $R_\odot$ and 8 $R_\odot$ are, -2.50, for $N_{c,e}$, and -2.42, for $N_{c,w}$, in close agreement with the quoted value of -2.5 for the F-corona elongation dependence.[77] Representative values of $N_{c,e}$ and $N_{c,w}$ are given in Table 7 ; also included are radiances derived from observational models of the (K + F)-corona, as given by Saito[98] and van de Hulst,[97] designated $N_{K+F}(1)$ and $N_{K+F}(2)$, respectively. As pointed out in the previous section, some of the calibration factors involve significant uncertainties and the magnitude of the observed coronal radiance is correspondingly imprecisely known; the relatively close agreement between the N_c and N_{K+F} values given in Table 7 is therefore not necessarily valid. However, large possible errors have little effect on the form of the angular dependence, and the similarity leads to the conclusion that thermal emission from circumsolar particles was not explicitly detected. This is consistent with Peterson's[23] calculation of the thermal emission spectrum of such particles, based on the model of Ingham.[99] For interplanetary particles of radius, a, and solar distance, r, Peterson used the distribution function, $n(a,r) = Ca^{-p}\,(D/r)^{q}da$, where p and q are population indices, and C is a constant determined by the space density at D = 1 A.U. He assumed a wavelength independent albedo, A, and a particle temperature dependence of the form $T(r) = \kappa(D/r)^{0.5}$, where $\kappa = 280(1-A)^{0.25}$ K. At λ = 1.0 μ, and an elongation of 4.5 $R_\odot$, evaluation of the column integral for $C = 2.5 \times 10^{-26}$, p = 4, q = 1.5, A = 0.39, predicts a thermal emission radiance, $N_T(\lambda=1\mu) \sim 0.3\, N_{K+F}(\lambda=1\mu)$. Beyond $\lambda \sim 2\ \mu$, thermal emission is the dominant component. It is noted, however, that MacQueen[38] found that both scattered radiation and thermal-emission models, adjusted with

plausible parameters, could be made to fit his 2.2-μ continuum coronal observations beyond 5 $R_\odot$.

Table 8 lists the ratios $N_{c,e}/N_{K+F}$, $N_{c,w}/N_{K+F}$, and N_c/N_{K+F}, where $N_{K+F} = \{N_{K+F}(1) + N_{K+F}(2)\}/2$, and $N_c = (N_{c,e} + N_{c,w})/2$. It is evident that a small deficit in the observed values of coronal radiance, compared with N_{K+F}, occurs for elongations over the range $2 < \rho < 4.5$, where $\rho = R/R_\odot$, where R is the angular distance in units of solar radii. In an analysis of the visible F-corona, van de Hulst[19] assumed a uniform particle space density beyond a vaporization region, void of dust particles, surrounding the Sun. His model predicted that the reflected component, $N_{F,r}$ would decrease with decreasing elongation within the particle-free region, while the diffracted component, $N_{F,d}$, would at first continue to increase, dependent on the magnitude of the scattering parameter, $2\pi a/\lambda$, and then also decrease in this region. In a subsequent analysis, Ingham[99] assumed a circumsolar dust-free region extending to 4 $R_\odot$, and investigated $N_{F,d}$ employing two distribution functions, including n(r,a), given above. For this, and $\lambda = 0.63$ μ, $1 \leq \rho < 4$, the best fit to values derived from observations in the visible was found to be for $p = 4$, $q = 1.5$, and $a_1 = 0.4$ μ, where a_1 is the minimum particle radius. The agreement is relatively poor, except for $1 \leq \rho < 1.4$, where the gradients are approximately equal; for $1.4 < \rho < 4$, the gradient of the calculated function is much smaller than that derived observationally. Following Ingham,[99] $N_{F,r} \propto \text{cosec}^{1+q}\varepsilon \{\int_{\varepsilon}^{\theta} \sin^{-q}\theta \, d\theta + \int_{\theta_2}^{\pi} \sin^{-q}\theta \, d\theta\}$, where ε is the elongation, and θ is the scattering angle; θ_1, θ_2 are limits defined by the boundary of the dust-free region, such that $\sin\theta_1 = \sin\theta_2 = \sin\varepsilon/\sin\varepsilon'$, where ε' ($\rho'=4$) is the maximum elongation of the dust-free region. The increase in the

integral coefficient with decreasing ε is compensated by the decrease in the integrals with both decreasing ε and integration range. Hence $N_{F,r}$ is approximately constant for $2.5 < \rho < 4$. For $\rho < 3$, a correction factor $\alpha(\varepsilon)$ must be applied to account for the finite size of the solar disk, leading to an increase in $N_{F,r}$. For small elongations, $N_{F,r} << N_{F,d}$; at $\rho = 4$, Ingham's results give $N_{F,r} \sim 0.03\ N_{F,d}$. In a similar calculation, Calbert and Beard[41] used the parameters $p < 2.5$, $q = 1.5$, $a_1 = 0.18\ \mu$, and found that within a $4\text{-}R_\odot$ dust-free region, $N_{F,d}$ continues to increase, but with a smaller gradient than in the absence of such a region, while $N_{F,r}$ remains constant. Their value for a_1 followed from deductions from observational results, which indicated that $ka_1 = 2\pi a_1/\lambda \sim 2$, at $\lambda = 0.55\ \mu$.

Such calculations cannot be expected to predict the precise form of the F-corona. Fraunhofer diffraction theory[99,19,41] does not apply for ka small,[19] and $N_{F,d}$ and $N_{F,r}$ cannot then be separated. Mie scattering theory has been used, but applies only for spheres, whereas some observed interplanetary particles are found to have irregular shapes.[100] Further, uncertainty about the appropriate form of the particle distribution(s),[99,31] the magnitude of the associated parameters, and the assumption of an abrupt cut-off in the density of solid particles at the boundary of the dust-free region, together suggest approximate models only. Nevertheless, the relative decrease in $N_{F,d}$, as calculated, for $\varepsilon < \varepsilon'$, provides a possible interpretation of the relative depletion of N_c in the region $2 < \rho < 4.5$, compared with N_{K+F}. Figure 26 is a plot of $N_{c,e}/N_{K+F}$, and N_c/N_{K+F}; also plotted are calculated values given by,

$$N'_{cal} = \{N_F(1)\ N_{F,d}(3)\}/\{N_{K+F}(1)\ N_F(4)\} + N_K(1)/N_{K+F}(1),$$

where $N_{F,d}(3)$ values are derived from the results of Calbert and Beard,[41]

but for $\rho' = 4.5$; $N_F(4)$ are corresponding values for a model F-corona, where $N_F \propto \varepsilon^{-2.5}$.

According to the visible F-corona models proposed by Allen[18] and van de Hulst,[19] the major contribution to the observed radiance arises from particles relatively distant from the Sun; the effect of the greater irradiance and particle concentration in the solar vicinity is over-compensated by the effect of small-angle diffraction at large solar distances. This relationship depends on the magnitude of ka_1; a decrease in ka_1 results in a broadening of the diffraction profile, and the maximum contribution to the integrated column radiance therefore moves closer to the Sun. This suggests an explanation for the form of the ratio N_c/N_{K+F}: the radiance at $\lambda = 1\ \mu$ is more sensitive to particles close to the Sun than the radiance in the visible, and is therefore more affected by the dust-free region. Evidently the observations approximately fit $ka_1 \sim 2$, or $a_1 \sim 0.32\ \mu$. Ingham[99] has evaluated N_d for the case, $a_1 = 0.3\ \mu$, $p = 4$, $q = 1.5$, $\lambda = 0.63\ \mu$, $\rho' = 4$; at $\rho = 3$, the change in N_d due to a dust-free zone is ~ 3%, a result which is consistent with the above explanation. However, at smaller elongations, the fit is better for $a_1 = 0.4\ \mu$. In this case, the error is positive; that is, the calculated value is greater than that given by the observational model; for $a_1 = 0.3\ \mu$, the error is negative, indicative of the sensitivity of the calculation to this parameter. For $1.8 < \rho < 4$, the best fit is given by $a_1 \sim 0.34\ \mu$. The agreement between this result and that derived from the observations at $\lambda = 1\ \mu$ suggests that $a_1 \sim 0.3\ \mu$. But since the diffraction theory used omits the reflected and refracted contributions to the radiance, and since the models may not be realistic in, for example, the particle size

and density distributions, the above value cannot be asserted confidently.

In summary, the results indicate the presence of a dust-free zone, with $4 < \rho' < 4.5$, and a lower limit of interplanetary dust-particle radius, $a_1 \sim 0.3\ \mu$. The results also are not inconsistent with Peterson's thermal emission model[23] that indicates that for $\rho = 4$, and $\lambda = 1\ \mu$, $N_T \sim 0.3\ N_{K+F}$, where N_T is the thermal-emission component.

CHAPTER V

INTERFEROMETRIC TELESCOPE TEST

Introduction

Telescope tests. A variety of methods have been used to assess the optical precision of astronomical telescopes. Of these, the Foucault test is simple and sensitive, but does not readily yield quantitative data.[101,102] It has the advantage that a relatively long-exposure photographic record tends to average out seeing-induced perturbations in the wavefront. A variant, the Gaviola caustic test,[103] provides a precise method of measuring a paraboloid at its center-of-curvature. In the Hartmann test,[104,105] a perforated screen is placed over the primary objective aperture; the generalized pupil function can then be derived from measurements of the light distribution close to the image plane. The Ronchi screen[106] has also been applied as a telescope test; interpretation can be difficult due to diffraction effects.

An interferometric type of test has the attraction of providing direct quantitative data on the phase variations across the pupil, and hence on the accuracy and alignment of the optical surfaces, in units of the wavelength of the source radiation, with a potential precision $\lesssim 0.05\ \lambda$. This research is concerned with the description and analysis of a new interferometer--the "Point-Diffraction Interferometer,"[107,108] and its application as a telescope test.

Two-beam interference. For a general light source having a finite angular and spectral extent, the complex scalar optical disturbance, $V(\underset{\sim}{u}_i,t)$, at a field point $\underset{\sim}{u}_i$, varies randomly with time in amplitude and phase. The correlation of such statistical fluctuations between different field points is described by partial coherence theory, conventionally divided into spatial (lateral) coherence and temporal (longitudinal) coherence; strictly, these are not separable except for a restricted class of optical fields.[109] The theory leads to a detailed description of two-beam interference. In turn, properties of an interference field can give information about the source.

A two-beam interferometer forms two wavefronts originating at a common source. The concepts of lateral and temporal coherence are usually illustrated by a wavefront-division interferometric system. The more common system that operates by amplitude division is considered here. In general, the two wavefronts have a relative delay and lateral shift at a point of superposition, $\underset{\sim}{u}_i$, in the interference plane. The associated complex optical disturbances are $V_1(\underset{\sim}{u}_i,t)$, and $V_2(\underset{\sim}{u}_i,t+\tau)$, where τ is the relative delay over non-dispersive paths, and the instantaneous field is

$$V(\underset{\sim}{u}_i,t) = V_1(\underset{\sim}{u}_i,t) + V_2(\underset{\sim}{u}_i,t+\tau).$$

The observable quantity is the time-averaged intensity

$$I(\underset{\sim}{u}_i) = \langle V(\underset{\sim}{u}_i,t)\, V^*(\underset{\sim}{u}_i,t)\rangle, \text{ neglecting a factor of 2; then}$$

$$I(\underset{\sim}{u}_i) = I_1(\underset{\sim}{u}_i) + I_2(\underset{\sim}{u}_i) + 2\,\mathrm{Re}\{\Gamma_{12}(\underset{\sim}{u}_i,\tau)\},$$

where $\Gamma_{12}(\underset{\sim}{u}_i,\tau) = \langle V_1^*(\underset{\sim}{u}_i,t)\, V_2(\underset{\sim}{u}_i,t+\tau)\rangle$ is the mutual coherence function[65] of V_1 and V_2. Its normalized form is the complex degree of coherence, $\gamma_{12}(\underset{\sim}{u}_i,\tau) = \Gamma_{12}(\underset{\sim}{u}_i,\tau)/\sqrt{I_1 I_2}$, so that the general interference field is given by

$$I(\underset{\sim}{u}_i) = I_1(\underset{\sim}{u}_i) + I_2(\underset{\sim}{u}_i) + 2\sqrt{I_1 I_2}\ \mathrm{Re}\{\gamma_{12}(\underset{\sim}{u}_i,\tau)\}.$$

γ_{12} is in general a periodic function, and unlike the field, V, it can be determined from the interference pattern simply by intensity measurements. The modulus satisfies the relation, $0 \leq |\gamma_{12}| \leq 1$, where in the coherent limit, $|\gamma_{12}| = 1$, and in the incoherent limit, $|\gamma_{12}| = 0$. The visibility V, of the pattern is given by, $V(\underset{\sim}{u}_i) = (I_{max} - I_{min})/(I_{max} + I_{min})$, where I_{max} is the intensity of a fringe minimum, in the vicinity of $\underset{\sim}{u}_i$. For a quasi-monochromatic source and $I_1(\underset{\sim}{u}_i) = I_2(\underset{\sim}{u}_i)$, $V(\underset{\sim}{u}_i) = \gamma_{12}(\underset{\sim}{u}_i,\tau)$. It follows that V is determined by both the source and interferometer characteristics. The van Cittert-Zernike theorem[65] describes the lateral coherence at two field points of an extended, quasi-monochromatic source. In the usual case of a uniform, circular source of angular radius, α, the lateral coherence interval, ℓ, is expressed by the uncertainty relation, $\alpha\ell/\lambda \sim 1$, as can also be derived using a quantum-mechanical formalism.[110] The relative lateral shift of two interfering wavefronts is therefore limited by this restriction. Even for zero shift, conceptually the resolved source can be considered to be composed of angularly separated point sources each giving rise to an elementary wavefront. At a point in the interference plane, the phase difference

between each pair of wavefronts (as generated by the interferometer) varies, due to variations of path difference. Hence the interference term varies and the fringe modulation, or visibility, is diminished. If the interferometer source is effectively a point, the mutual coherence of interfering wavefronts having a relative delay τ at a point $\underset{\sim}{u}_i$ is equivalent to the autocorrelation or self-coherence, $\gamma_{11}(\underset{\sim}{u}_i,\tau)$, of the oscillations of one of the wavefronts at points separated longitudinally by the same delay. For a point source of bandwidth $\Delta\nu$, where ν is the frequency, the delay is limited by the uncertainty relation, $\Delta\tau\Delta\nu \sim 1$, or equivalently, $\Delta p\Delta\sigma \sim 1$, where Δp is the path difference or coherence length of the radiation, and $\Delta\sigma$ is the bandwidth in wavenumbers. A white-light point source can therefore be used only when $\tau \sim 0$. The restriction follows conceptually, since each spectral element gives rise to a wavelength-dependent phase difference between the interfering wavefronts. As discussed below, for the point-diffraction interferometer, $\tau \equiv 0$ for the axial path and a white-light source can be used; but it must be effectively a point, both from the mode of operation and since the wavefronts have an effective radial shear when circular fringes are introduced. All star sources satisfy this lateral coherence requirement, for all existing telescopes.

In summary, optimum fringe modulation or unit visibility requires that $|\gamma| = 1$ and $I_1 = I_2$; further, the two wavefronts (or components derived from them) must have the same polarization state. The latter two conditions can be achieved by interferometer design. With minor

qualifications, $|\gamma| \sim 1$ for a laser source under all practical circumstances. Then, in principle, maximum potential information can be obtained from the interferogram. But the high degree of coherence can lead to the occurrence of secondary, unwanted interference patterns and perturbations of the interference field arising from diffraction at optical-surface discontinuities. Such a noise background can result in an effective decrease in V. In this respect, design simplicity of an interferometer is an advantage.

Two-beam interferometers. Many two-beam interferometers suitable for testing optical systems have been described; there are only a few fundamentally different types, however, and in terms of the underlying principles, the range is even smaller, the number depending on the classification system used. In almost all cases, the light from a "point" source is divided into two beams, to produce a "test" and a "reference" beam. These two beams follow separate paths, or at least have different geometries, such that the test beam has impressed on it any phase variations caused by the system under test, while the reference beam is unmodified. The two beams, or "wavefronts," are then recombined to form an interference fringe pattern that reveals variations of phase difference across the pupil of the system under test in terms of variations of fringe location. When the two wavefronts match perfectly, the interference pattern is a uniform field. If the effective sources of the two wavefronts are slightly separated laterally, straight fringes are introduced across the field; and circular fringes for a longitudinal separation. In general then,

the form of the fringe pattern is determined both by the relative alignment of the two wavefronts, and the presence of any deformations in the test wavefront different from those in the reference wavefront.

The dividing process that generates a reference and a test beam is usually accomplished by means of a partially-reflecting plate. In the Michelson interferometer, one "beamsplitter" serves both to divide and to recombine the beams; in the Mach-Zehnder interferometer, two are usually used. Beamsplitters of different types, such as those that separate by means of polarization, scattering, and diffraction have also been used. Several interferometers have been described in which diffraction is used to generate at least one of the two beams. For example, the diffracted component may be derived from a linear diffraction grating, as used in one form of the Twyman-Green interferometer,[111] from a circular grating as used in the zone plate interferometer,[112,113] a random diffraction screen in a scatter-plate interferometer,[114] or a complex diffraction screen in a holographic interferometer.[115] It will be shown that the Point-Diffraction Interferometer (PDI) belongs to this family, since the reference beam is generated by diffraction. It also shares the characteristics of "common-path" interferometers[111] in which the test and reference beams have equal optical paths along a common axis. For this class of interferometer the effects of vibration and phase fluctuations in the air path are far less than for interferometers in which the beams follow separate paths, and a relatively stable

interference pattern is typical. Another classification scheme can be used; the PDI and some forms of lateral- and radial-shear interferometers are fundamentally different from all other two-beam interferometers since the light is divided into two components to produce a test and reference beam, *after* passing through the system under test. This allows the enormous freedom of testing components, or even entire optical system, *in situ*, without the need to fulfill some special interferometer configuration. The lateral shear interferometer is simple to align and use,[116] a distinct advantage for the non-laboratory conditions of a field telescope test, but the interference pattern does not give the wave-aberration directly, but its gradient (for small shears), and requires computer reduction for all but the simplest cases. The radial-shear interferometer can also be made in a compact and simple form,[113] but cannot be used to test a telescope in which the aperture has a central obscuration. In other interferometers, the source radiation is *first* divided into two components to form a test beam and a reference beam that separately interact with the system under test and are *then* recombined. Such a mode of operation precludes a telscope test application in the case of a remote source, with the possible exception of some complex and impractical configurations.

Point-Diffraction Interferometer

Principle. The PDI generates a spherical reference wave by diffraction at a point discontinuity placed in the path of a beam.

The discontinuity is a point-like circular aperture in an absorbing film on an otherwise non-diffracting substrate. (The complementary case of a point-like opaque disk can also be used.) Incident light is transmitted through the film with reduced amplitude, and, in addition, some light is diffracted by the aperture. In the general case, the amplitude of the diffracted wave will be much less than the directly transmitted wave unless the transmittance of the film is exceedingly small. However, if the aperture is placed in the vicinity of a point-like image formed by the system under test, two necessary conditions can be simultaneously satisfied: the amplitudes of the direct and the diffracted components can be equalized; also, the direct (or test) wavefront and the diffracted (or reference) wavefront have a common center of curvature, necessary to obtain a useful interference pattern.

The principle of operation is illustrated in Fig. 27. The aperture is critically positioned at the image of the wavefront to be analyzed. This wavefront emerges from the thin film unchanged except for reduced amplitude. Provided the aperture is sufficiently small in relation to the image size, a spherical diffracted wave is produced which interferes with the undiffracted wave. The resultant interference pattern directly reveals the wavefront aberration. For typical tests, an aperture of a few microns in a thin film having a transmittance ~ 0.01 is required. Apertures are prepared by shadowing with small spheres during evaporation of gold onto a specially cleaved mica substrate.

Theory. We consider the case of a monochromatic plane wave incident on an image-forming system. Points in the exit aperture have coordinates, (x,y), and in the image plane, (u,v). The complex disturbance at the exit aperture, of radius $R = \sqrt{x^2 + y^2}$, can be expressed by,

$$g(x,y) = g(x,y) \exp\left[-\frac{ik}{2f}(x^2 + y^2)\right]. \qquad (1)$$

For a unit amplitude wave, $g(x,y) = P(x,y)$, the generalized pupil function, where $P(x,y) = p(x,y) \exp\{-i\phi(x,y)\}$; $\phi(x,y)$ is the phase error at the point (x,y), and $p(x,y)$ is the pupil function, unity within the aperture, and zero otherwise. The exponential term of equation (1) is a quadratic phase approximation to a spherical wave converging to a focal point at a distance, f.

From the Fresnel approximation,[66] the complex disturbance in the image plane is,

$$G(u,v) = \exp\left[ik\{f + (u^2 + v^2)/2f\}\right]/i\lambda f \iint_{-\infty}^{\infty} g(x,y)\exp\{-\frac{ik}{f}(ux + vy)\}dxdy \qquad (2)$$

Apart from the quadratic phase factor, which for this discussion can be neglected, $G(u,v)$ is proportional to the two-dimensional Fourier transform of $g(x,y)$, the incident wavefront subtended by the system aperture.

In operation, the PDI diffraction aperture, of radius, a, is centered approximately in the image plane. The amplitude transmittance, $t(u,v)$, of the PDI plate is given by,

$$t(u,v) = t_1 + t_2 \operatorname{circ}\{\frac{r(u,v)}{\alpha}\},$$

where t_1 is the amplitude transmittance of the absorbing film over the plate aperture, t_2 is the effective amplitude transmittance of the diffracting aperture, and $\operatorname{circ}(\frac{r}{\alpha}) = \begin{cases} 1, & r \leq \alpha \\ 0, & r > \alpha, \end{cases}$

with r a radius coordinate, and $\alpha = 2aR/\lambda f$. The complex disturbance

emerging from the plate is then $G(u,v) = G(u,v)\ t(u,v)$, or

$$G(u,v) = t_1 G(u,v) + t_2 G(u,v)\ \mathrm{circ}(\tfrac{r}{\alpha}). \tag{3}$$

At infinity, the amplitude distribution is given by the transform of $G(u,v)$, aside from a multiplicative constant. Then,

$$g(x',y') = t_1 g(x',y') + t_2 T\{G(u,v)\ \mathrm{circ}(\tfrac{r}{\alpha})\}, \tag{4}$$

where $T\{\ \}$ is the Fourier transform operator. If the diffraction aperture in the plate is small compared with the central part of the image, $G(u,v)$ is then approximately constant over the region of the aperture, and the second transform reduces to the Fourier-Bessel transform,

$$B\{\mathrm{circ}(\tfrac{r}{\alpha})\} = 2\pi \int_0^{\alpha} r\ J_o(2\pi\rho r)\ dr,$$

where J_o is a zero-order Bessel function, and $\rho = r'/\lambda Z$, with r' a radius coordinate in a plane of observation at a distance Z. Substituting $\xi = 2\pi r\rho$,

$$\begin{aligned} B\{\mathrm{circ}(\tfrac{r}{\alpha})\} &= \frac{1}{2\pi\rho^2} \int_0^{2\pi\rho\alpha} \xi\ J_o(\xi)\ d\xi \\ &= \pi\alpha^2 \left[\frac{2J_1(2\pi\rho\alpha)}{2\pi\rho\alpha}\right] \\ &\approx \pi\alpha^2 \end{aligned} \tag{5}$$

when $2\pi\rho\alpha \sim 0$.

From equation (4), it then follows that for a centered, aberration-free system, the amplitudes of the diffracted and direct wavefronts are equal when $|t_1| = |\pi\alpha^2 t_2|$, or $a \sim 0.1\lambda f/R$. For the general case where aberration is present and the diffraction aperture is not centered exactly at the image, a slightly larger value for a is more suitable.

Characteristics. If the aperture is moved along the axis away from the focal plane, circular fringes occur, since the direct and diffracted wavefronts now have longitudinally-displaced centers-of-curvature.

Straight fringes are introduced when the aperture is moved laterally. This behavior is identical to that of other common-path interferometers. That *straight* fringes result from a lateral displacement can be seen from the following argument: the intersection of two spheres is a circle with center on the line defined by the centers of the spheres; therefore, the projection of the intersections on any plane parallel to a plane containing the sphere centers is a straight line. When the aperture is displaced with respect to the image, the amplitude of the diffracted wavefront varies according to the amplitude distribution in the image, while that of the test wavefront remains substantially constant. The fringe visibility, V, therefore, is a function of the interferometer setting and becomes low for relatively large displacements of the aperture. Nevertheless, this characteristic is not unduly restrictive since in most cases the variation is small or moderate within the usual range of settings desired for optimum display. V is also a function of the interferometer parameters--the aperture size and the relative film and aperture transmittances. In practice, fringes with close to unit visibility are easily obtained. As shown above, for typical tests the diameter of the aperture should be smaller than the central diffraction disk of the image; it must also fulfill the condition that the cone angle, defined by the first minimum in the diffraction pattern, should be greater than that of the system under test. This is equivalent to $a < 0.6\ \lambda(\sin\theta)^{-1}$, where a is the diffraction-aperture radius, and sin θ is the system numerical aperture. Both requirements can be simultaneously satisfied with one aperture for a large range of typical tests.

A laser is an ideal source to use with the PDI; the only optical surfaces that can give rise to secondary interference patterns, a common problem in most interferometers, are those of the system under test itself, and the recording system. The PDI plate can be tilted slightly so that light reflected from it is directed to the side of the test pupil. However, even if the plate is normal to the axis, it is unlikely that this stray light will prove to be a problem. The reflected beam is of special interest however, since it is perturbed identically, within a phase factor, to that of the transmitted light--the aperture gives rise to a spherical diffraction wavefront in both transmission and reflection. The reflected beam therefore has an identical interference pattern to that of the transmitted light, but with reduced visibility. Note that the irradiance in the central part of the image produced by a high-quality, small f/number optical system can be $\sim 10^6$ that of the direct, unexpanded laser beam. The PDI plate must therefore have negligible scattering properties over the general region containing the aperture. While a non-laser source can be used, less light is then available; the angular source size, α, must be restricted to satisfy lateral coherence requirements across the aperture, D, of the system under test, such that $\alpha \lesssim 2\lambda/\pi D$, where the value of the Bessel function argument has been taken as unity. Equivalently, the angular diameter of the source should be smaller than that which can be resolved by the system under test.

Interferometers in which the two beams follow separate paths are very sensitive to vibration and thermal fluctuations in the air path, since optical path variations so introduced appear as corresponding fringe displacements having the same scale as the test itself; that is, consecutive

fringes occur for optical path increments of one wavelength. For the PDI, relative displacements between the source, the system under test, and the interferometer plate also result in fringe movement, but the sensitivity is typically at least two orders of magnitude less than that for non-common-path interferometers. Fluctuations in the air path are normally evident only where the path is at least several meters, and then only when substantial temperature differences are present.

Telescope Testing

As pointed out above, the PDI can be used with a polychromatic source, and only requires access to a point-like image for its operation. These properties suggested its application to that of testing astronomical telescopes using a stellar source. While many stars are binary systems, almost without exception, for the brightest stars one of the two components is much fainter than the other and can be ignored. At any time there is generally a second, first, or (preferably) zero magnitude star near the zenith, where atmospheric seeing is normally the best, and this circumstance provides the logical choice for the star source; otherwise it is arbitrary. Since even the lowest magnitude stars are relatively weak interferometer sources, illuminance in the recording plane is an important consideration; the relevant aperture is that of the telescope primary objective. For a given effective focal length, the illuminance is independent of the aperture, while for a given f/number, there is a gain approximately proportional to the square of the aperture.

The test has been tried on the Hale Observatories' 152-cm Cassegrain telescope at Mt. Palomar.[108] The interferometer was attached at the

Cassegrain focus. For alignment, it was found more convenient to use the fine setting controls of the telescope than the micrometer adjustments of the interferometer. During excellent atmospheric-seeing conditions, it was simple to find an interference pattern. The fringes were well-defined across the entire field but continuously in motion due to atmospheric-seeing-induced phase fluctuations and image movement. The precision of the telescope drive was such that fringes remained evident over a period of many minutes, without need for further adjustment. A 35-mm camera, focused to the telescope pupil, was used to record the interference pattern on an extreme high-speed film. However, even during the best seeing conditions encountered, using a zero magnitude star such as Capella, the fringe movement, though readily followed by eye, was too rapid to record unblurred at a minimum exposure time of 1 s. Hence no photographic records show well-defined interference patterns. Figure 28a-i contains selected interferograms recorded sequentially over an interval of approximately ten minutes, when, under exceptionally stable atmospheric conditions, the mean wavefront error due to atmospheric perturbations remained less than one wavelength across the telescope aperture. While these transient features are evident in the interferograms, common features can also be identified, persisting from exposure to exposure. Such features therefore characterize the telescope optical system. Poor seeing was characterized by a fine mottled appearance of the image, or, during strong wind conditions, a unidirectional streaming pattern. Under both conditions, no continuous fringes were evident, but the white-light interference highlighted the complex structure of the wavefront. While this particular telescope optical system is evidently of high optical quality, in the

absence of any image intensification device, it was not possible to obtain a precise quantitative measure of its accuracy. Operationally, the test proved to be a simple, straightforward procedure.

This study emphasized that an accurate error analysis requires excellent atmospheric seeing conditions, if only for a period of a few seconds; or, alternatively, a system to record many samples of the interference pattern, compute the wavefront of each sample, and then average out the randomly varying component due to the seeing. But this component should be, at most, of only a few wavelengths amplitude. Otherwise, the interference pattern, if identifiable at all, is likely to be too scrambled to allow reduction. The experiment also pointed to the desirability of a more sensitive recording system than purely photographic. A high-sensitivity vidicon and recording system appears to be ideal for this application. It is noted that such a test provides an excellent method to obtain a quantitative measure of atmospheric seeing, particularly in its ability to discriminate over a range of good to exceptional seeing conditions.

The test has been applied also to the 61-cm f/11 Cassegrain telescope of the Williston Observatory, Mt. Holyoke College. Using the zero magnitude star Arcturus as a source, the interference pattern was clearly evident when viewed directly by eye. Even though during the period of observation of a few hours the pattern was continually in rapid motion, a marked localized asymmetry in the fringe distribution was obvious, due to mirror misalignment. (Subsequent independent work revealed that the primary mirror was de-centered in its mount.) An attempt was made to record such patterns using the system shown in Fig. 29. The image

intensifier used had a gain in excess of 100, and a resolution of 64 lp/mm, more than adequate for this application. The long decay time of the image on the output screen of the intensifier precluded visual observation of the fringes of the screen. However, recording of a useful pattern by this method proved unsatisfactory due to a problem with the telescope drive. It was decided therefore to attempt to test the telescope with a remote laser source, since unlike many larger systems, the telescope could be tilted to an unobstructed horizontal view. It must be remembered that measurements in this configuration may not necessarily give the same result as those made when the telescope is within its normal operating rotational range. Advantages over a star source are: 1) a much larger irradiance in the recording plane; 2) a stationary system; and 3) improved atmospheric seeing.

A 2-mW He-Ne laser was set up at a distance of 2.3 km (the wavefront error due to testing at this non-infinite conjugate is ~ 0.04λ, and can therefore be disregarded). The gaussian spread of the raw beam at the telescope was mainly concentrated in an area of about 1 m diameter, representing an efficient use of the laser output. Alignment of the laser on the telescope was simply achieved by using a 5-cm corner-cube retro-reflector at the telescope entrance aperture. The reflected beam was clearly evident directly by eye, viewing close to the laser, and could be optimized by laser adjustment while viewing through a sighting telescope attached to the laser. The path was within a few meters of the ground over a distance of about 0.3 km, limiting the seeing quality. The best conditions were found to be under an extremely overcast sky, or, when clear, just after dawn under windless conditions, when thermal

equilibrium tends to occur. Most of the large number of interferograms recorded reveal at least some irregularities due to path turbulence, even though at some instants the wavefront appeared to be entirely stationary. All show the pronounced asymmetry of the wavefront observed visually with a star source. Several are almost identical and are therefore considered to characterize the error of the telescope optical system. Representative interferograms are shown in Fig. 30a-f. The approximate wavefront error (the departure from an osculating spherical surface) has been evaluated at several points for each of these, and the errors averaged. For example, the abrupt change in fringe direction identifies a segmental region of the pupil where the error is ~ 1.6 λ at the pupil boundary (with respect to the region contiguous to the segment.) Where the entire interference pattern, or portion of it, was stationary during the instant of exposure, the fringes show high spatial resolution, estimated to be < 0.01 of the telescope aperture. Exposures of 1 millisecond on Tri-X film were, if anything, overexposed. In fact the interference pattern could be conveniently observed as a projection on the internal surface of the observatory dome.

The test has been applied also to two compact catadioptric astronomical telescopes, both of commercial manufacture. These tests were carried out indoors, using a laser source at a distance of about 30 m from the telescope. Figure 31a and b comprises interferograms of one of these telescopes, a 20-cm Schmidt-Cassegrain design, on-axis. Figure 32a and b shows interferograms of a 9-cm Maksutov-Cassegrain telescope. The high optical quality is evident, with an error on-axis no greater than 0.1 λ. These indoor results illustrate the typical quality of interferograms obtainable

with the PDI under laboratory conditions, and the potential quality of interferograms from larger systems under excellent field conditions.

From both field and laboratory results, it is concluded that the point-diffraction interferometer is a very useful addition to the range of standard telescope tests.

TABLE 1

Detector #	Type	Spectral Range (μ)	Wavelength of Max. Responsivity (μ)	Scan Range* ($R/R_{\odot}$)	Vignetting Range** ($R/R_{\odot}$)
1	PbS	2.0 - 2.5	2.25	3.37 - 12.93	3.37 - 5.10
2	InAs	2.3 - 3.4	3.10	3.22 - 12.78	3.22 - 5.41
3	PbS	2.0 - 3.0	2.50	3.03 - 12.59	3.03 - 5.40
4	PbS	1.9 - 2.5	2.22	3.00 - 12.56	3.00 - 5.42
5	PbS	3.0 - 4.0	3.30	3.22 - 12.78	3.22 - 5.38
6	PbS	2.0 - 3.0	2.50	3.37 - 12.93	3.37 - 5.10

*Zero-error alignment and tracking.

**October 1973 balloon flight.

TABLE 2a-c

Normalized values of the scattered radiance, N, of coronagraph mirrors #3, #4, #5, #7, and #8, measured as a function of the scattering angle, θ_s.

Mirror #3

θ_s	N/N_o	
	b	*c*
0.28°	2.34×10^{-6}	1.26×10^{-6}
0.42	1.33	7.87×10^{-7}
0.70	7.23×10^{-7}	4.72
1.11	3.61	3.15
1.81	1.45	1.89
3.21	6.5×10^{-8}	7.87×10^{-8}
4.18	4.1	4.7
5.02		3.6
7.54		
10.1		

(a)

Mirror #7

θ_s	N/N_o	
	a	*b*
0.28°	1.08×10^{-5}	
0.42	6.25×10^{-6}	1.49×10^{-5}
0.70	2.17	7.23×10^{-6}
1.11	1.16	2.89
1.81	5.80×10^{-7}	1.06
3.21	2.17	3.37×10^{-7}
4.18	1.30	2.05
5.02	9.63×10^{-8}	7.2×10^{-8}
7.54	4.8	
10.1	2.4	

(b)

Mirror #8

θ_s	N/N_o				
	a	*a*	*d*	*b*	*c*
0.28°	7.71×10^{-6}	7.83×10^{-6}	1.61×10^{-5}	9.40×10^{-6}	1.29×10^{-5}
0.42	4.82	5.30	9.88×10^{-6}	5.30	8.03×10^{-6}
0.70	2.17	2.41	4.58	2.41	3.58
1.11	1.06	1.20	2.02	1.20	1.79
1.81	4.82×10^{-7}	4.58×10^{-7}	8.67×10^{-7}	5.06×10^{-7}	7.32×10^{-7}
3.21	1.83	1.69	3.13	2.17	2.73
4.18	9.63×10^{-8}	1.01	1.93	1.45	1.64
5.02	7.7	7.2×10^{-8}	1.45	9.63×10^{-8}	1.25
7.54	4.1	4.8	7.2×10^{-8}	4.8	
10.1	2.4		6.0		

(c)

TABLE 2d-e

Mirror #4

θ_s	N/N_o			
	a	*d*	*b*	*c*
0.28°	8.07×10^{-6}	9.16×10^{-6}	8.19×10^{-6}	1.43×10^{-5}
0.42	4.34	5.18	5.30	8.35×10^{-6}
0.70	2.22	2.77	2.89	3.69
1.11	1.20	1.33	1.49	1.97
1.81	5.54×10^{-7}	5.54×10^{-7}	7.47×10^{-7}	9.0×10^{-7}
3.21	2.17	2.17	2.89	3.28
4.18	1.33	1.37	1.81	2.29
5.02	1.06	9.63×10^{-8}	1.33	1.47
7.54	6.0×10^{-8}	4.8	7.2×10^{-8}	
10.1	3.6	3.6	4.8	

(d)

Mirror #5

θ_s	N/N_o			
	a	*d**	*b*	*c*
0.28°	1.44×10^{-5}	4.10×10^{-5}	1.54×10^{-5}	2.15×10^{-5}
0.42	7.25×10^{-6}	2.77	1.01	1.16
0.70	3.5	1.69	4.46×10^{-6}	5.08×10^{-6}
1.11	1.69	8.67×10^{-6}	2.17	2.42
1.81	6.75×10^{-7}	3.98	8.92×10^{-7}	9.22×10^{-7}
3.21	2.17	1.45	3.31	3.13
4.18	1.33		1.98	1.88
5.02	8.4×10^{-8}		1.33	1.41
7.54	3.6		6.0×10^{-8}	
10.1	2.4		4.3	

(e)

Gold-film deposition, and N/N_o measurements: *a*, February 1971; *b*, October 1971; *c*, October 1973. N/N_o measurements: *d*, September 1971.

*Mirror exposed to room air over a two-week period prior to these measurements.

TABLE 3

Detector #	Responsivity, R	D* (500 K, 400)
1	5.0×10^{6} VW^{-1}	$\sim 2 \times 10^{11}$ cm $(Hz)^{\frac{1}{2}}$ W^{-1}
2	1.0×10^{4}	$\sim 6 \times 10^{10}$
3	5.7×10^{6}	$\sim 2 \times 10^{11}$
4	5.2×10^{6}	$\sim 2 \times 10^{11}$
5	5.6×10^{6}	$\sim 2 \times 10^{11}$
6	5.7×10^{6}	$\sim 2 \times 10^{11}$

TABLE 4

Parameters of balloon flights of October 24, 1971 (644-P) and October 29, 1973 (795-P)

	644-P	795-P
Launch Time	05:56 CST	07:02 CST
Average Ascent Rate	2.3 m/s	4 m/s
Float Altitude	38 km	29.4 km
Float Altitude Attained At:	11:16 CST	9:00 CST
Data Recording Commenced	9:38 CST	10:00 CST
Duration of Data Recording	∿ 5 hr.	∿ 3 hr. 45 min.
Termination	14:50 CST	13:45 CST
Duration of Flight	8 hr. 54 min.	6 hr. 45 min.
Flight Distance	∿ 800 km*	470 km

*Balloon ground coordinates remained approximately constant from 08:20 CST (15 km) to 10:00 CST (30 km).

TABLE 5

Detector #	Spectral Range	Number of Usable Scans 1971 Flight	1973 Flight
1	2.0 - 2.5 μ	78	
2	2.3 - 3.4	74	
3	2.0 - 3.0	54	
4	1.9 - 2.5	78	58
5	3.0 - 4.0	78	
6	2.0 - 3.0	54	56

TABLE 6

Ratios of corresponding ordinates, Y_i, of D_w coronal scans #4 and #14.

$R/R_\odot$	$Y_i(\#14)/Y_i(\#4)$
3.5	1.234
3.75	1.233
4.0	1.235
4.25	1.252
4.5	1.255
4.75	1.233
5.0	1.238
5.25	1.230
5.5	1.229
5.75	1.250
6.0	1.254
6.25	1.254
6.5	1.269
6.75	1.274
7.0	1.277
7.25	1.291
7.5	1.286
7.75	1.294
8.0	1.302
8.5	1.374
9.0	1.397

TABLE 7

Observed coronal radiances, $N_{c,e}$, $N_{c,w}$, and published values of white-light equatorial coronal radiances, $N_F(1)$, $N_{K+F}(1)$, $N_F(2)$, $N_{K+F}(2)$, for a minimum-corona model; units of 10^{-9} $N_\odot$.

$R/R_\odot$	$N_{c,e}$	$N_{c,w}$	N_c*	$N_F(1)$	$N_{K+F}(1)$	$N_F(2)$	$N_{K+F}(2)$
1.7	68.2			17.3	66.0		
1.8	45.0			13.6	47.1	13.8	44.7
1.9	32.1			11.6	34.9		33.6
2.0	24.5			9.55	27.7	10.0	25.1
2.2	15.4			7.24	17.3		16.2
2.5	8.35			5.07	9.53	5.37	8.91
3.0	4.00	3.31	3.65	3.16	4.73	3.24	4.57
3.5	2.44	2.16	2.30	2.14	2.81	2.19	2.82
4.0	1.64	1.45	1.54	1.51	2.00	1.58	1.91
4.5	1.39	1.27	1.33		1.46		1.39
5.0	1.09	1.02	1.05	0.851	1.10	0.891	1.05
5.5	0.832	0.798	0.815		0.862		0.82
6.0	0.666	0.642	0.654	0.562	0.678	0.562	0.646
6.5	0.554	0.545	0.550		0.534		0.531
7.0	0.447	0.445	0.446	0.400	0.420		0.440
7.5	0.357	0.363	0.360		0.360		0.369
8.0	0.331	0.330	0.331	0.288	0.301	0.302	0.316
8.5		0.268					
9.0		0.200			0.217	0.170	0.182

*$N_c = (N_{c,e} + N_{c,w})/2$

TABLE 8

Ratios of observed coronal radiances, $N_{c,e}$, $N_{c,w}$, N_c to published values of white-light equatorial coronal radiances, N_{K+F}.

$R/R_\odot$	$N_{c,e}/N_{K+F}$*	$N_{c,w}/N_{K+F}$	N_c/N_{K+F}
1.7	1.07		
1.8	0.98		
1.9	0.94		
2.0	0.93		
2.2	0.92		
2.5	0.91		
3.0	0.86	0.71	0.79
3.5	0.87	0.77	0.82
4.0	0.84	0.74	0.79
4.5	0.98	0.93	0.96
5.0	1.01	0.95	0.98
5.5	0.99	0.97	0.98
6.0	1.01	0.97	0.99
6.5	1.04	1.03	1.04
7.0	1.04	1.03	1.04
7.5	0.98	0.99.	0.98
8.0	1.07	1.07	1.07
9.0		1.00	

*$N_{K+F} = \{N_{K+F}(1) + N_{K+F}(2)\}/2$

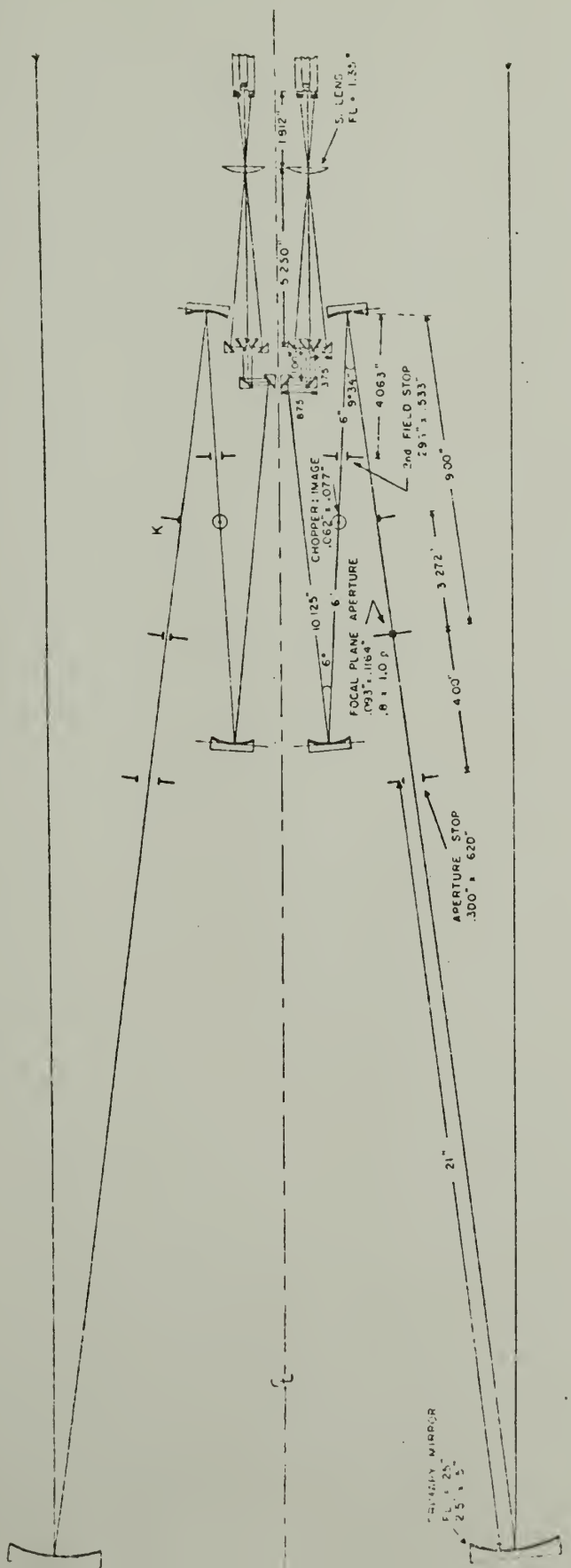

Fig. 1.--Coronagraph optical configuration. K indicates the internal knife-edged baffle.

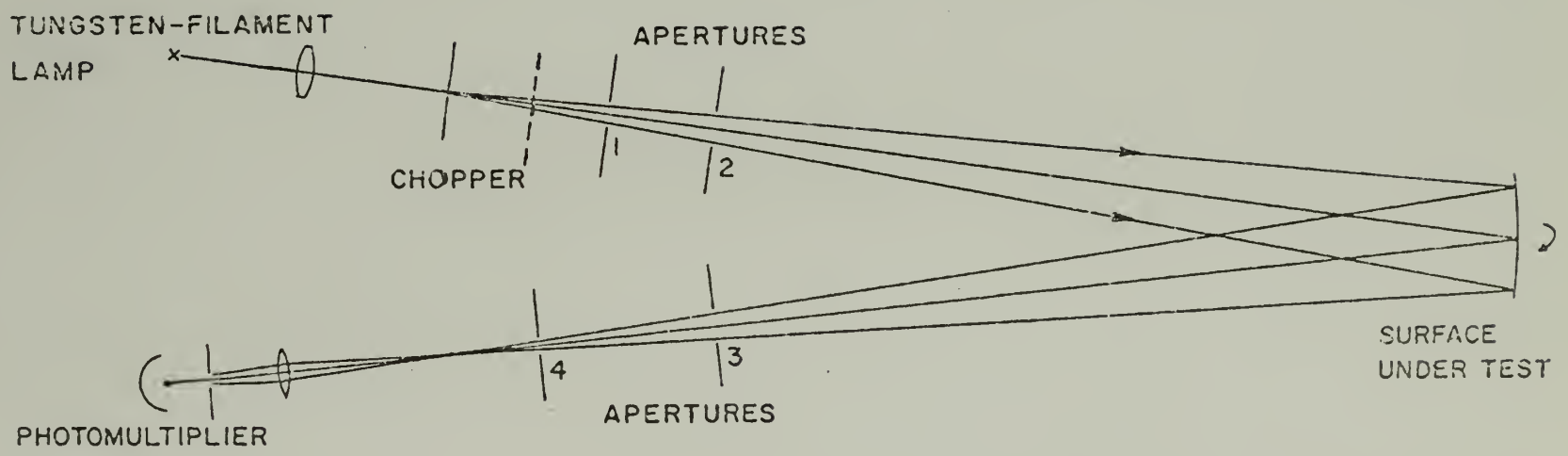

Fig. 2.--Optical configuration for measuring the coronagraph primary mirror scattering functions.

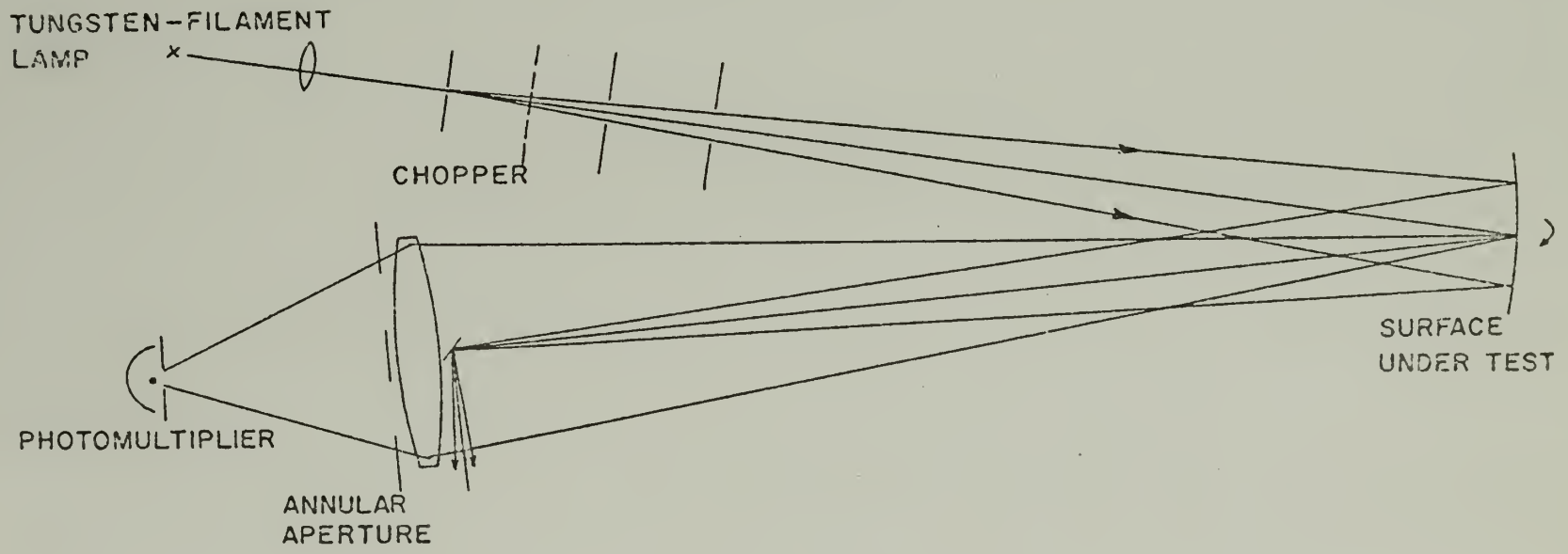

Fig. 3.--Optical configuration for measuring the integrated scattered radiance of the primary mirrors.

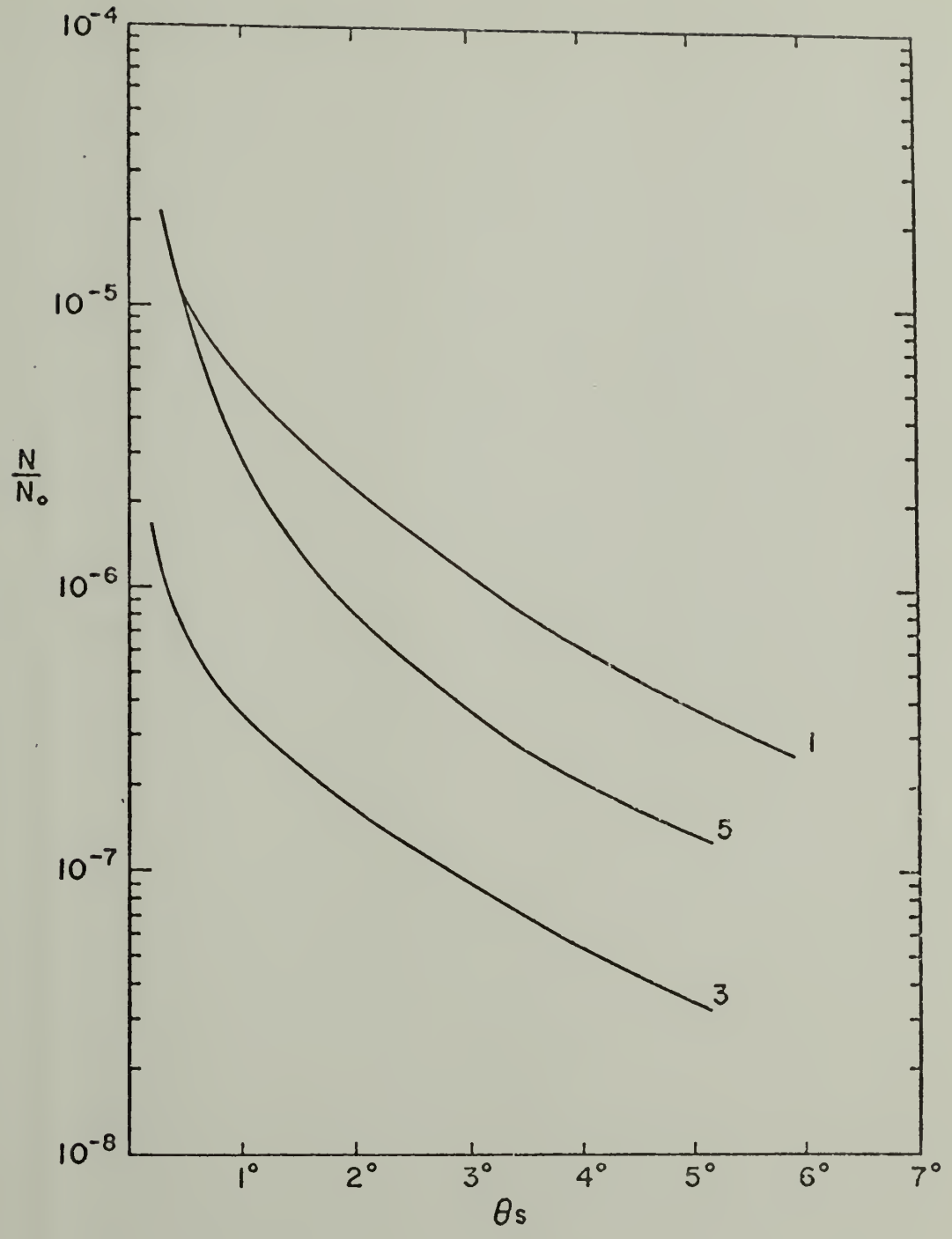

Fig. 4.--The measured angular dependence of scattering of coronagraph primary mirrors #1, #5, and #3, as a function of the angle of scatter, θ_s.

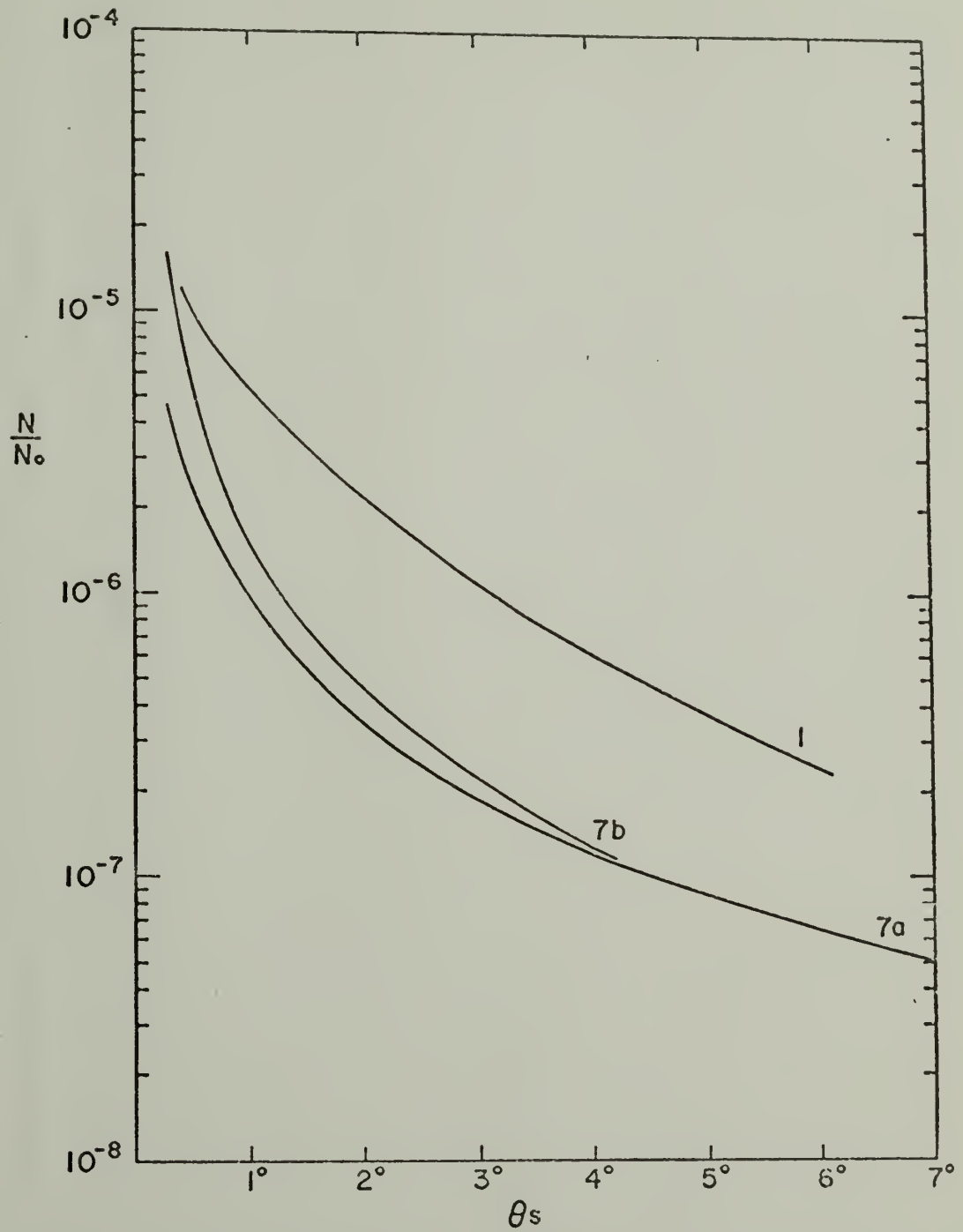

Fig. 5.--The measured angular dependence of scattering of coronagraph primary mirrors #1 and #7 as a function of the angle of scatter, θ_s. The curves labelled 7a and 7b correspond to measurements of mirror #7 before and after the balloon flight of 1971.

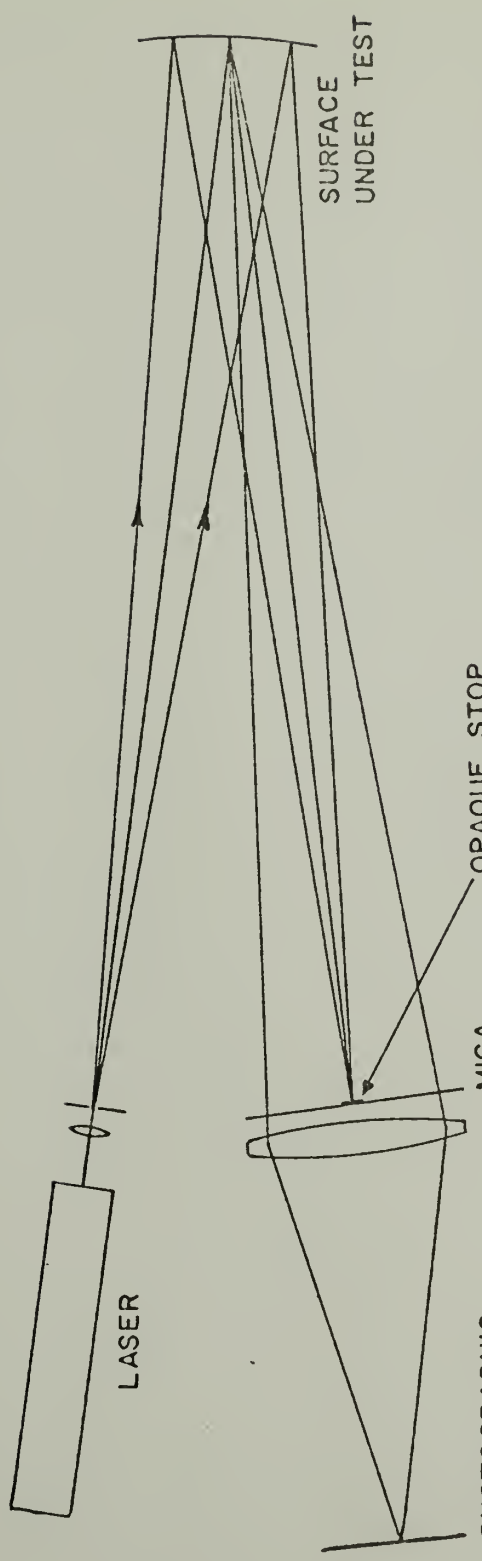

Fig. 6.--Optical system to produce central dark-ground illumination.

(a)

(b)

(c)

(d)

Fig. 7a-d.--Photographic records of the central region of a primary mirror surface using dark-ground illumination, for scattering angles, θ_s, of a, 0°; b, 1°; c, 2°; and d, 4°.

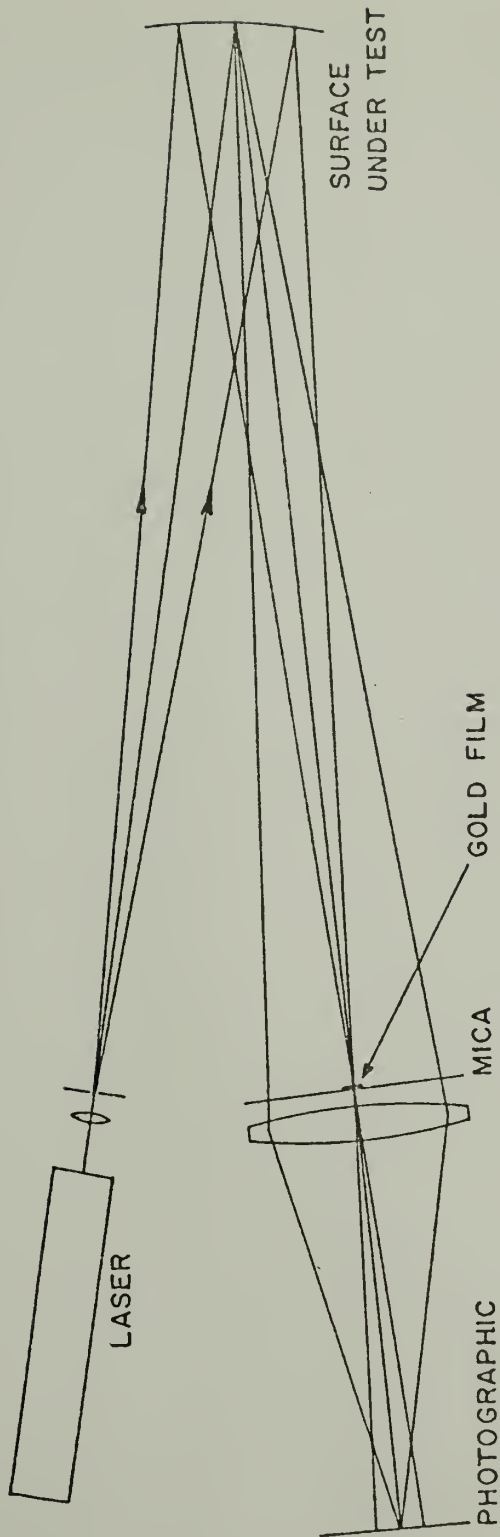

Fig. 8.--Phase-Contrast Test.
The phase disk is a partially transparent evaporated gold film on a mica substrate.

(a)

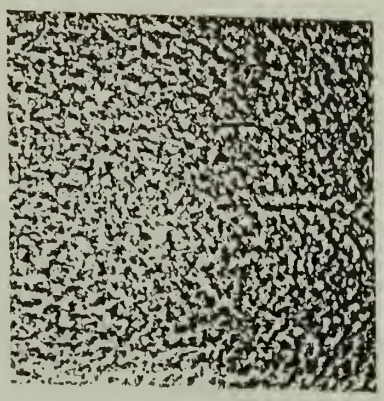

(b)

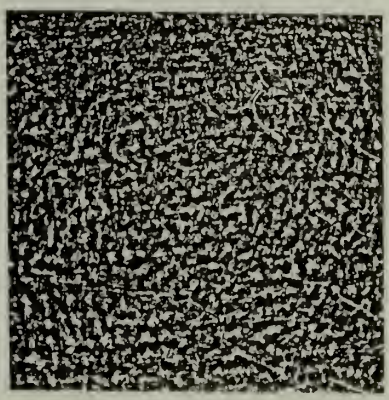

(c)

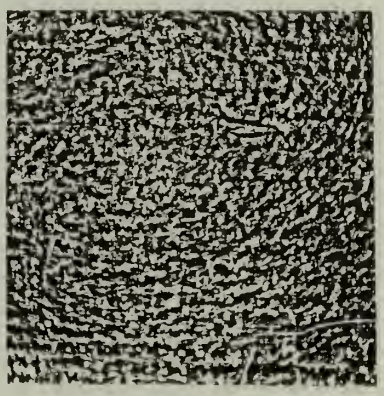

(d)

(e)

Fig. 9a-e.--Phase contrast images of the central region (9 cm^2) of the gold-coated surfaces of primary mirrors: a, #1; b, #5; c, #4; d, #8; and e, #3.

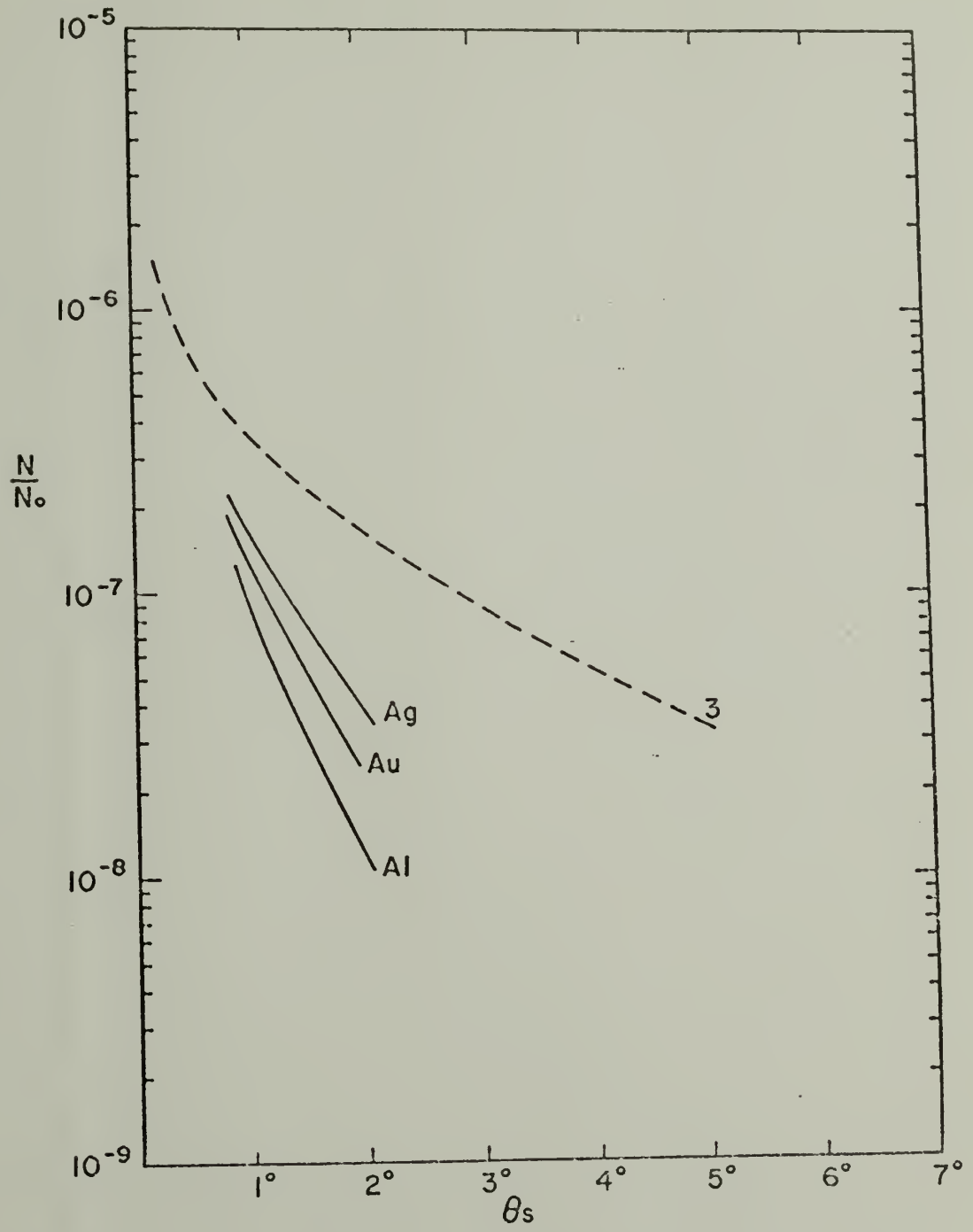

Fig. 10.--The measured angular dependence of scattering of specially-cleaved mica sheets coated with evaporated films of silver, gold, and aluminum, compared with that of primary mirror #3.

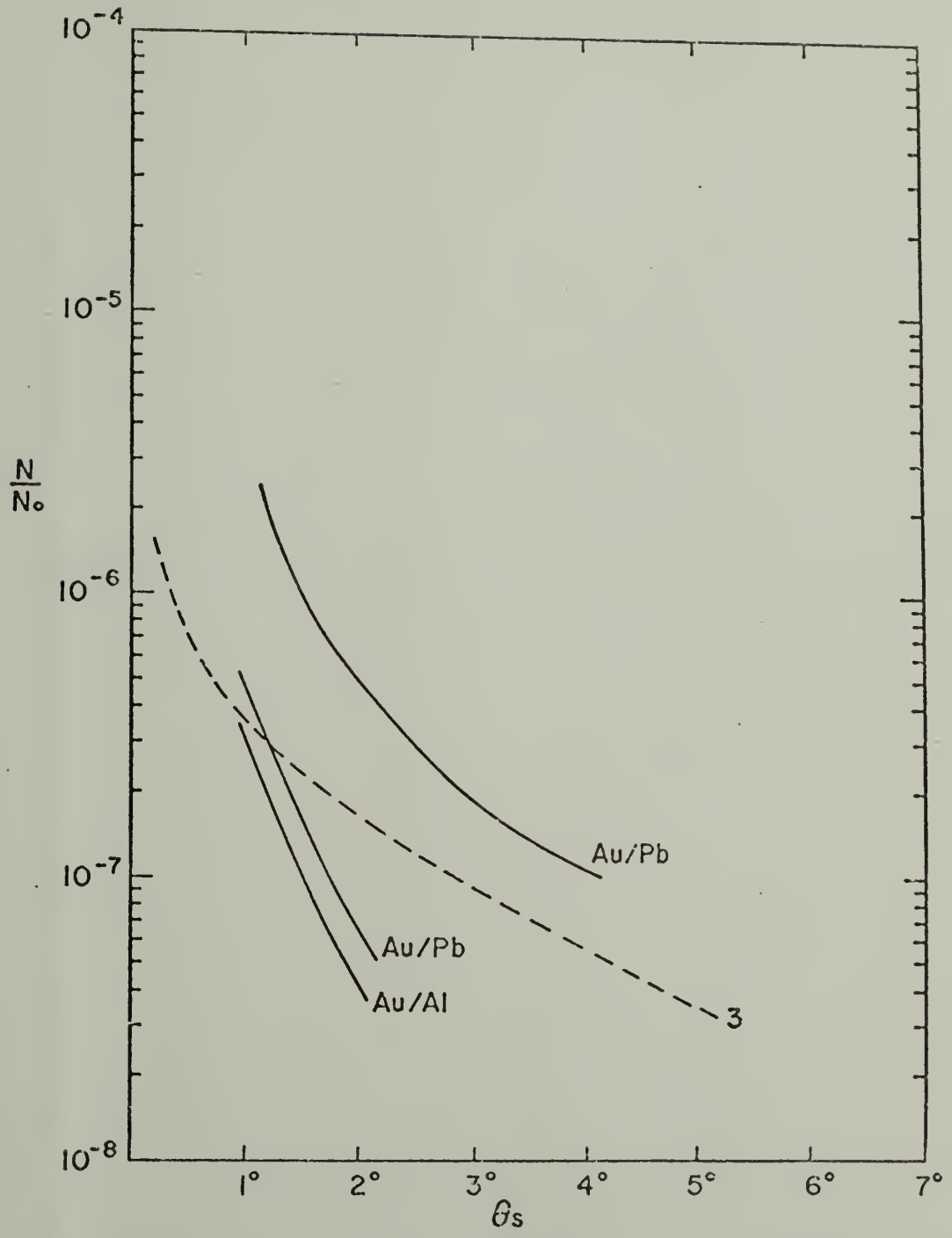

Fig. 11.--The measured angular dependence of scattering of specially-cleaved mica sheets coated with evaporated films of lead and aluminum, over-coated with gold. The two gold-lead curves correspond to measurements made on different parts of the same substrate. The broken curve represents the scattering function of primary mirror #3.

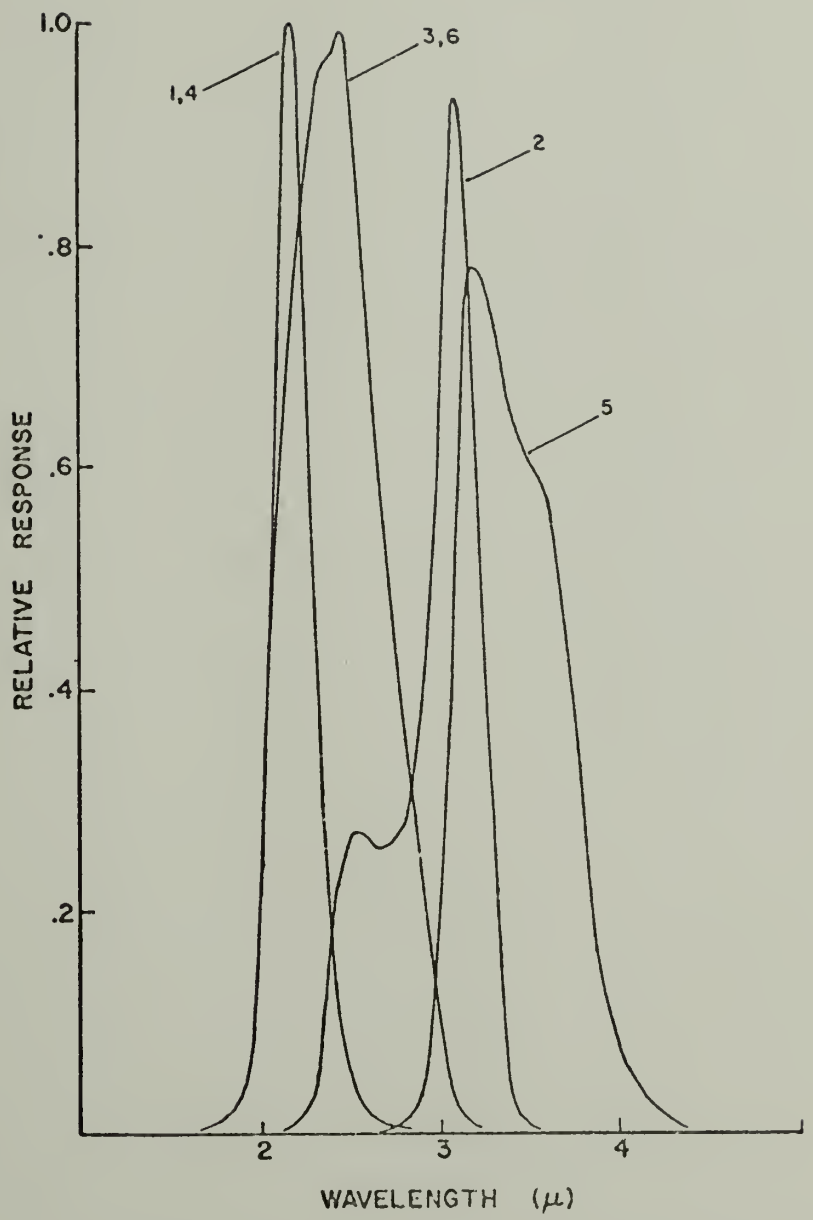

Fig. 12.--Spectral responses of the six coronagraph detectors.

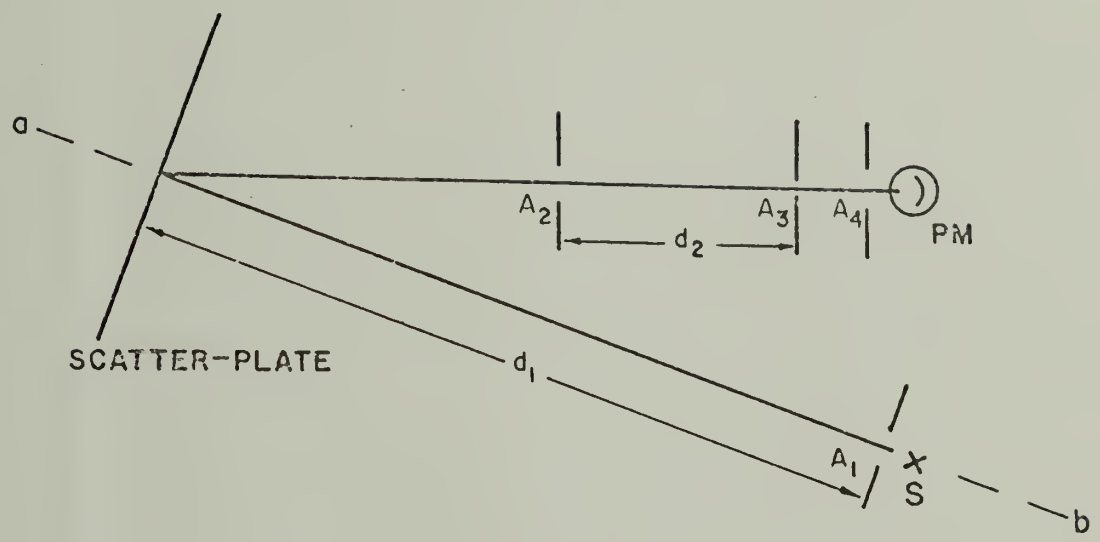

Fig. 13.--Optical system used to determine the effective reflectance of a gold-coated scatter plate, using a photomultiplier, PM, and a diffuse source, S.

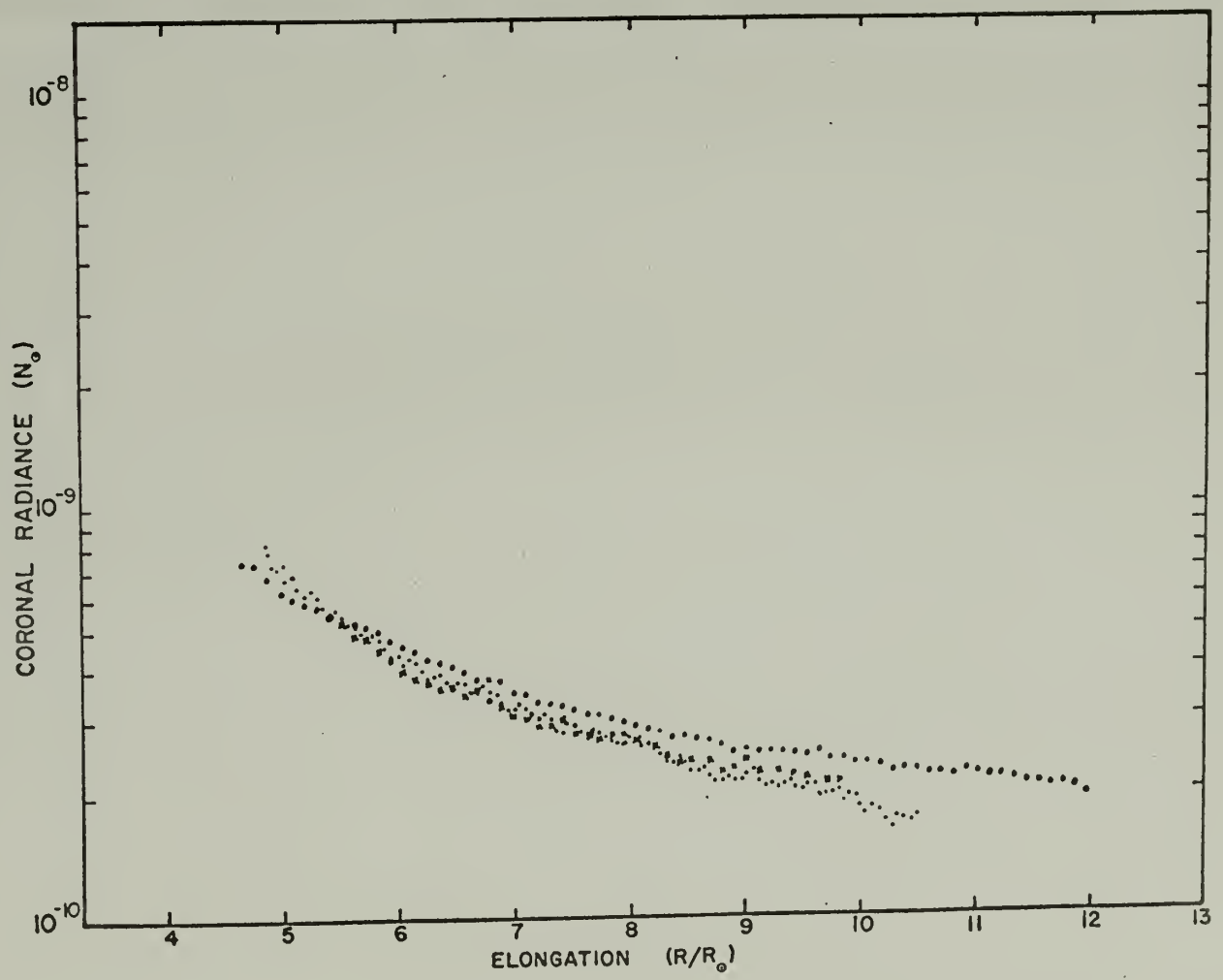

Fig. 14.--Coronal radiance as a function of elongation, $R/R_\odot$, observed during the balloon flight of October 24, 1971. The plotted points are averaged values for detectors #1 (×), #2 (∘), and #3 (•).

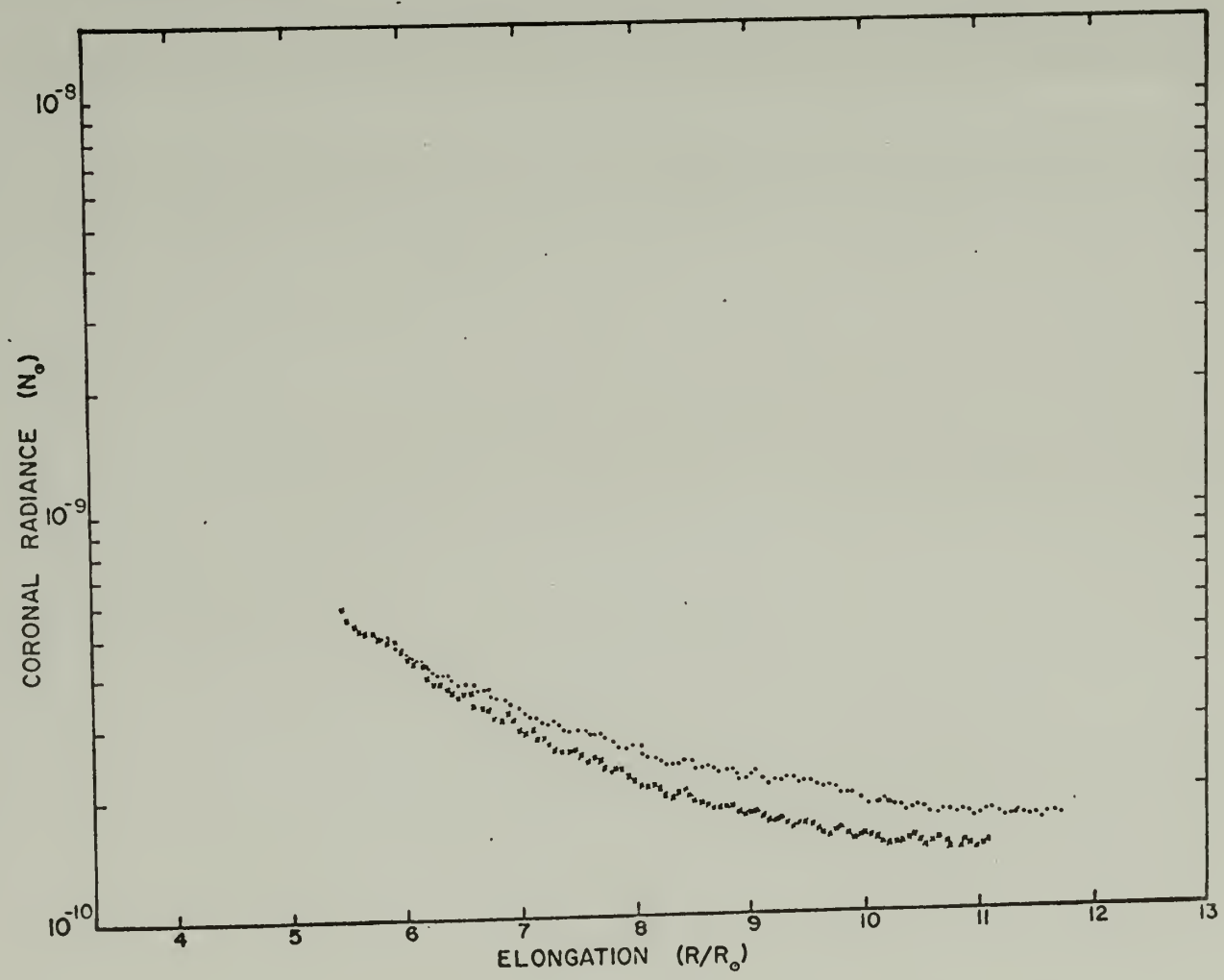

Fig. 15.--Coronal radiance as a function of elongation, $R/R_\odot$, observed during the balloon flight of October 24, 1971. The plotted points are averaged values for detectors #4 (×), and #6 (•).

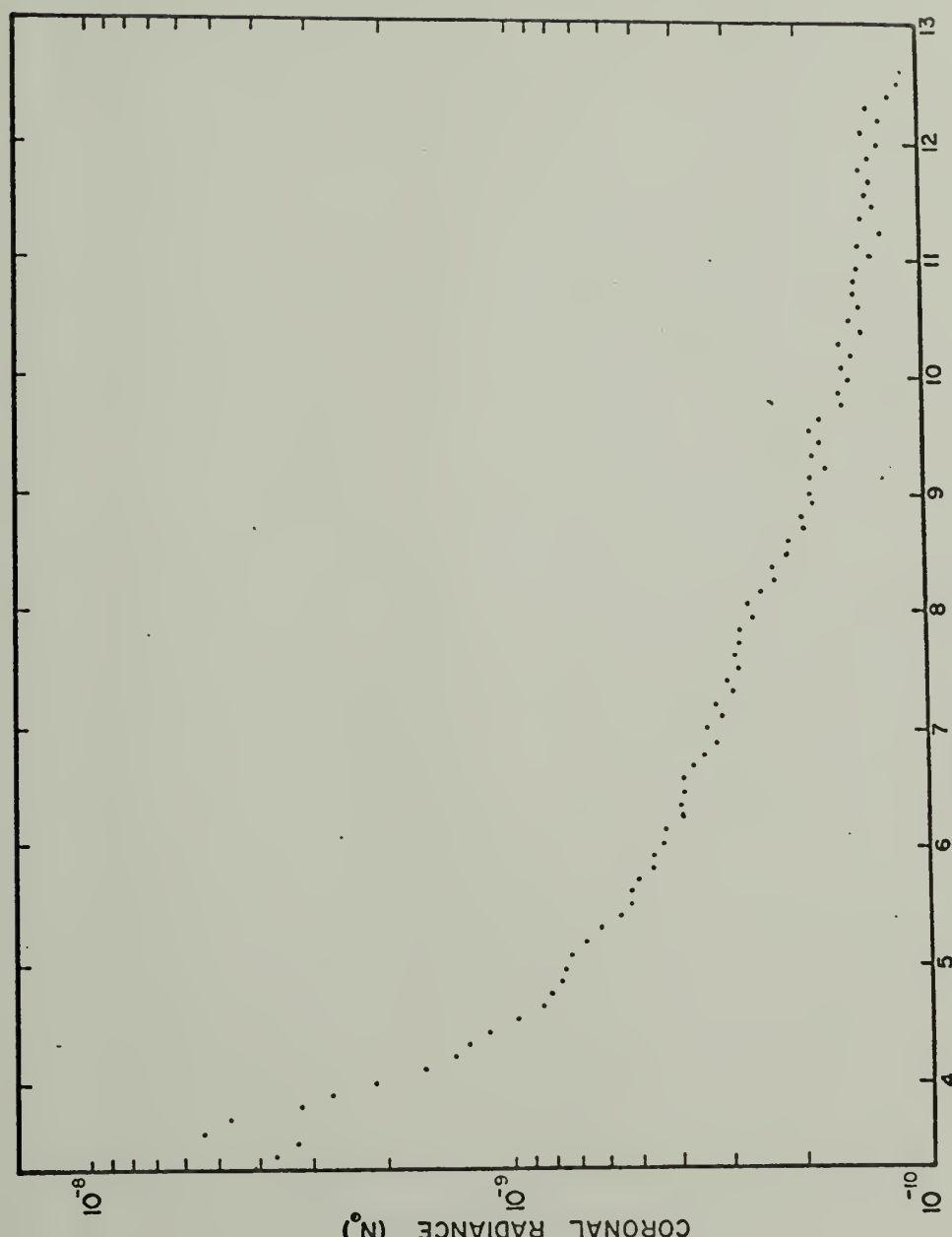

Fig. 16.--Coronal radiance as a function of elongation, $R/R_\odot$, observed during the balloon-flight of October 29, 1973. The plotted points are averaged values for detector #4.

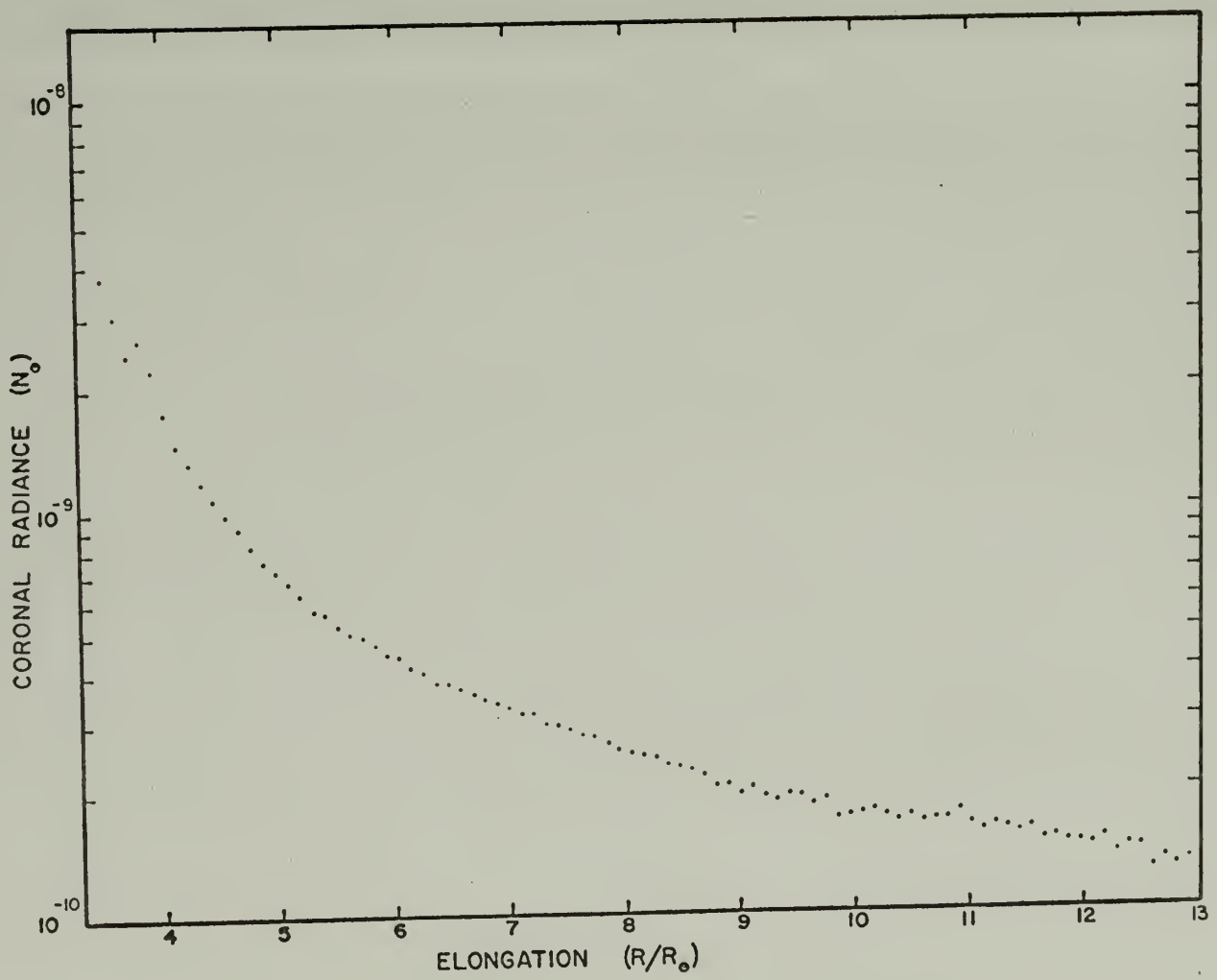

Fig. 17.--Coronal radiance as a function of elongation, $R/R_\odot$, observed during the balloon-flight of October 29, 1973. The plotted points are averaged values for detector #6.

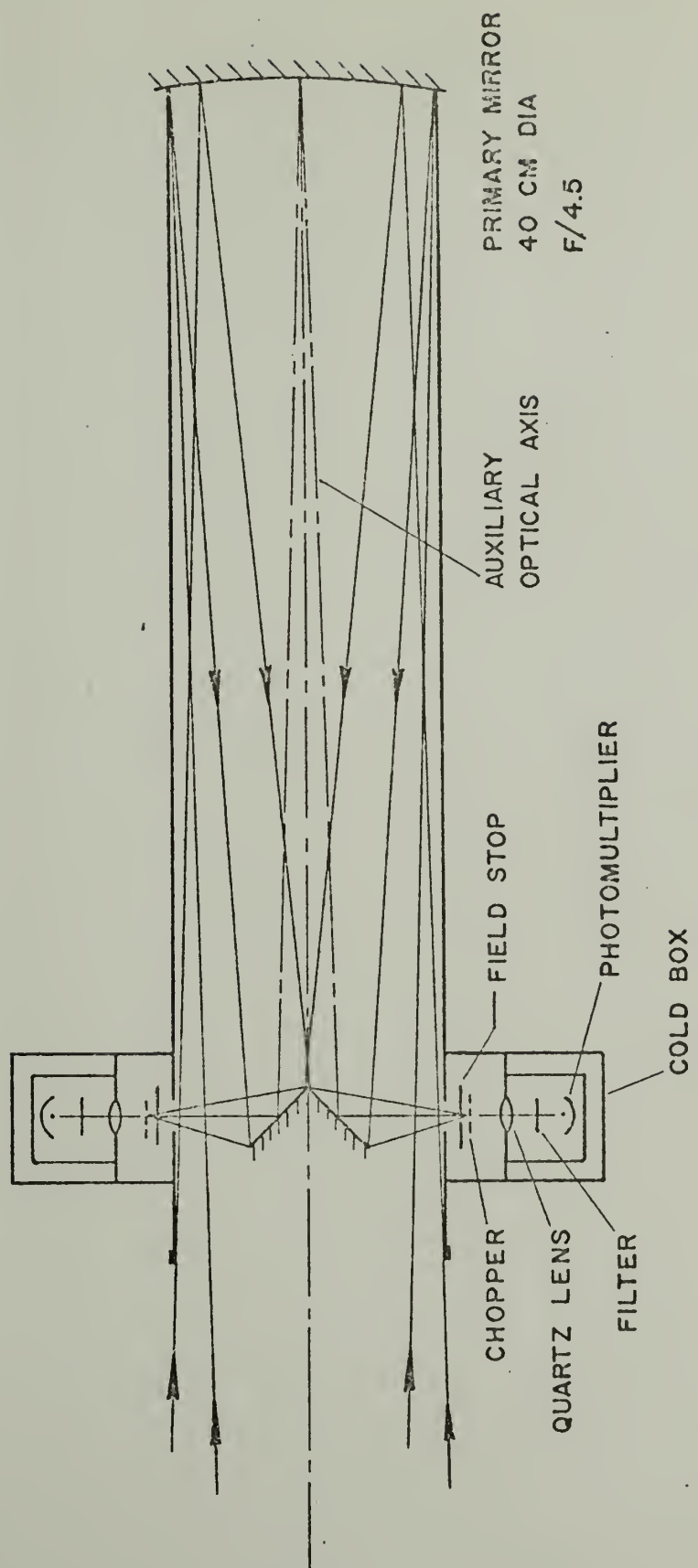

Fig. 18.--Eclipse telescope, 40-cm aperture, $f/4.5$ reflector, showing the twin off-axis photomultiplier detector systems.

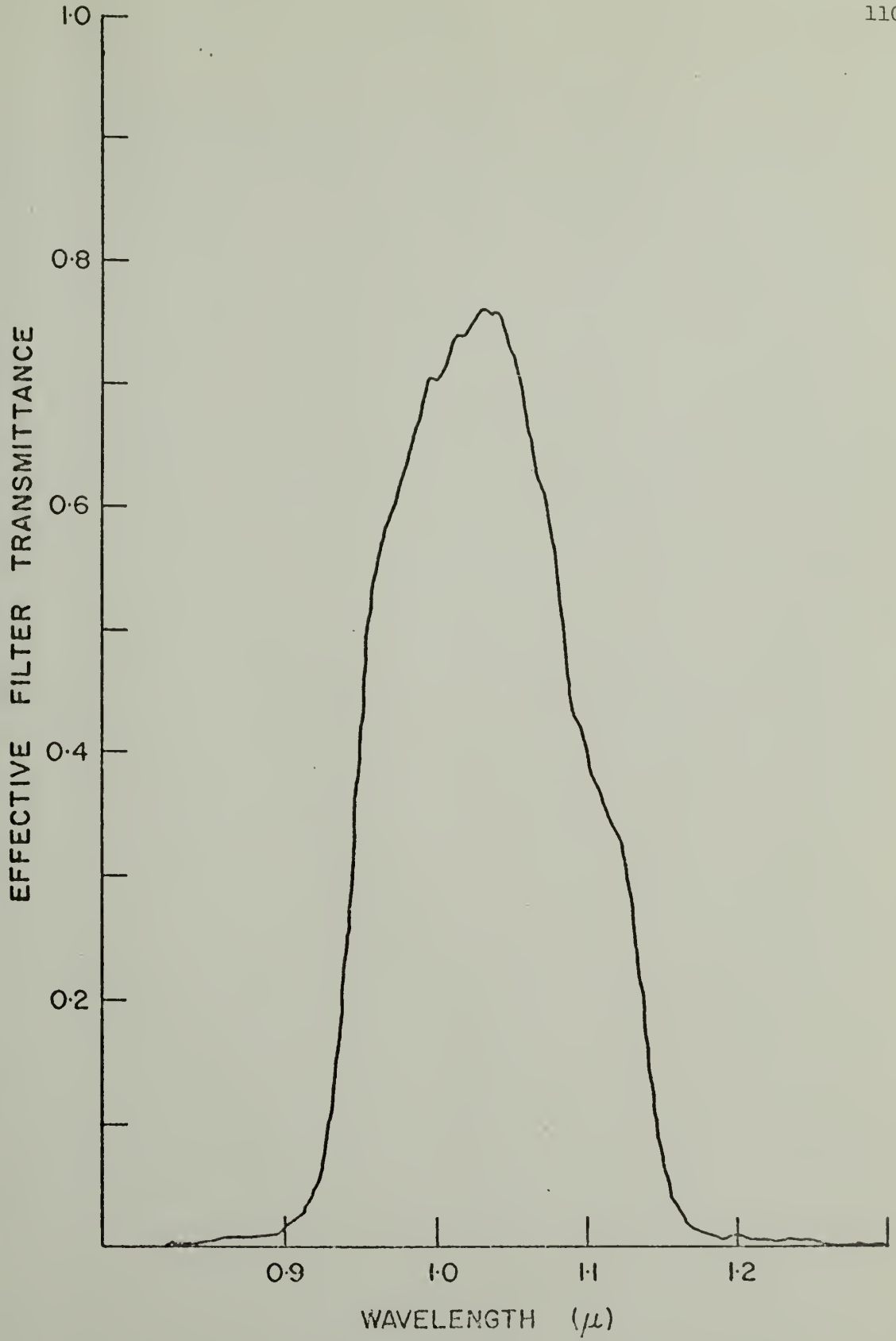

Fig. 19.--Spectral response of the eclipse telescope photomultiplier detection system, D_e.

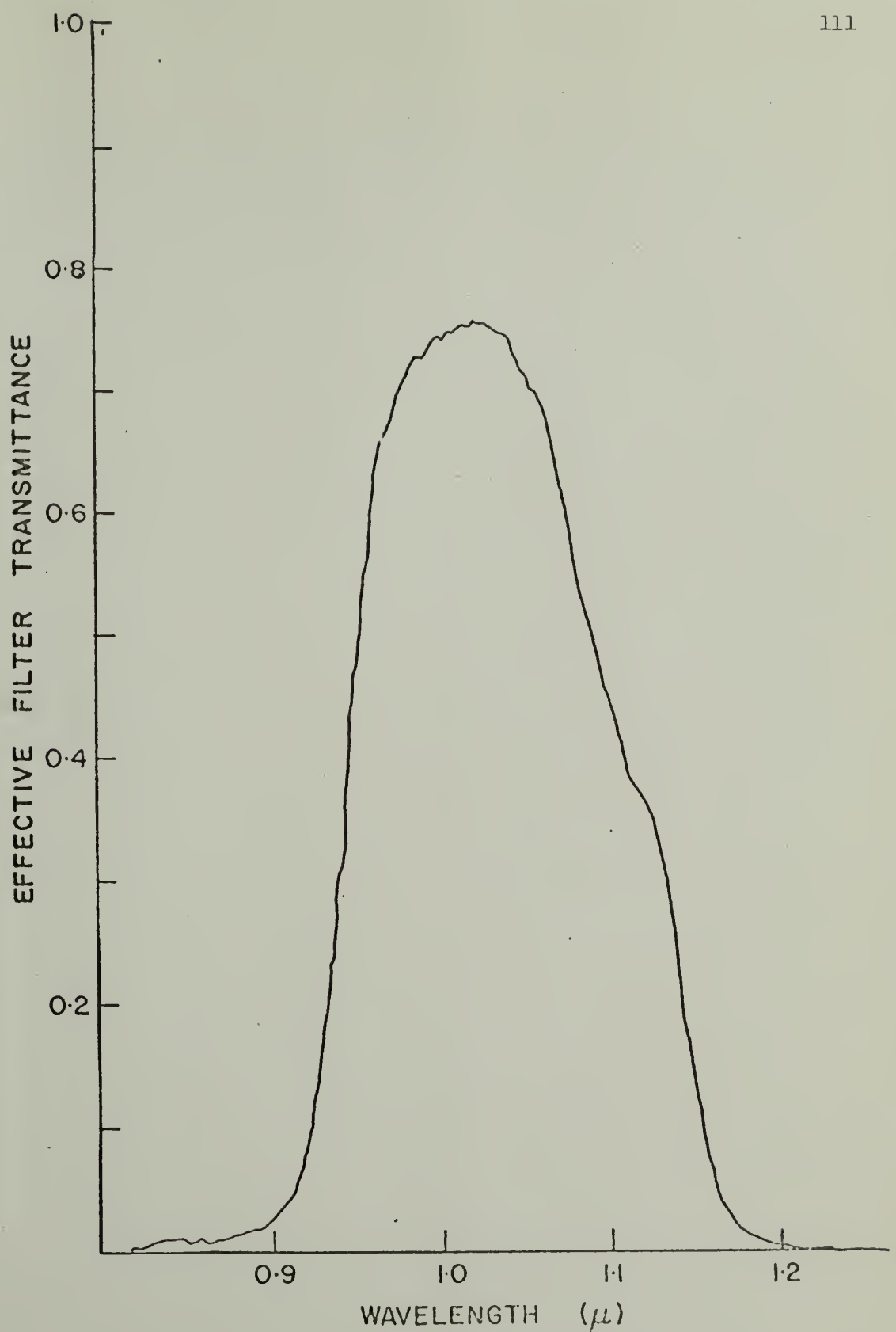

Fig. 20.--Spectral response of the eclipse telescope photomultiplier detection system, D_w.

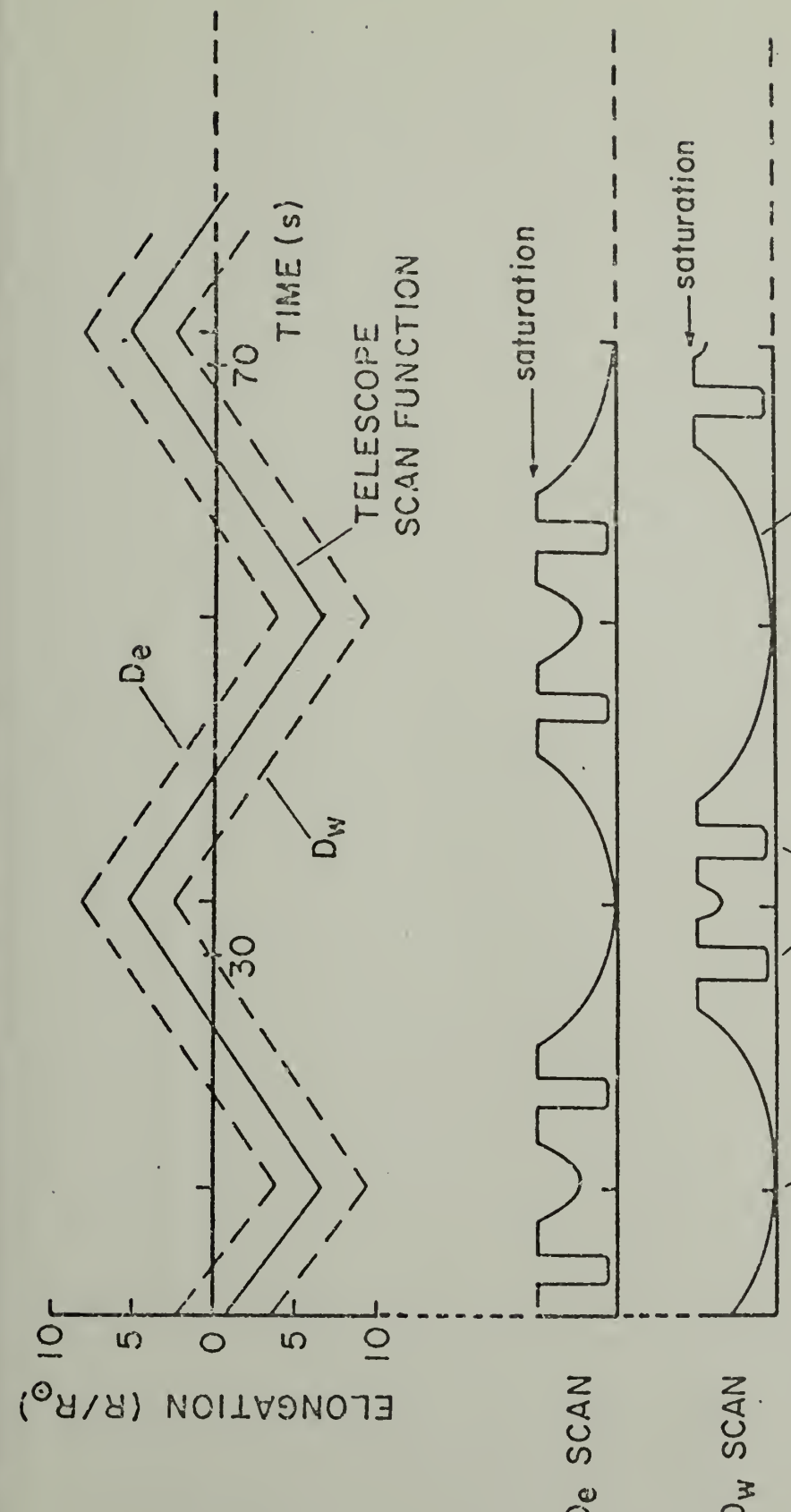

Fig. 21.--Telescope scan program during the period of totality.

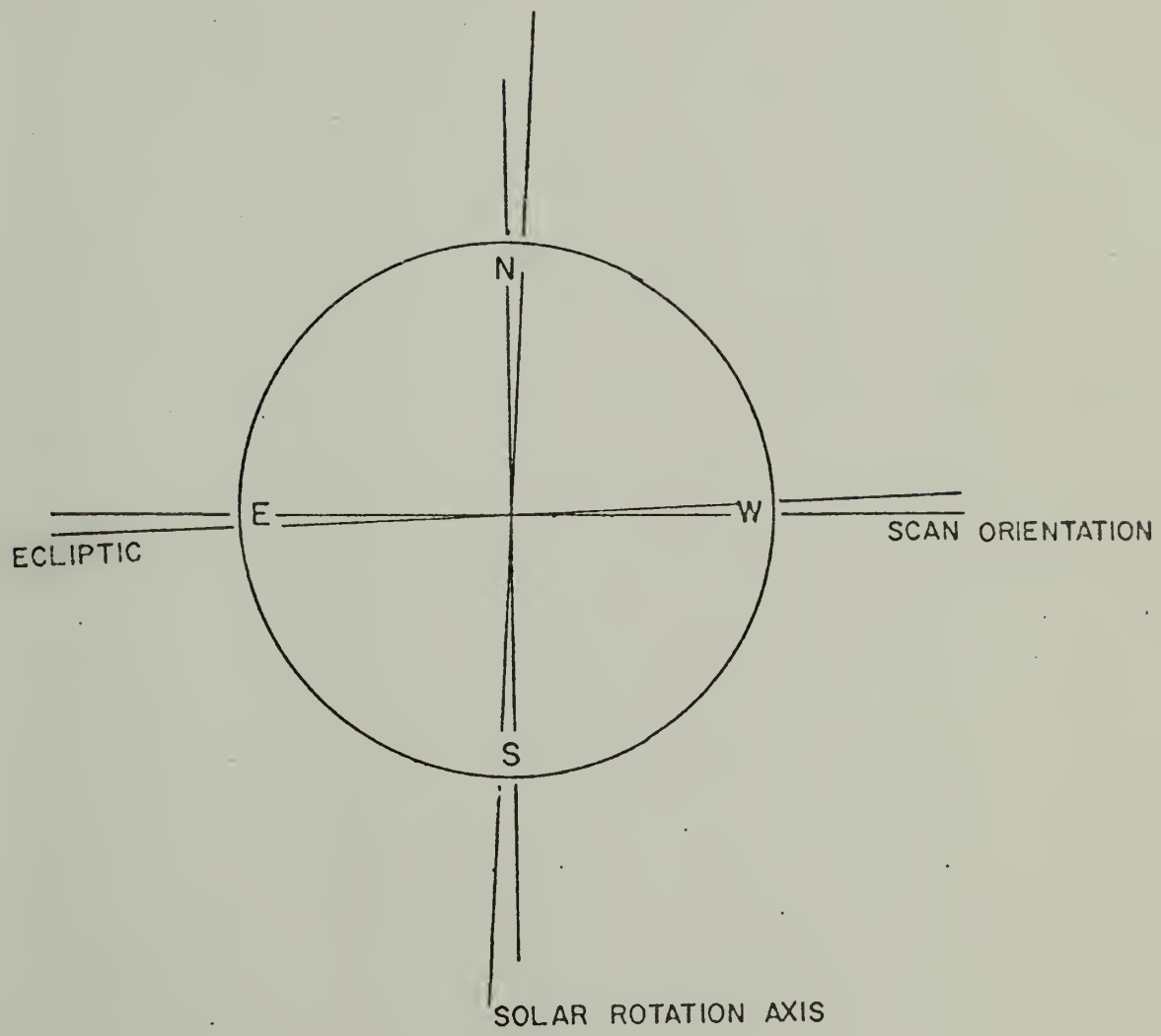

Fig. 22.--Relative orientation of the diametral scans across the solar disk with respect to the ecliptic.

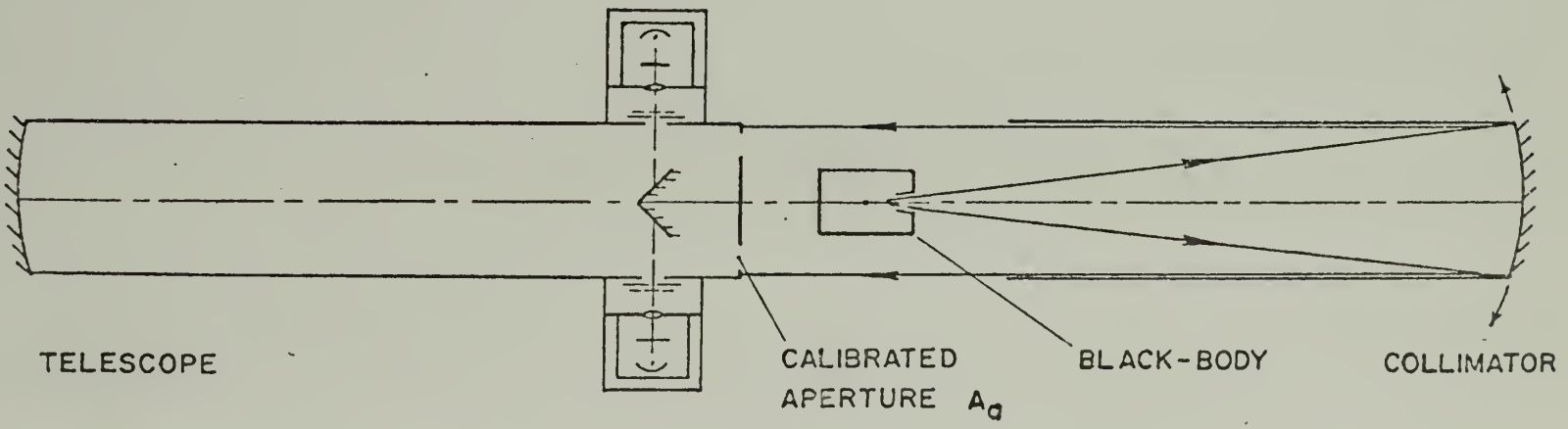

Fig. 23.--Optical system configuration to determine the responsivity of each detector.

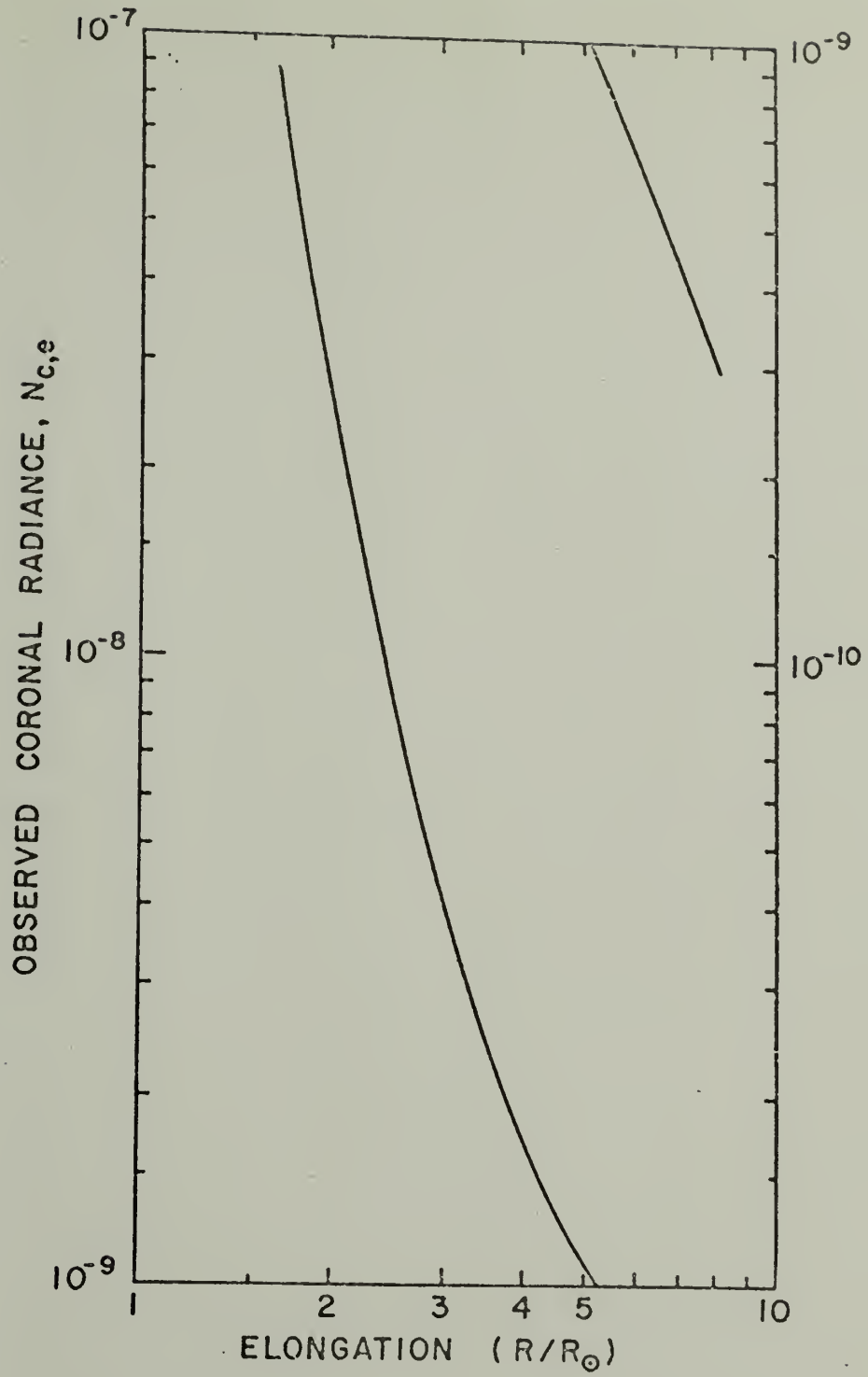

Fig. 24.--Observed coronal radiance, $N_{c,e}$, (units of $N_\odot$) as a function of elongation ($R/R_\odot$), measured east of the solar disk.

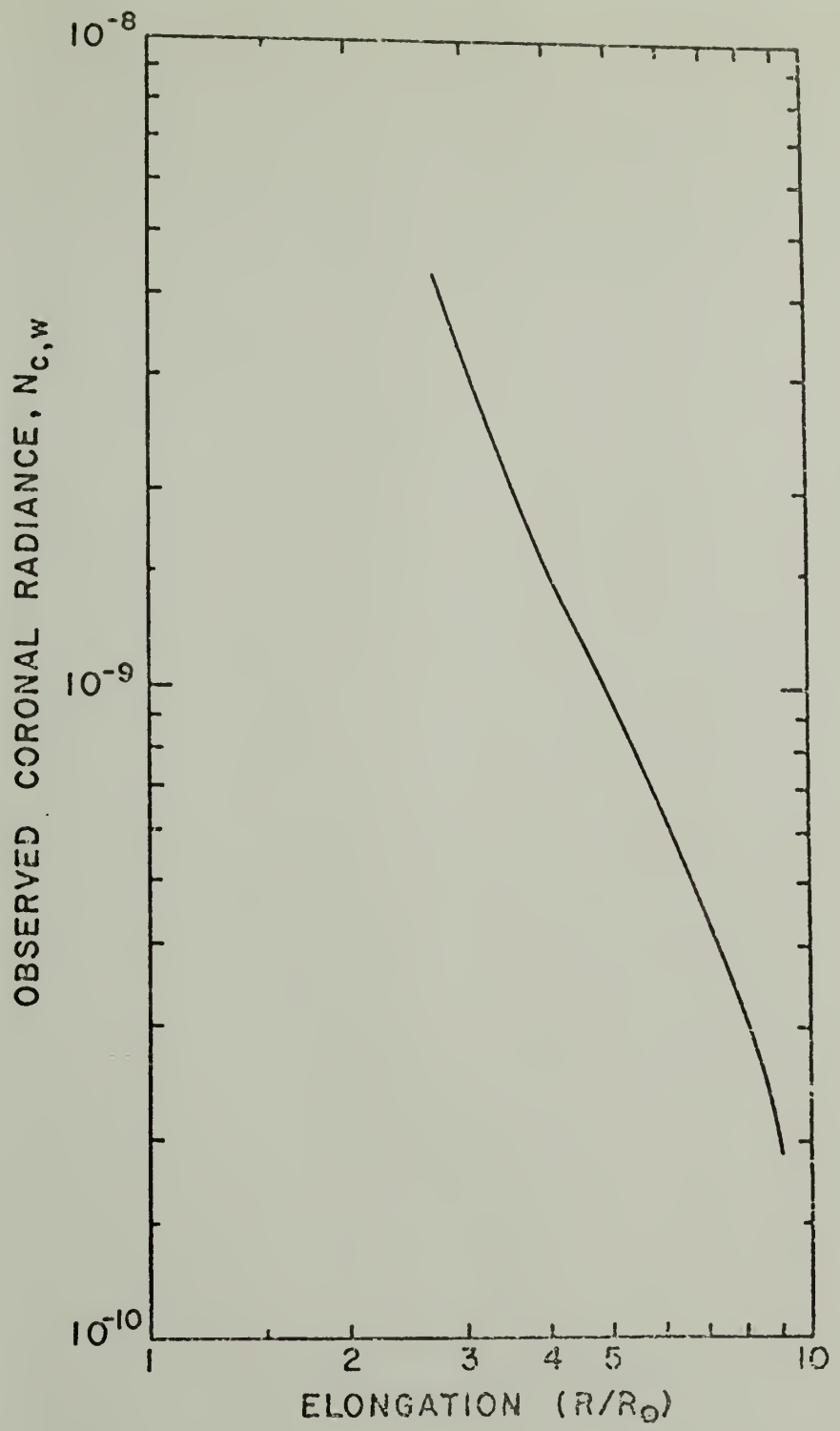

Fig. 25.--Observed coronal radiance, $N_{c,w}$, (units of $N_\odot$) as a function of elongation ($R/R_\odot$), measured west of the solar disk.

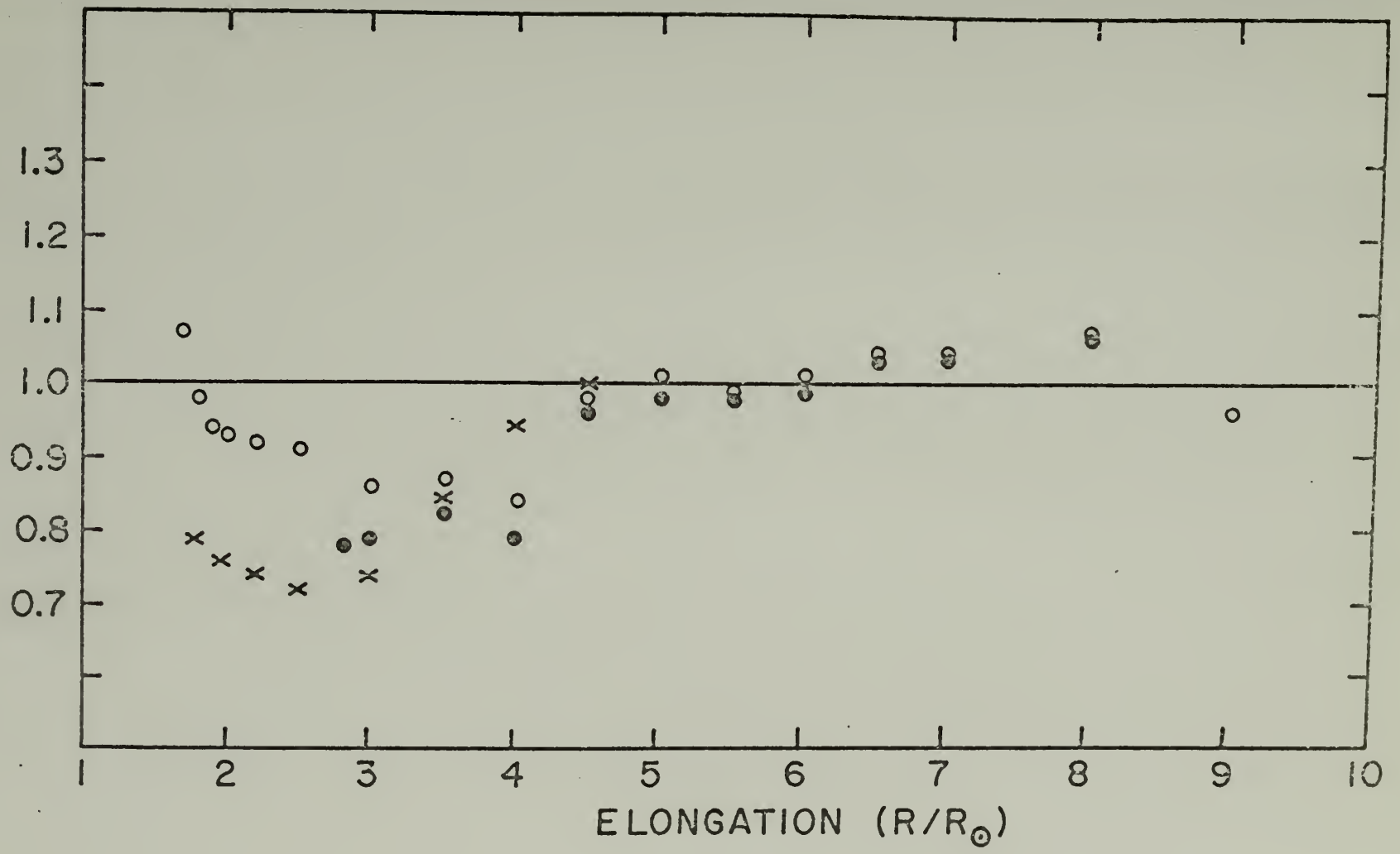

Fig. 26.--Plots of the ratios $N_{c,e}/N_{K+F}(o)$, $N_c/N_{K+F}(o)$, and $N'_{cal}(x)$, as a function of elongation, $R/R_\odot$.

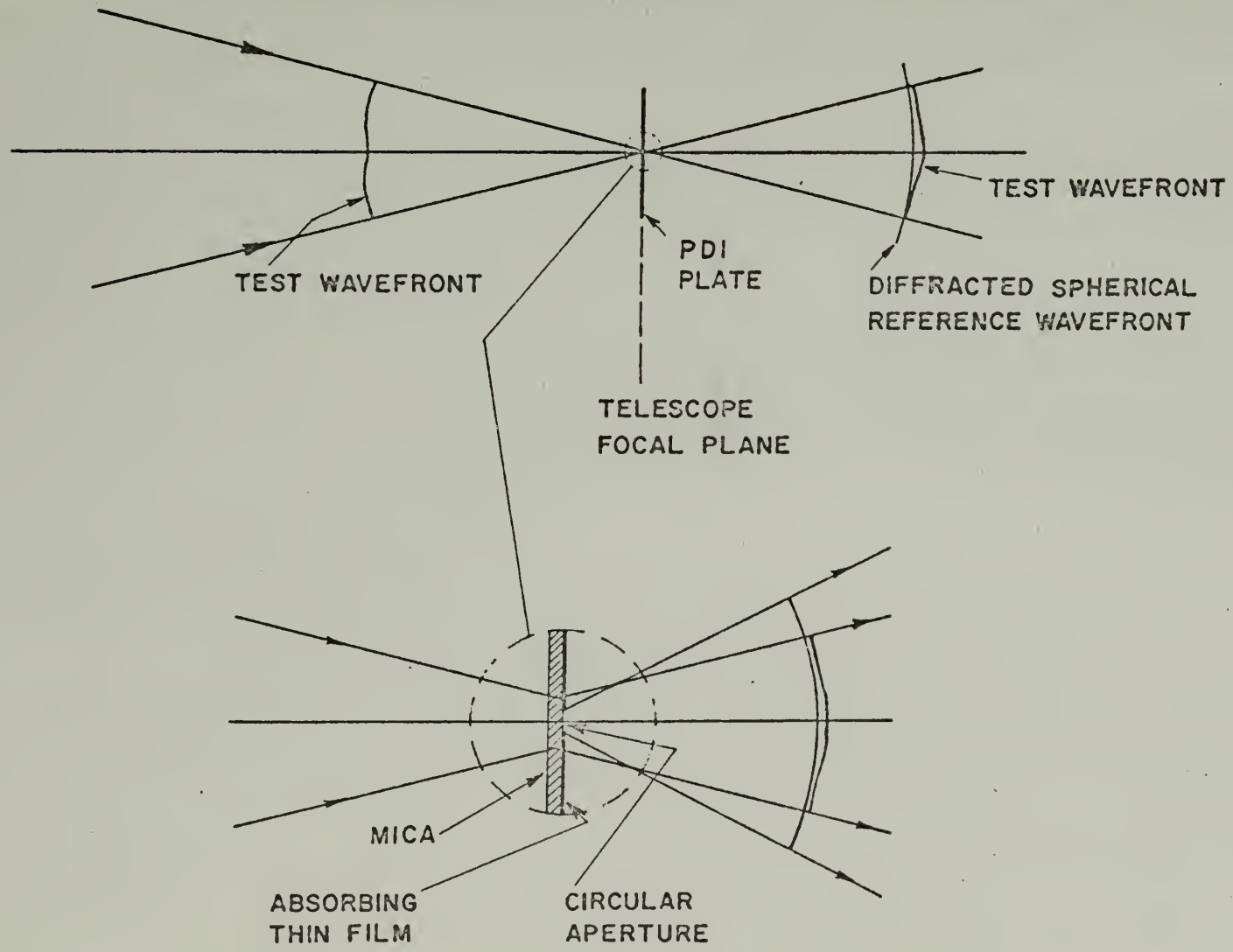

Fig. 27.--Principle of operation of the point-diffraction interferometer, applied as a telescope test.

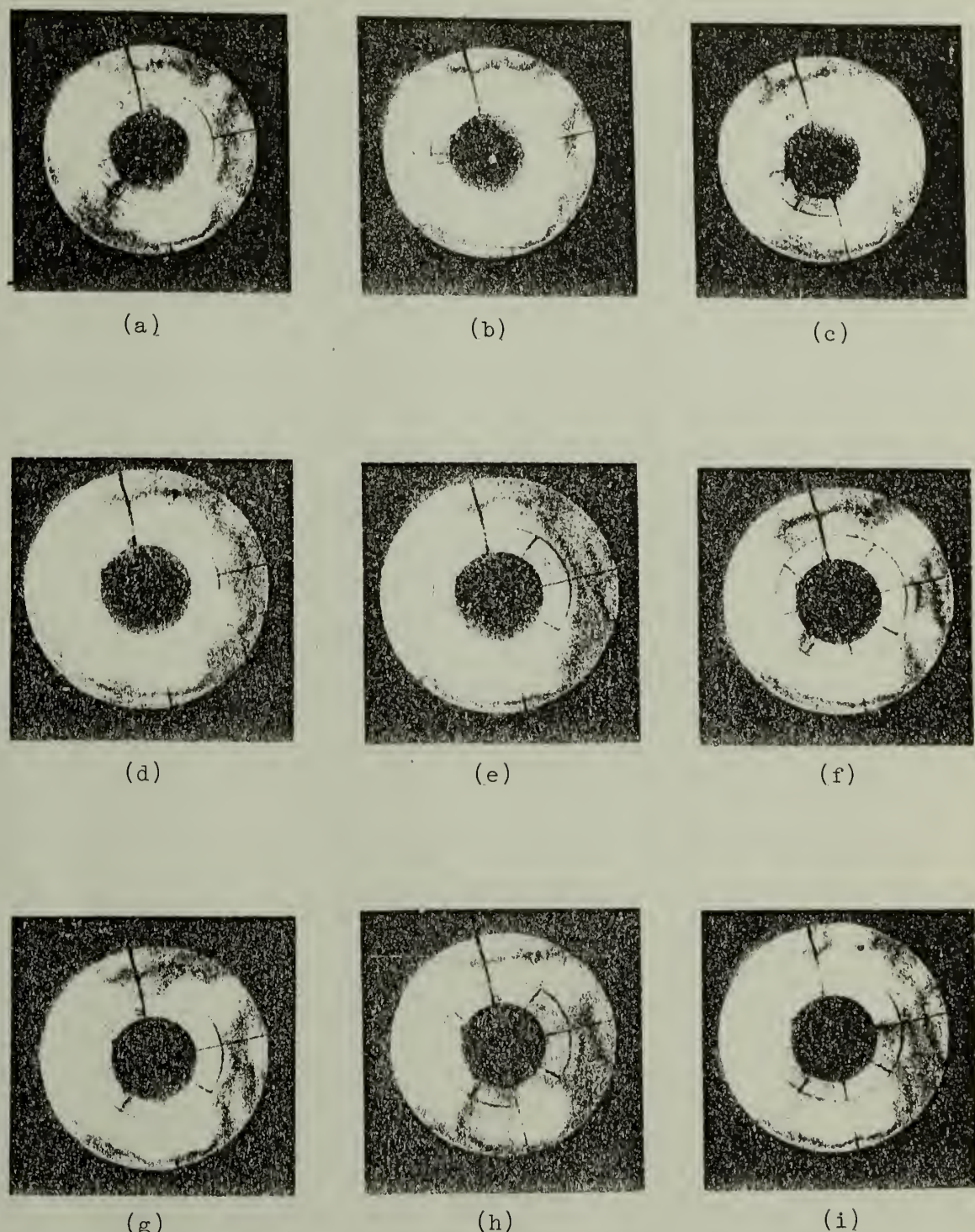

Fig. 28.--PDI interferograms of a 152-cm Cassegrain telescope (Mt. Palomar, Hale Observatories) using a stellar source. These interferograms were recorded over a period of approximately 10 minutes during atmospheric seeing conditions of exceptional stability. Common features characterize wavefront errors associated with the telescope optical system.

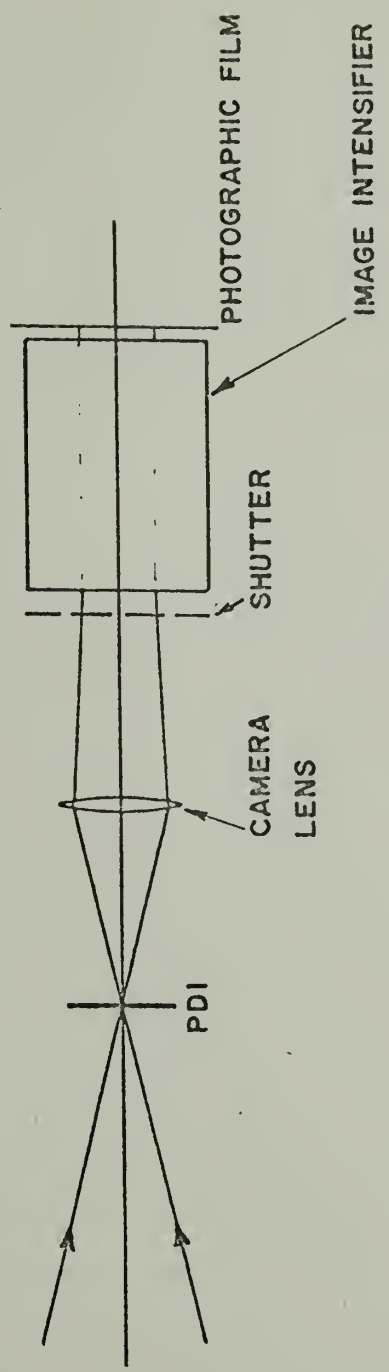

Fig. 29.--Image intensifier and camera, attached beyond Cassegrain focus.

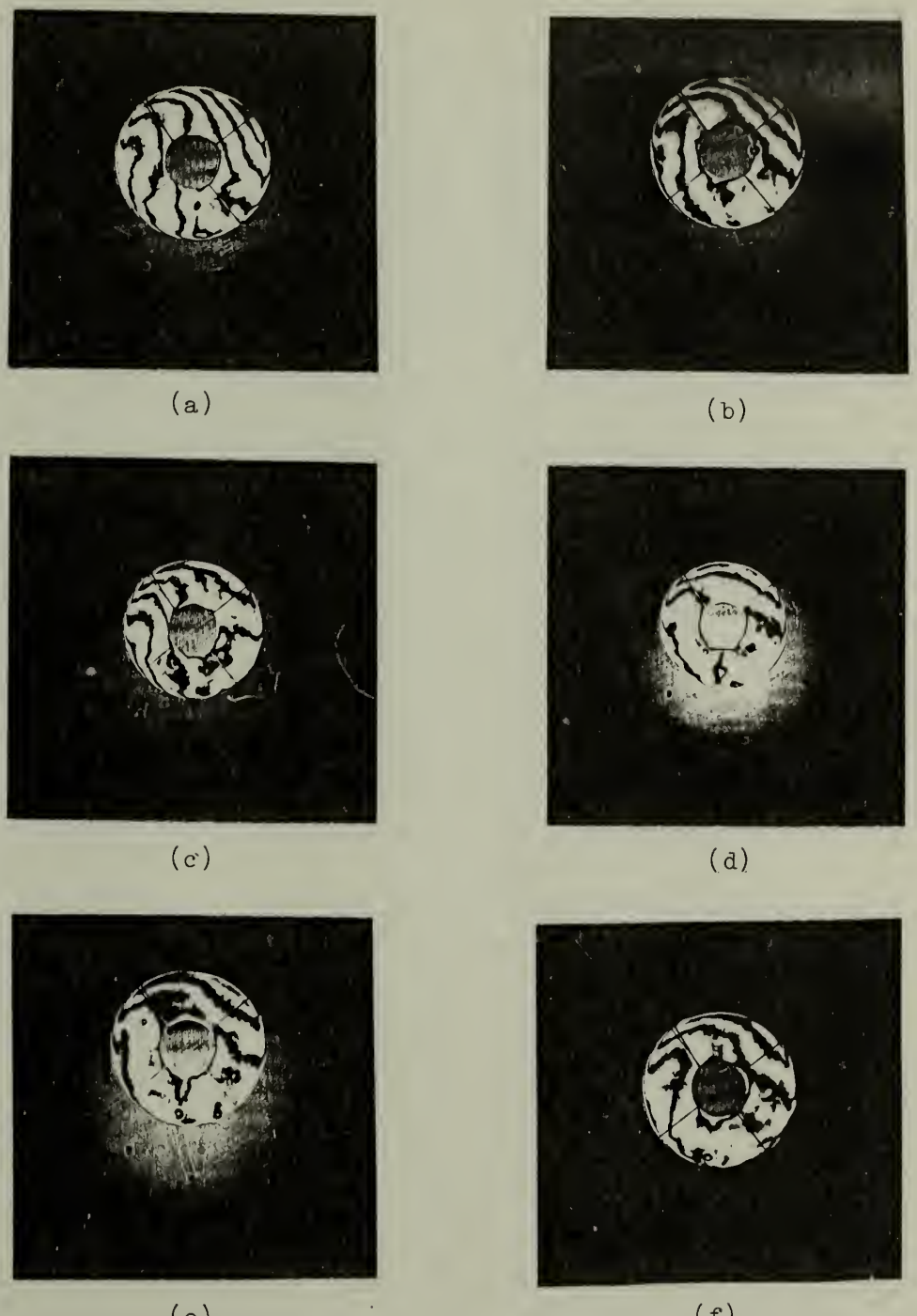

Fig. 30.--PDI interferograms of a 61-cm Cassegrain telescope (Williston Observatory, Mt. Holyoke College) using a 2 mW He-Ne laser source at 2.3 km. Each interferogram displays random perturbations due to thermal fluctuations in the air path. The dominant asymmetrical character of the interference patterns reveals optical errors of the telescope, subsequently traced to mirror misalignment.

(a) (b)

Fig. 31.--PDI interferograms of a 20-cm Schmidt-Cassegrain telescope, recorded indoors with a laser source at 30 m.

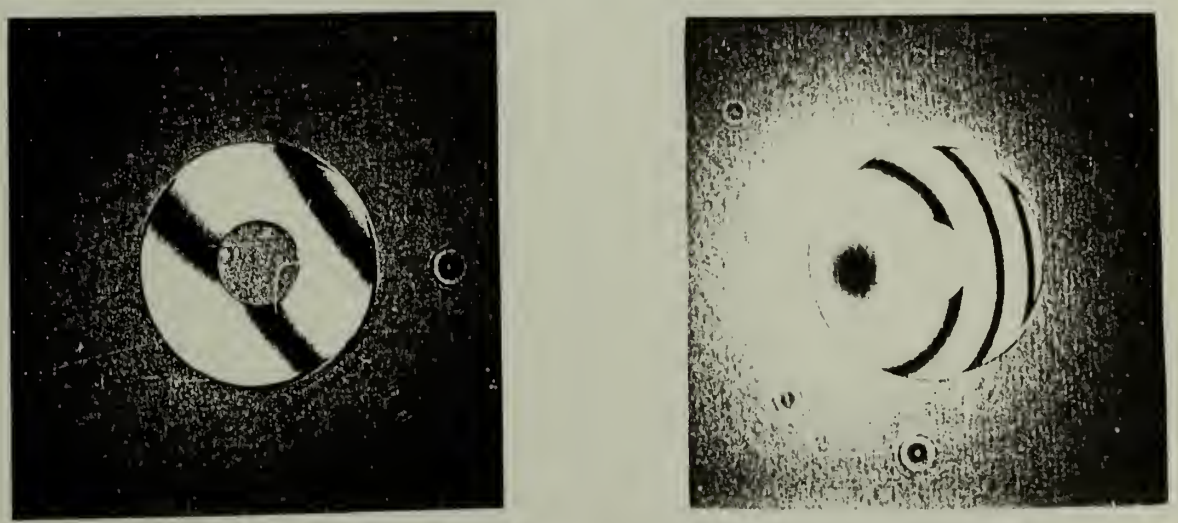

(a) (b)

Fig. 32.--PDI interferograms of a 9-cm Maksutov-Cassegrain telescope, recorded indoors with a laser source at 30 m. The wavefront error is $< 0.1\ \lambda$.

REFERENCES

1. Kelvin, M.N. 20, 317 (1860).
2. T.A. Edison, Am. J. Sci. 117, 52 (1879).
3. Magrini, Mem. R.A.S. 41, 246 (1879).
4. J.M. Wilson, Mem. R.A.S. 41, 251 (1879).
5. J.W. Langley, Wash. Obs. 23, Part 2, App. III, 211 (1880).
6. W. Harkness, Wash. Obs. 23, Part 2, App. III, 386 (1880).
7. W. Abney and T.E. Thorpe, Phil. Trans. (A) 180, 363 (1889).
8. E.C. Pickering, Harvard Annals 18, No. 5, 85 (1890).
9. H.H. Turner, Phil. Trans. (A) 180, 385 (1889).
10. G.G. Stokes, Mem. R.A.S. 41, 331 (1879).
11. G.K. Winter, Mem. R.A.S. 41, 324 (1879).
12. A.W. Wright, Wash. Obs. 23, Part 2, App. III, 261 (1880).
13. A. Schuster, M.N. 40, 35 (1879).
14. W. Huggins, Proc. Roy. Soc. 39, 108 (1885).
15. W. Grotrian, Zs. f. Ap. 8, 124 (1934).
16. S. Koutchmy, Astr. and Ap. 16, 103 (1972).
17. P.J. Kellogg and E.P. Ney, Nature 183, 1297 (1959).
18. C.W. Allen, M.N.R.A.S. 106, 137 (1946).
19. H.C. van de Hulst, Ap. J. 105, 471 (1947).
20. S. Koutchmy and F. Magnant, Ap. J. 186, 671 (1973).
21. R.M. MacQueen, J.A. Eddy, J.T. Gosling, E. Hildner, R.H. Munro, G.A. Newkirk, A.I. Poland and C.L. Ross, Ap. J. 187, L85 (1974).
22. M.J. Koomen and R. Tousey, in *The Zodiacal Light and the Interplanetary Medium*, J.L. Weinberg, Ed. (NASA SP-150, 1967), p. 79.

23. A.W. Peterson, Ap. J. 138, 1218 (1963).

24. C.G. Abbot, Ap. J. 12, 69 (1900).

25. S.P. Langley, Ap. J. 12, 370 (1900).

26. K.V. Sheridan, Proc. Astronom. Soc. of Australia 1, 376 (1970).

27. W.H. Anderson, Zs. f. Phys. 28, 299 (1924).

28. M.J.S. Belton, Science 151, 35 (1966).

29. H.N. Russell, Ap. J. 69, 49 (1929).

30. J. Over, Proc. Koninkl. Ned. Akad. Wetenschap. 61B, 74 (1958).

31. C.B. Kaiser, Ap. J. 159, 77 (1970).

32. P.L. Lamy, Astr. and Ap. 33, 191 (1974).

33. A.I. Lasarev, Sov. Astr.--AJ 8, 285 (1964).

34. V.I. Moroz and P.N. Boiko, Sov. Astr.--AJ 9, 89 (1965).

35. A.W. Peterson, Ap. J. 148, L37 (1967).

36. A.W. Peterson, Ap. J. 155, 1009 (1969).

37. D.E. Blackwell, D.W. Dewhirst and M.F. Ingham, in *Advances in Astronomy and Astrophysics*, Vol. 5, Z. Kopal, Ed. (Academic Press, New York, 1967), p. 1.

38. R.M. MacQueen, Ap. J. 154, 1059 (1968).

39. A.W. Peterson, Bull. Am. Astron. Soc. 3, 500 (1971).

40. W.G. Mankin, R.M. MacQueen and R.H. Lee, Astr. and Ap. 31, 17 (1974).

41. R. Calbert and D.B. Beard, Ap. J. 176, 497 (1972).

42. G.E. Hale, Ap. J. 1, 318 (1895).

43. G.E. Hale, Ap. J. 12, 372 (1900).

44. H. Deslandres, Ap. J. 12, 287 (1900).

45. B. Lyot, C.R. Acad. Sci. Paris 191, 834 (1930).

46. B. Lyot, C.R. Acad. Sci. Paris 193, 1169 (1931).

47. B. Lyot, M.N. 99, 580 (1939).

48. G.A. Newkirk and J.D. Bohlin, Ann. Astrophys. 28, 234 (1965).

49. G. Wlerick and J. Axtell, Ap. J. 126, 253 (1957).

50. G.A. Newkirk and D. Bohlin, Appl. Opt. 2, 131 (1963).

51. G.A. Newkirk and J.A. Eddy, Nature 194, 638 (1962).

52. G.A. Newkirk and J.A. Eddy, J. Atm. Sci. 21, 35 (1964).

53. R.M. MacQueen, Appl. Opt. 7, 1149 (1968).

54. J.D. Bohlin, M.J. Koomen and R. Tousey, Solar Phys. 21, 408 (1971).

55. J.W. Evans, J. Opt. Soc. Am. 38, 1083 (1948).

56. J.D. Purcell and M.J. Koomen, J. Opt. Soc. Am. 52, 596A (1962).

57. J.H. Rush and G.K. Schnable, Appl. Opt. 3, 1347 (1964).

58. H. Zirin and G. Newkirk, Appl. Opt. 2, 977 (1963).

59. G.R. Hostetter, D.L. Patz, H.A. Hill and C.A. Zanoni, Appl. Opt. 7, 1383 (1968).

60. J. Demarcq and J. Rosch, in *Advanced Optical Techniques*, A.C.S. Van Heel, Ed. (North-Holland Publishing Co., Amsterdam, 1967), p. 396.

61. T.C. Li, Appl. Opt. 12, 2828 (1973).

62. P. Beckmann and A. Spizzichino, *The Scattering of Electromagnetic Waves From Rough Surfaces* (MacMillan Company, New York, 1963), p. 30.

63. H.E. Bennett, J. Opt. Soc. Am. 60, 1577A (1970).

64. F. Zernike, Z. Tech. Phys. 16, 454 (1935).

65. M. Born and E. Wolf, *Principles of Optics* (Pergamon Press, New York, 1970).

66. J.W. Goodman, *Introduction to Fourier Optics* (McGraw-Hill, New York, 1968).

67. L.C. Martin and J.V. Ramsay, in *Le Contraste de Phase et le Contraste par Interférences*, M. Francon, Ed. (Revue d'Optique, Paris, 1952), p. 164.

68. R. Fleischmann and H. Schopper, Z. Physik 130, 304 (1951).

69. J.L. Stanford, E.J. Ashley and H.E. Bennett, J. Opt. Soc. Am. 60, 1543A (1970).

70. G. Newkirk and J.A. Eddy, Sky and Telescope 24, 3 (1962).

71. J. Strong, Appl. Opt. 6, 179 (1967).

72. M. Bottema, Appl. Opt. 6, 213 (1967).

73. R. Zander, J. Geophys. Res. 71, 3775 (1966).

74. W.G. Mankin, Dissertation, Johns Hopkins University, Baltimore (1969).

75. J. Strong, Interim Report, NASA Grant NGL 22-010-025, Astronomy Research Facility, University of Massachusetts (1972).

76. G.E. Shaw, Appl. Opt. 14, 388 (1975).

77. C.W. Allen, *Astrophysical Quantities* (University of London, Athlone Press, London, 1973), p. 172.

78. G.E. Shaw, J.A. Reagan and B.M. Herman, J. Appl. Meteorol. 12, 374 (1973).

79. K.Ya. Kondratiev, G.A. Nicolsky, I.Ya. Badinov and S.D. Andreev, Appl. Opt. 6, 197 (1967).

80. J.H. Taylor and H.W. Yates, J. Opt. Soc. Am. 47, 223 (1957).

81. D.M. Gates, J. Meteor. 13, 369 (1956).

82. D.M. Gates, J. Opt. Soc. Am. 50, 1299 (1960).

83. D.M. Gates and W.J. Harrop, Appl. Opt. 2, 887 (1963).

84. N. Medrud, Astro-Geophysical Memorandum No. 180, High Altitude Observatory, Boulder, Colorado (1971).

85. E. Raschke, T.H. Vonder-Haar, W.R. Bandeen and M. Pasternak, J. Atmos. Sci. 30, 341 (1973).

86. A. Angstrom, Tellus 14, 435 (1962).

87. S. Fritz, J. Meteor. 6, 277 (1949).

88. K.L. Coulson, Planet. Space Sci. 1, 277 (1959).

89. A. Lane and W.M. Irvine, Astron. J. 78, 267 (1973).

90. B.S. Dandekar, Appl. Opt. 7, 705 (1968).

91. W.E. Sharp, S.M. Silverman and J.W. Lloyd, Appl. Opt. 10, 1207 (1971).

92. J.W. Lloyd and S.M. Silverman, Appl. Opt. 10, 1215 (1971).

93. W.N. Hall, Appl. Opt. 10, 1225 (1971).

94. G. Newkirk, R.G. Dupree and E.J. Schmahl, Solar Phys. 15, 15 (1970).

95. G. Newkirk, J. Opt. Soc. Am. 46, 1028 (1956).

96. O. Koutchmy and S. Koutchmy, Astron. Astrophys. Suppl. 13, 295 (1974).

97. H.C. van de Hulst, in *The Sun*, G.P. Kuiper, Ed. (University of Chicago Press, Chicago, 1962), p. 257.

98. K. Saito, Ann. Tokyo Astr. Obs. Sec. Ser. 12, 53 (1970).

99. M.F. Ingham, M.N.R.A.S. 122, 157 (1961).

100. D.E. Blackwell, D.W. Dewhirst and M.F. Ingham, in *Advances in Astronomy and Astrophysics*, Vol. 5, Z. Kopal, Ed. (Academic Press, New York, 1967), p. 58.

101. J. Texereau, Appl. Opt. 2, 23 (1963).

102. R.G. Wilson, Appl. Opt. 14, 2286 (1975).

103. J. Strong, *Concepts of Classical Optics* (W.H. Freeman and Company, San Francisco, 1958), p. 273.

104. J. Hartmann, Z. Instrum. 24, 1 (1904).

105. I. Ghozeil and J.E. Simmons, Appl. Opt. 13, 1773 (1974).

106. V. Ronchi, Appl. Opt. 3, 437 (1964).

107. R.N. Smartt and J. Strong, J. Opt. Soc. Am. 62, 737 (1972).

108. R.N. Smartt, J. Opt. Soc. Am. 64, 558 (1974).

109. L. Mandel, J. Opt. Soc. Am. 51, 1342 (1961).

110. J. Perina, *Coherence of Light* (Van Nostrand Reinhold Company, London, 1971).

111. W.H. Steel, *Interferometry* (University Press, Cambridge, 1967).

112. M.V. Murty, J. Opt. Soc. Am. 53, 568 (1963).

113. R.N. Smartt, Appl. Opt. 13, 1093 (1974).

114. R.M. Scott, Appl. Opt. 8, 531 (1969).

115. B.P. Hildebrand and K.A. Haines, Appl. Opt. 5, 172 (1966).

116. J.B. Saunders, Japan J. Appl. Phys. 4, Supplement 4-1, 99 (1965).